DECADAL PREDICTABILITY IN CLIMATE MODELS WITH AND WITHOUT INTERACTIVE OCEAN DYNAMICS

by

Abhishekh K. Srivastava

A Dissertation
Submitted to the
Graduate Faculty
of
George Mason University
In Partial fulfillment of
The Requirements for the Degree
of
Doctor of Philosophy
Climate Dynamics

Committee:

______________________ Dr. Timothy DelSole, Dissertation Director

______________________ Dr. Jagadish Shukla, Committee Member

______________________ Dr. Edwin K. Schneider, Committee Member

______________________ Dr. Edwin K. Schneider, Department Chair

______________________ Dr. Donna M. Fox, Associate Dean,
Office of Student Affairs & Special Programs,
College of Science

______________________ Dr. Peggy Agouris, Dean, College of Science

Date: ______________________ Spring Semester 2017
George Mason University
Fairfax, VA

Decadal predictability in climate models with and without interactive ocean dynamics

A dissertation submitted in partial fulfillment of the requirements for the degree of Doctor of Philosophy at George Mason University

By

Abhishekh K. Srivastava
Master of Science
University of Allahabad, 2000
Bachelor of Science
University of Allahabad, 1997

Director: Dr. Timothy DelSole, Professor
Department of Atmospheric, Oceanic and Earth Sciences

Spring Semester 2017
George Mason University
Fairfax, VA

Dedication

I dedicate this dissertation to Almighty God, my parents Late Satish Chandra Srivastava and Mrs. Beena Srivastava, and my wife Mrs. Sandhya Singh.

Acknowledgments

I would like to thank the following people who made this thesis possible.

First and foremost, I am very thankful to my supervisor, Dr. Timothy DelSole, who provided me unconditional guidance and inspiration throughout my PhD. I have no doubts in saying that whatever I have learnt as a PhD student is largely attributed to his exemplary teaching and thorough training. There had been several occasions when I would have given up, but I sustained because of his support, advice and guidance. Without him, this thesis would never have been completed.

I sincerely thank my PhD committee member Dr. Jagadish Shukla, who motivated me to join Climate Dynamics program in George Mason University. He has been a constant source of inspiration to me. I must thank my PhD committee member Dr. Edwin Schneider for his motivation, suggestions and unconditional support during my PhD.

I also thank Dr. Barry Klinger for his valuable advice and help from time to time.

I must thank Dr. Avinash Chandra Pandey, Professor, University of Allahabad, who is friend, philosopher and guide to me. I must say without his support, motivation and suggestions, I would not have been able to pursue PhD in the USA. He has been a constant source of motivation, support and strength to me.

I thank my brother Avinash Srivastava and sister-in-law Akriti Srivastava to support and motivate me during my PhD.

Lastly, I must acknowledge my grandparents Late Rajendra Prasad Srivastava and Late Kesri Devi for inculcating valuable cultural and human values in me.

Table of Contents

List of Tables

List of Figures

Abstract

DECADAL PREDICTABILITY IN CLIMATE MODELS WITH AND WITHOUT INTERACTIVE OCEAN DYNAMICS

Abhishekh K. Srivastava, PhD

George Mason University, 2017

Dissertation Director: Dr. Timothy DelSole

Climate variations on decadal time scales, such as droughts and changes in extreme weather events, have a great impact on society and therefore reliable predictions of these variations would be valuable. Unfortunately, the mechanisms of this variability have remained unclear partly due to observational limitations and partly due to limitations of current climate models. The purpose of this dissertation research is to improve understanding of decadal variability and predictability through analysis of simulations and simple stochastic models. As a first step, the most predictable components of 2m-air temperature are identified through an objective procedure called Average Predictability Time (APT) analysis. This analysis reveals that the most predictable components of internal variability in coupled atmosphere-ocean models are remarkably similar to the most predictable components of climate models without interactive ocean dynamics (i.e., models whose ocean is represented by a 50m-deep slab ocean mixed layer with no interactive currents). This result suggests that interactive ocean circulation is not essential for the existence of multi-year predictability previously identified in coupled models and observations. A new stochastic model is proposed that captures the essential physics of decadal variability in the latter models. This model is based on the linearized primitive equations for the atmosphere, a

slab mixed-layer model for the ocean, a gray radiation scheme for radiative effects, and a diffusive scheme for vertical turbulent eddy fluxes. It is shown that this model generates new low-frequency peaks in the power spectrum that do not exist in either the atmospheric model alone or in the slab ocean mixed layer model alone.

Chapter 1: Introduction

1.1 Importance of decadal predictability

The climate system exhibits multiyear variability in characteristic spatial structures and timescales. For example, the Pacific decadal oscillation (PDO) is the leading mode of decadal climate variability in the North Pacific (Mantua and Hare, 2002) and the Atlantic multidecadal oscillation (AMO) is the mode of climate variability on multidecadal timescales in the North Atlantic(Knight et al., 2006; Schlesinger and Ramankutty, 1994). These modes of climate variability affect the weather and climate of the surrounding continents. For example, more than 50% of the spatial and temporal variance in drought frequency in the US is claimed to be attributable to the PDO and AMO (McCabe et al., 2004). Major hurricane activity in the Atlantic increased by 2.5-fold during the positive phase of the AMO as compared to that during the negative phase of the AMO (Goldenberg et al., 2001). Moreover, the AMO has widespread impact on Sahel rainfall, North American and European summer climate (Knight et al., 2006; Marshall et al., 2001). The PDO greatly impacts fishery and it has been noted that the positive phase of the PDO adversely affects Salmon breeding and their population growth (Mantua et al., 1997). The PDO also impacts Indian summer monsoon such that the positive (negative) phase of the PDO is associated with deficit (excess) summer rainfall over India (Krishnamurthy and Krishnamurthy, 2014; Krishnan and Sugi, 2003). Reliable predictions on multi-year timescales of temperature, precipitation, wind and radiation could prove important for planning for changing demand and supply capacity of energy sector (capacity of power plants, planning for renewable source of energy such as thermal, wind and solar), food security (e.g., selection of crop species), water management, and even land management (Vera et al., 2010). Considering the widespread implications of these components, it would be useful to predict them skillfully.

1.2 Sources of decadal predictability

Sources of decadal predictability are broadly divided into two categories (Kirtman et al., 2013a,b; Meehl et al., 2014). First, due to external forcing and second due to internal climate variability.

1.2.1 Decadal predictability due to external forcing

The first category is predictability caused by external forcing, such as changes in solar insolation, volcanic aerosols, and anthropogenic greenhouse gases (Hegerl et al., 2007; Meehl et al., 2007; Smith et al., 2012). For example, volcanic aerosols injected into stratosphere tend to cool the global mean temperature for years and hence significantly affect the climate on multiyear timescales (Robock, 2000). The response of the climate to the anthropogenic forcing can be seen in the trend of global mean temperature since the year 1900. The trend is comparable to the variability associated with the AMO and PDO, suggesting that anthropogenic forcing is a potential source of decadal predictability (Smith et al., 2012). It is not clear to what extent the external and internal sources are distinct. For example, the extent to which the AMO is externally forced is currently debated (Booth et al., 2012; Zhang et al., 2013). There seems to be more consensus that the PDO is not significantly externally forced (Newman et al., 2016).

In this thesis we do not study decadal predictability due to external forcing and investigate decadal predictability only due to internal climate variability.

1.2.2 Decadal predictability due to internal climate variability

The second category is predictability due to internal variability arising naturally from the coupled atmosphere-ocean-land-ice climate system. There is a significant literature promoting the view point that the Atlantic Multidecadal Oscillation (AMO), Pacific Decadal

Oscillation (PDO) and Atlantic Meridional Overturning Circulation (AMOC) are manifestations of internal variability (e.g., Buckley and Marshall (2016); Newman et al. (2016); Zhang et al. (2013)). Because these quantities vary on decadal/multidecadal time scales, they are are potentially predictable for a significant fraction of their lifetime (Hurrell et al., 2010). Multiple studies highlight four regions where components may be predictable on multi-year time scales: the North Atlantic, the Southern Ocean, the North Pacific, and the tropical Pacific ocean (Boer, 2011; Park and Latif, 2005; Pohlmann et al., 2004).

One of the earliest studies on decadal predictability was done by Griffies and Bryan (1997), who found that subsurface features such as dynamic topography in a global coupled ocean-atmosphere model were more predictable than SST. Their model results suggested that certain features in the subsurface North Atlantic may have predictability on the order of decades. The possible mechanisms they suggested included red noise response of the ocean to white noise forcing of the atmosphere and variability associated with the thermohaline circulation. Both observational and model studies indicate that the AMO varies on multidecadal timescales, possibly linked to the AMOC variability (Delworth et al., 2007; Knight et al., 2005). Coupled atmospheric-ocean general circulation models (AOGCMs) suggest that both the AMO and AMOC are predictable on multidecadal timescales (Collins et al., 2006; Griffies and Bryan, 1997; Hawkins and Sutton, 2009; Pohlmann et al., 2004).

Numerous studies also suggest that the North Pacific is predictable on decadal timescales (Bellucci et al., 2012; Boer, 2004; Boer and Lambert, 2008; Ding et al., 2016). However, the North Pacific seems to be less predictable than the Atlantic region (e.g.,Collins (2002); Ding et al. (2016)). Predictability in this region has been suggested to arise from propagation of oceanic Rossby waves (Schneider and Cornuelle, 2005), a coupled ocean-atmosphere mode (Latif and Barnett, 1994) or tropical-extratropical interactions (Gu and Philander, 1997). Schneider and Cornuelle (2005), using a first-order autoregressive (AR-1) model on North Pacific SST anomalies, argued that on interannual timescales random Aleutian low fluctuations and ENSO teleconnections are equally important for PDO variability with little contribution from ocean dynamics, whereas on decadal timescales stochastic forcing, ENSO teleconnections and ocean gyres contribute equally to the PDO variability. In a review article, Newman et al. (2016) also used an AR-1 model to argue that the PDO is not driven by a single phenomenon but by a combination of different basin-scale ocean processes. Using the AR-1 model of observed SST fluctuation in the Pacific with forcing involving the random Aleutian low forcing and ENSO teleconnections, they deduced that persistence and ENSO teleconnection can explain large fraction of observed PDO variability.

1.3 Mechanisms of decadal predictability due to internal climate variability

One of the simplest hypotheses to explain decadal scale and longer variability in midlatitudes was proposed by Hasselmann (1976). This model divides the climate system into fast and slow components. The atmosphere represents the fast component and the ocean represents the slow component. This division is based upon the fact that atmospheric variability has a timescale typically of the order of days, therefore atmosphere has little memory on the timescale of months or longer. In contrast, the ocean varies much more slowly owing to its thermal and mass inertia and therefore exhibits variability on timescales of months or longer; much longer than that of the atmosphere. Therefore, on oceanic timescales, the atmospheric variability can be assumed to be white noise. The ocean simply integrates this white noise forcing to produce a red noise response. By red noise, we mean that variability increases with time scale until it saturates at sufficiently long time scale. It must be noted that this model assumes that atmosphere drives the ocean locally and there is no spatial coherence in the atmospheric or oceanic variability. The following equation illustrates the one-dimensional Hasselmann model for a mixed layer ocean :

$$C\frac{dT}{dt} = \eta - \lambda T, \tag{1.1}$$

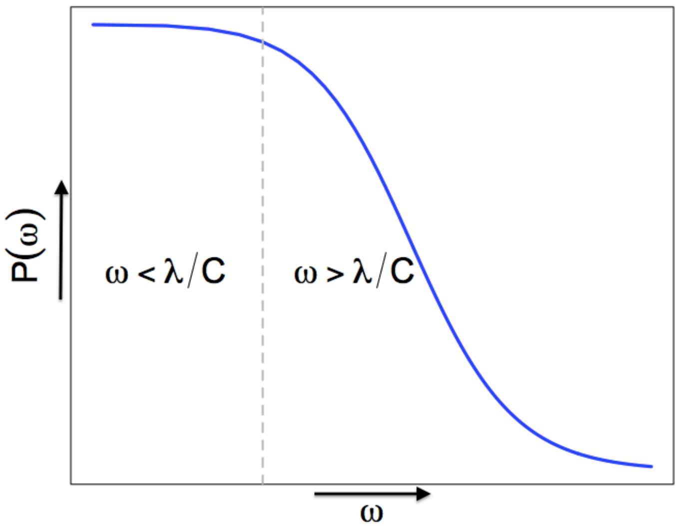

Figure 1.1: A schematic representation of power spectrum of SST from white noise atmospheric forcing.

where, T indicates the temperature anomaly of the mixed layer ocean, η is the random atmospheric forcing, C denotes the heat capacity of the ocean and λ is the damping coefficient. The damping term λT is a representation of turbulent latent and sensible heat fluxes from the ocean to the atmosphere and small scale turbulent diffusive processes.

The power spectrum of the the temperature anomaly T can be written as

$$|\tilde{T}(\omega)|^2 = \frac{\left|\frac{\tilde{\eta}(\omega)}{C}\right|^2}{\omega^2 + \left(\frac{\lambda}{C}\right)^2}. \tag{1.2}$$

Where, $\tilde{\eta}(\omega)^2$ is the power spectral density of the atmospheric forcing η. The heat capacity of the ocean is calculated as $C = \rho_0 c_p H$, where ρ_0 is the density of seawater ($\approx 1000\,\mathrm{Kgm^{-3}}$), c_p is the specific heat of seawater ($\approx 4180\,\mathrm{Jkg^{-1}K^{-1}}$), and H is the depth of the mixed layer. The damping coefficient λ has a typical value of $15\mathrm{Wm^{-2}K^{-1}}$ (Frankignoul et al., 1998). For mixed layer depth of 50m, the damping timescale $\tau_D = (\lambda/C)^{-1} \approx 5.4$months. Some previous studies have found similar timescale for mid-latitude SST (Deser et al., 2003; Hall and Manabe, 1997). A schematic representation of Eq. 1.2 is shown in fig. 1.1. For short time scales, $\omega > \lambda/C$, the variance increases as ω^{-2} with time. But for the time scales $\omega \sim \lambda/C$, the damping becomes important and for very long timescales $\omega < \lambda/C$, the variance becomes independent of frequency ω and spectrum flattens out.

Previous studies have indicated that Hasselmann model can explain variability in most of the ocean regions except where mean ocean advection or mesoscale eddies are important (Frankignoul and Hasselmann, 1977; Frankignoul and Reynolds, 1983; Hall and Manabe, 1997; Hurrell et al., 2010). For the parameter values given above, the frequency at half maximum corresponds to a period of $2\pi\tau_D \approx 3$ years. However, this timescale must not be construed as predictability timescale. A conservative definition of predictability limit is the time at which the autocorrelation function (ACF) decays by 2 e-foldings. Since the e-folding timescale of the Hasselmann model is τ_D, the 2 e-foldings is around 11 months, corresponding to an ACF of 0.135. This means that the Hasselmann model cannot predict more than $(0.135)^2 \approx 2\%$ of the variance after a lead time of $2\tau_D$ (11 months here).

Moving forward from Hasselmann's mechanism, one important question arises as to what are the relative roles of pure (intrinsic) atmospheric noise and ocean-atmospheric feedbacks in setting the timescale of SST variability on decadal timescales? Comparing the response of an ocean mixed layer model to atmospheric forcing with simulations from a fully coupled GCM, Seager et al. (2000) argue that dominant pattern of Atlantic ocean climate (tripole structure) variability can be explained as a passive response of ocean mixed layer to atmospheric forcing. Fan and Schneider (2012) and Schneider and Fan (2012) adopted interactive ensemble strategy (Kirtman and Shukla, 2002) to seperate internal atmospheric noise forcing SST from the SST variability resulting from coupled feedbacks between atmosphere and ocean. They found that the North Atlantic tripole SST variability can be explained primarily by atmospheric noise (weather noise heat flux) with important feedbacks of oceanic gyre circulation on the tripole SST. In an examination of the multidecadal mode of Atlantic multidecadal variability (AMV), Chen et al. (2016), argued that the North Atlantic Oscillation (NAO) pattern in the atmosphere, dominated by the noise component, forces the multidecadal mode through noise heat flux and noise wind stress. The noise wind stress forcing causes dynamical changes in the oceanic gyres and the AMOC that have substantial impact on the structure of the SST variability.

The Hasselmann model represented by Eq. 1.1 considers no active role of ocean. The inclusion of oceanic response to stochastic atmospheric forcing may also introduce new mechanisms for decadal variability. A simple linear, geostrophic model of the ocean forced by wind stress forcing white in time produces baroclinic response of the ocean that propagates westward at twice the Rossby wave speed. This response results in a red noise spectrum at low frequencies (Frankignoul et al., 1997). Selective excitation of some oceanic process by the atmospheric forcing with preferred large-scale spatial patterns is also proposed to be one of the mechanisms that may produce preferred timescales. For example, Weng and Neelin (1998) demonstrated in a simple midlatitude model that a preferred timescale is set by resonance between zonal length scale of atmospheric wind stress feedback and oceanic Rossby wave dynamics.

Saravanan and McWilliams (1998) added an advective ocean and a spatially coherent atmospheric forcing of the ocean to the stochastic model of the Hasselmann. The advective ocean is characterized by velocity scale V and the atmospheric forcing is characterized by spatially coherent structure with length scale L. The model solution produces two regimes. A slow regime where local damping effects dominate ocean advection. This regime is characterized by red noise spectrum with a peak only at zero frequency. The other is the fast regime in which a spectral peak emerges. To understand this mechanism, consider a dipolar standing wave pattern of atmospheric variability with white-noise temporal structure, as illustrated in fig. 1.2 taken from Saravanan and McWilliams (1998). This may be viewed in spectral space as a random superposition of oscillations with all possible periods. Let us focus on the component with period L/V. At time t =0, the atmospheric forcing would excite an oceanic temperature anomaly shown by the sinusoidal curve in panel (b). At t = L/2V, in the fast deep regime, the temperature anomaly would be displaced by a distance L/2, as shown by the dashed curve. At the same time, the spectral component of atmospheric

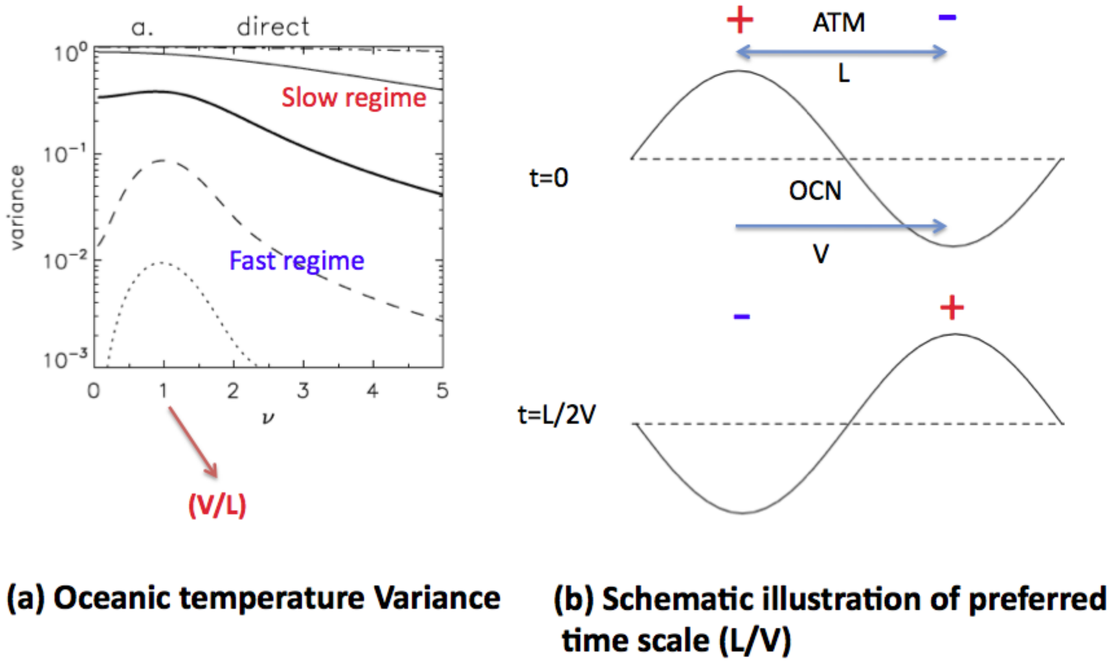

Figure 1.2: A schematic representation of generation of spectral peak under advective resonance hypothesis of Saravanan and McWilliams (1998).

forcing with period L/V would also have changed sign, leading to positive reinforcement of the SST anomaly. This positive reinforcement of SST anomaly results in the spectral peak in the fast regime as shown in the panel (a). Of course, white noise atmospheric forcing would also contain spectral components at all other possible periods, but these would not interact coherently with the ocean. This mechanism of Saravanan and McWilliams (1998) is referred to as advective-resonance hypothesis. Fig. 1.2(a) shows the frequency-variance spectrum of oceanic temperature anomaly. This shows that the slow regime exhibits a red noise type of response that flattens out as $V \to 0$. However, the fast regime shows a preferred frequency corresponding to the timescale L/V. One limitation of this mechanism is that it does not work in conditions where effects of local damping are stronger than that of the advection (Farneti and Vallis, 2011; Saravanan and McWilliams, 1997). Despite the physical plausibility of this mechanism of decadal variability, there seems to be no paper that critically tests this mechanism against observations.

Latif and Barnett (1994) proposed a mechanism in which coupled ocean atmosphere dynamics and ocean waves gives rise to new intrinsic modes of variability on longer timescales. They argued that about one-third of the low frequency climate variability in the North Pacific can be attributed to a cycle involving unstable air-sea interactions between the subtropical gyre circulation in the North Pacific and the Aleutian low-pressure system. Fig. 1.3 illustrates the mechanism involving coupled atmosphere-ocean modes in the 70-yr long simulation of coupled ECHO model from MPI. In this model, the anomalous SST in the western Pacific region shows irregular oscillatory behavior on decadal time scale (not shown here) and is dominated by large positive SST anomaly centered around 35N. The positive anomaly is surrounded by negative anomalies most prominently in the south (panel A). The atmospheric response to this SST pattern results in a positive geopotential height anomaly (panel B). The associated changes in the net heat flux (panel C) tend to reinforce the already existing warm anomaly in the central and western North Pacific region, and cold anomaly in the Equatorial Pacific . This results in positive feedback between ocean and atmosphere. However, associated changes in the wind stress curl (panel D), that is clockwise in the north and anti-clockwise in the south, tends to weaken the mean westerly wind in the North Pacific, which ultimately results in the weakening of the gyre circulation. The weakened gyre circulation leads to less transport of warmer water northward along the western boundary and into the Kuroshio extension region. This tends to reduce the warm anomaly and provides negative feedback. The spin up time of the gyre provides the delay responsible for the oscillations of a decade. Unfortunately, the mechanism of Latif and Barnett (1994) has not been reproduced in some of the later studies (e.g., Schneider et al. (2002)). Some other studies have shown that when Aleutian low strengthens, it shifts southward and thus also shifts gyre circulation equatorward, resulting into colder SST anomaly instead of warmer SST anomaly in the western Pacific. Thus the response of the western Pacific atmosphere appears to be of opposite sign than in the Latif and Barnett (1994) (Deser et al., 1999; Newman et al., 2016; Seager et al., 2001).

Another mechanism of decadal variability based on a coupled ocean-atmosphere feedback

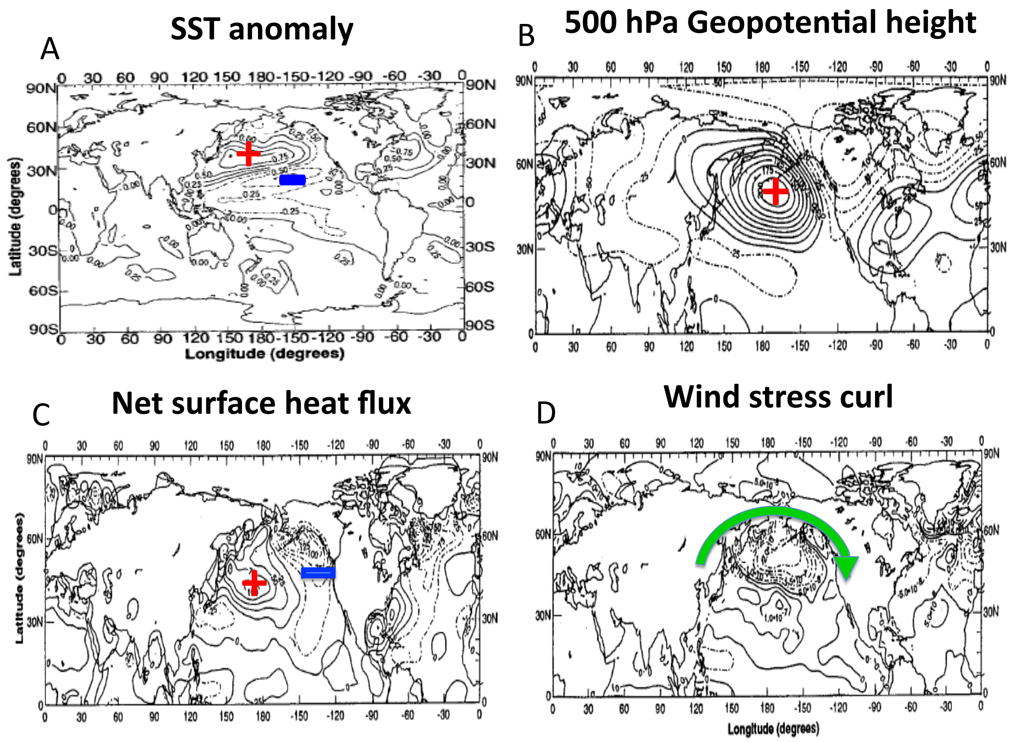

Figure 1.3: Generation of coupled atmosphere-ocean mode in the 70-yr integration of a coupled ECHO model from MPI Latif and Barnett (1994).

was proposed by Marshall et al. (2001). This mechanism involves the response of the ocean gyre and thermohaline circulation to persistent NAO anomalies. The delay offered by the gyres and/or thermohaline circulation sets the time scale of the oscillation of the coupled system. A major limitation of this model is that it is highly idealized and hence its comparison with the observations is difficult.

GCM experiments have shown that variations in the AMOC are strongly related to the variations in the SST on multidecadal timescales (Ba et al., 2014; Buckley and Marshall, 2016; Delworth and Mann, 2000; Gastineau and Frankignoul, 2012; Knight et al., 2005; Latif and Keenlyside, 2011; Latif et al., 2004). Fig. 1.4 shows the covariability of SST and the

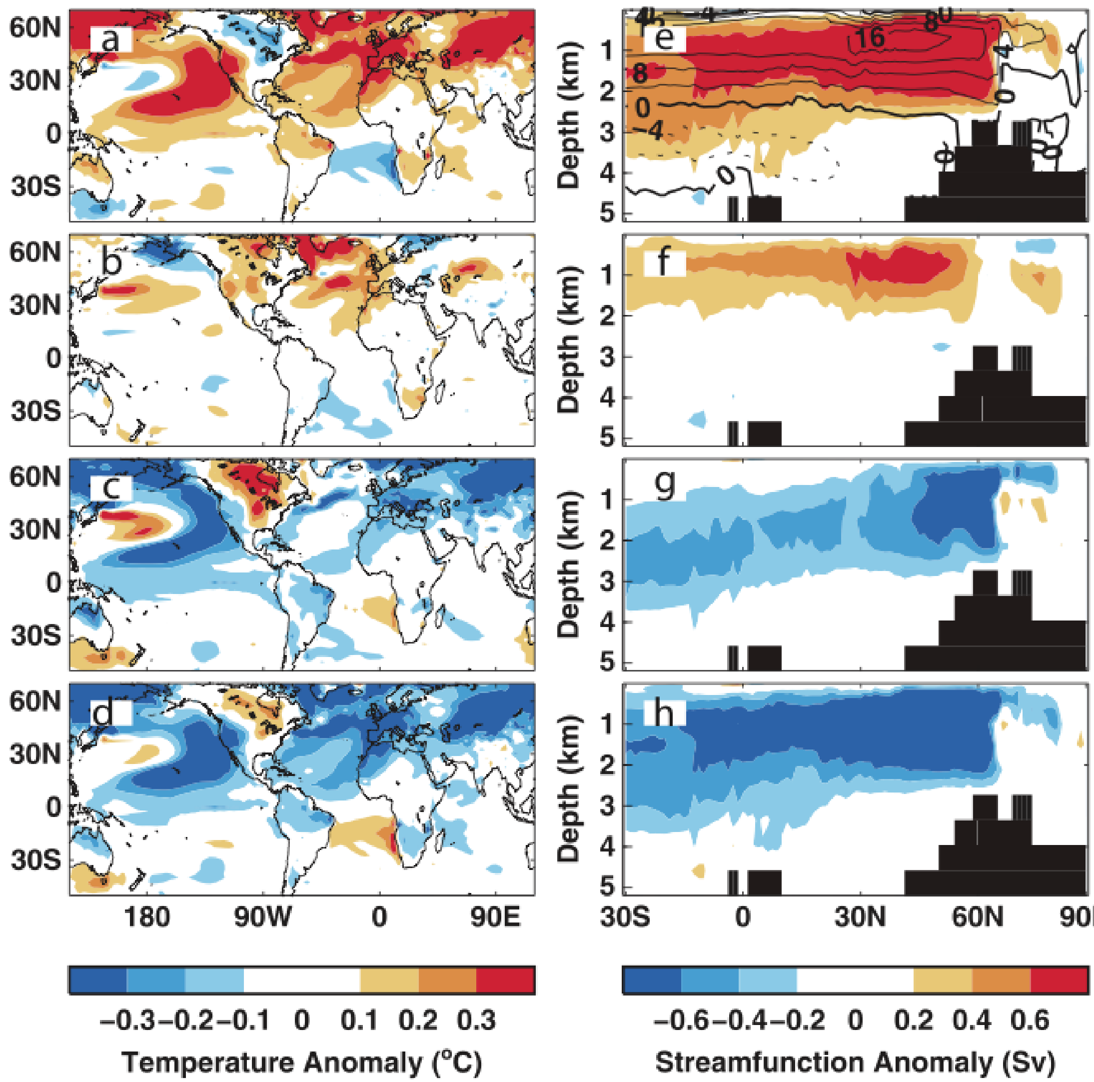

Figure 1.4: Cycles of SST and AMOC anomaly from Knight et al. (2005). Panels a-d show the signal in surface temperature anomaly in the frequency band from $(70yrs)^{-1}$ to $(180yrs)^{-1}$, at phases of 0, 60, 120, 180 respectively. Zero phase corresponds to maximum mean Northern Hemisphere temperature. Panels e-h show the corresponding phases of the covarying signal in streamfunction anomaly in the same band. In panel e, the climatological streamfunction is shown by contours, such that the mean AMOC and anomalous AMOC strength are positive (clockwise). Negative contours are dashed.

AMOC in 70-180 yrs timescales from Knight et al. (2005). It shows that widespread warm SST anomalies prevail in the Northern Hemisphere when the AMOC is at the maximum. The warm SST anomalies diminish with the decreasing strength of the AMOC. After a complete cycle, the cold SST anomalies persist in the Northern Hemisphere when the AMOC strength is minimum. The maximum positive (negative) SST anomalies have considerable similarity with the observed positive (negative) AMO pattern, thus the result shows a possible link between the AMO and the AMOC strength. Using a fully coupled atmosphere-ocean model, Timmermann et al. (1998) hypothesized that air-sea interaction involving the AMOC in the North Atlantic and upper ocean in the North Pacific can generate a low-frequency climate oscillation with a dominant period of about 35 years.

1.4 Are ocean dynamics essential for decadal predictability?

As indicated above, some studies assign a prominent role of ocean circulation to decadal variability. One reason for earlier studies to look for the active role of the ocean is that the timescale obtained from linear, local Hasselmann's model is of the order of months, hence the Hasselmann's model can not explain decadal/ multidecadal variability. Another reason is that some studies argue that Hasselmann's model is inconsistent with observations in certain regions. Specifically, Hall and Manabe (1997) argued that Hasselmann's model could be used to simulate both SST and sea surface salinity (SSS). However, SST anomalies are damped by sensible, latent, and radiative fluxes, where SSS anomalies are damped only by turbulent diffusion. Therefore SST anomalies are damped more strongly than SSS anomalies and therefore should have less proportion of variance at low frequencies. In addition, they argue that a local, linear theory of SST and SSS anomalies cannot explain coherency between these anomalies. Based on this criteria, they found that a local linear theory could be applied to most of the world oceans except in the North Atlantic, Southern Oceans and in the Equatorial Pacific regions.

Technically speaking, coherency between SST and SSS anomalies can be explained by a local linear theory by adding coherence in the stochastic forcing. Such coherence in the noise can be justified by the fact that an evaporative forcing must cause a *simultaneous* change in SST and SSS. More importantly, disproving a local, linear theory for SST does not prove that ocean dynamics are essential for decadal variability. In particular, the atmosphere interacts with the SST in a way that has spatial coherence, but this interaction is not included in the Hasselmann model. In other words, it might be the atmosphere that violates the local, linear theory, not the ocean.

The hypothesis that spatially coherent atmospheric responses to SST can generate decadal variability without interactive ocean circulations can be tested using an atmospheric global circulation model (AGCMs) coupled to a slab ocean mixed layer. For instance, Clement et al. (2015) showed that many features of the AMO, such as the spatial structure, surface winds, and surface pressure, can be simulated by such models. In this model, AMO-like variability is generated by pure atmospheric noise that projects on the North Atlantic Oscillation (NAO).

Surface fluxes (latent heat flux, sensible heat flux, and shortwave and longwave fluxes) play a central role in thermodynamically coupled atmosphere-ocean system. Surface heat fluxes generate SST anomalies, and SST anomalies, in turn, can modulate surface heat fluxes. This cyclic process is called surface heat flux feedback. Park et al. (2005) estimated the surface heat flux feedback to underlying SST anomalies from observational records and found that the net surface heat flux feedback are in general negative, i.e., they tend to reduce the underlying SST anomalies. However, certain components of the surface heat flux feedback can be positive depending on the season and location, thus enhancing month-to-month persistence of SST anomalies. For example, a net positive surface heat flux feedback occurs in the Indian ocean region during boreal summer and fall. Park et al. (2005) proposed the following mechanism to explain this finding. A warm SST anomaly is accompanied by low atmospheric pressure at the surface. This low pressure induces anomalous cross-equatorial flow, tending to oppose the background trade wind. The weakening of trade winds results in the reduced sensible and latent heat fluxes which in turn reinforces the original positive SST anomaly.

Another striking example of positive surface heat flux feedback occurs in the subtropical stratocumulus ocean regions. In these regions, enhanced/ reduced stratus clouds persist over negative/positive SST anomalies, that cause reduced/ increased solar radiation reaching at the ocean surface, thus providing for the positive shortwave feedback. Bellomo et al. (2014), in their AGCM coupled to the ocean mixed layer, showed that a positive cloud-SST feedback enhances the persistence and variance of the leading modes of climate variability at decadal and longer time scales.

Other studies based on integrations of atmospheric global circulation models (AGCMs) coupled to a slab ocean mixed layer demonstrate that only intrinsic atmospheric circulations and air-sea interaction through sensible, latent and radiative fluxes can generate variability predictable on interannual and longer timescales (Clement et al., 2011; Deser et al., 2004; Dommenget, 2010; Dommenget et al., 2014; Dommenget and Latif, 2008). Moreover, Newman et al. (2016) using a regression model showed that a large fraction (50-60%) of the PDO can be explained by random atmospheric forcing and ENSO teleconnection from the tropics. However, this model is different from the typical Hasselmann model in the sense that the white noise atmospheric forcing implicitly has spatial structure that projects on the PDO. Moreover, the ENSO forcing has coherent structure both in space and time.

However, mechanism of decadal variability in atmospheric models coupled to a slab ocean mixed layer is under debate. For example, the mechanism of the AMO variability proposed by Clement et al. (2015) is challenged on the ground that the direction of the net surface heat flux in coupled models and observations is opposite to that in the slab models and is such that it opposes the SST tendency, so the net surface heat flux in coupled models tend to damp the SST anomaly and not to cause persistence of the SST anomaly (Gulev et al., 2013; O'Reilly et al., 2016; Zhang et al., 2016). On the other hand, Clement et al. (2016) argue that on decadal timescales the net heat flux is nearly balanced by the net ocean heat transport convergence making the tendency in temperature nearly zero. Therefore any causality based upon the role of net surface heat fluxes or the ocean heat convergence can not be established. Moreover, a recent study argues that ocean dynamics play a key role in decadal climate variability once air-sea interactions associated with ocean fronts and eddies are resolved (Siqueira and Kirtman, 2016).

1.5 Research objectives

It is clear from the above competing arguments that a unified and satisfactory theory of decadal variability and predictability is still lacking. Nevertheless, there is substantial evidence that decadal variability can be generated in models without interactive ocean circulations. Therefore, it is of interest to document the kinds of decadal variability that can arise in such models. Previous studies have documented this variability in terms of pre-defined indices associated with the AMO, PDO, and ENSO. In this project, we identify the most predictable component in an objective manner in models with and without ocean dynamics. Differences between these patterns indicate a role for ocean dynamics. In addition, we go beyond pure-model results and attempt to validate these components in observations.

This thesis is arrange in the following manner. First, our methodology for identifying the most predictable components is reviewed in chapter 2. In chapter 3, we address the following questions. What are the dominant patterns of decadal predictability in systems without ocean dynamics? Are these patterns similar to those of systems that capture ocean dynamics? Do the patterns derived from systems with and without interactive ocean dynamics have similar time scales? How would multiyear predictions by the two systems compare in terms of skill? We will answer these questions by identifying the most predictable components in two types of models: models with interactive ocean dynamics, and models without interactive ocean dynamics (i.e., models with a 50m ocean slab mixed layer). The predictability is estimated by fitting a linear regression model to model output, and then determining the most predictable components of the resulting regression models. These regression models also are used to make retrospective forecasts of observations. We will quantify the skill of these forecasts and compare the skill for regression derived from the two types of models.

In addition, we will also investigate predictability and skill of individual models. We will investigate whether some models are outliers, in the sense that their predictability and skill differs a lot from their multimodel mean. We will also determine whether some models have especially high skill or especially low skill. We will also examine whether some of the conclusions found in the multi-model analysis in chapter 3 also hold on model-by-model basis. These questions will be answered in chapter 4. Since each model has a unique representation of natural climate system, the nature of slowly varying components is different in each model. Our analysis will help identify models that have predictability and forecast skills and hence motivate future studies to identify the physical processes that are important for decadal variability and predictability.

In addition to investigating decadal predictability, we have also built a simple stochastic model of atmosphere coupled to a slab ocean mixed layer. The reason is that although much progress has been made using nonlinear AGCMs coupled to ocean mixed layer models, these models still are difficult to interpret owing to their nonlinearity and chaotic variability. On the other hand, Hasselmann-type models use simplistic atmospheric models that do not have spatially coherent responses to ocean temperature anomalies. Accordingly, we develop a model that is intermediate between the one-dimensional Hasselmann model and nonlinear AGCM-mixed layer. In particular, we build a stochastically forced, linearized primitive equation model coupled to a slab mixed layer ocean model. Since the proposed stochastic model is fundamentally linear, it is potentially easier to understand mechanisms in this model. This model is discussed in chapter 5.

Chapter 2: Methodology: Average Predictability Time Analysis

2.1 Overview

This chapter describes the methodology used for our research. We have adopted a measure of multivariate predictability called the average predictability time (APT) proposed by DelSole and Tippett (2009a,b). We have also used method of Laplacian eigenfunctions (DelSole and Tippett, 2015) to compute the APT in the Laplacian space. This approach of computing APT in the Laplacian space is new and has many advantages that are discussed in the subsequent section. Though the method of APT is a standard procedure, it is instructive to explain in detail the method of APT in order to comprehend how the method of APT is applied in the framework of Laplacian eigenfunctions.

2.2 A generalized measure of predictability

We are familiar on everyday basis that skill of weather forecast decays with time. This point is illustrated in fig. 2.1 taken from Simmons and Hollingsworth (2002). In this figure, the solid black curve is the standard deviation of the forecast error of the 500hPa geopotential height as a function of lead time (days) and the solid red curve is the saturation limit of the forecast. The figure shows that the forecast error starts out small, grows monotonically with time and finally saturates in around two weeks time. A measure of forecast skill is the closeness between the error curve and its saturation value. Note that the forecast skill as shown in fig. 2.1 is not only due to the difference between observation and forecast but also due to the fact that dynamical prediction models themselves are not perfect and observations also have uncertainties.

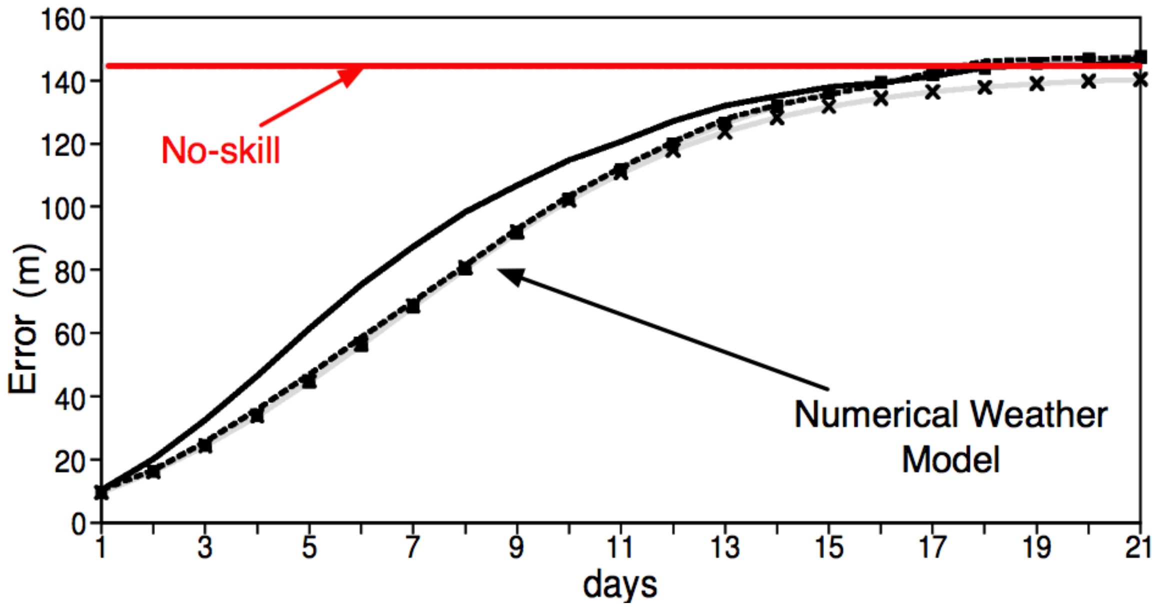

Figure 2.1: Forecast error of the 500hPa geopotential height in ECMWF weather prediction model. Standard deviation of T255L40 forecast errors (solid, black) and differences between successive forecasts (dashed, black) for the forecast range up to 21 days, for northern hemisphere forecasts verifying in the period 12 December 2000 to 11 March 2001. Also includes the curves (solid, grey) that result from fitting the three-parameter error-growth model to the differences over 21 days (square marker symbols) and 10 days (crosses) and the asymptotic limit derived from the variance of analyses (red line). From Simmons and Hollingsworth (2002).

We are interested in measuring the goodness of a forecast in the ideal case where observational errors can be neglected and forecast model is the same as that used to generate the truth. This framework is called a “prefect model” framework and provides the basis for quantifying predictability. It should be noted that perfect model framework does not mean the forecast is perfect in the sense of having no uncertainty- it is still not free from model error. Our aim is to define a generalized measure of predictability that can be used for both univariate and multivariate systems.

Suppose $X_{i+\tau}$ is a member of an infinite ensemble of forecasts initialized at time i and integrated for lead time τ. The ensemble mean of the forecast is denoted as

$$\mu_{\tau,i} = E_{|i}[X_{i+\tau}], \tag{2.1}$$

where, $E_{|i}$ represents the ensemble mean for fixed initial condition i. A measure of ensemble spread is the variance about the ensemble mean, expressed as

$$\sigma^2_{\tau,i} = E_{|i}[(X_{i+\tau} - \mu_{i,\tau})^2]. \tag{2.2}$$

Note that the ensemble mean and ensemble spread are functions of initial condition i. We can compute ensemble spread averaged over all initial conditions. The result is called mean square error (of a perfect model) and denoted as σ^2_τ, defined as

$$\sigma^2_\tau = E_i[\sigma^2_{\tau,i}], \tag{2.3}$$

where E_i is the average over all inital conditions. Fig. 2.1 illustrates a generic feature of predictability: forecast error increases with lead time and saturates for infinitely large lead time. Therefore, forecast error variance σ^2_τ also increases with lead time and reaches a saturation value, say σ^2_∞, in the limit $\tau \to \infty$. In the limit of $\tau \to \infty$, forecast (and hence forecast distribution) is assumed to be independent of initial condition. It can be shown that if forecast distribution is independent of initial condition, the forecast distribution must be climatological distribution in a prefect model framework. Hence, the saturation error variance σ^2_∞ must also be the climatological error variance.

We define a measure of predictability as

$$P_\tau = 1 - \frac{\sigma^2_\tau}{\sigma^2_\infty}. \tag{2.4}$$

By definition, P_τ varies between 1 and 0. If there is no forecast uncertainty in the beginning, then $\sigma^2_\tau = 0$ for $\tau = 0$. Therefore, It follows from the Eq. 2.4, $P_\tau = 1$ at lead time $\tau = 0$. σ^2_τ increases with lead time and becomes equal to the climatological error variance σ^2_∞ at lead time $\tau \to \infty$. Thus predictability measure P_τ decays monotonically with lead time and decays to zero at asymptotically large lead time $\tau \to \infty$.

2.3 Predictability of univariate systems

Eq. 2.4 gives one way of defining predictability. However there exist several other measures of predictability such as signal-to-noise ratio, mean square error, correlation between ensemble members, multiple correlation and autocorrelation. These different measures of predictability are not really independent but are equivalent to each other for gaussian distributions. It can be shown that all these different measures of predictability are monotonic functions of the measure P (Jia, 2011).

However, one practical limitation of these measures of predictability is that they are applicable only in univariate cases where predictability of a scalar variable is estimated on a grid by grid point basis. In climate studies, one is often concerned with estimating predictability over a geographical region or for a combination of variables. In such cases a combination of more than one variables are involved (multivariate systems). Therefore we need a method that accounts for multivariate predictability.

2.4 Predictability of multivariate systems

The basic idea of predictability of a multivariate systems is to find a linear combination of variables that maximizes P_τ, as expressed in the Eq. 2.4. This framework for estimating predictability is in general called "Predictable component analysis (PrCA)". PrCA is basically the multivariate generalization of ANOVA and essentially the same as Multivariate Analysis of Variance (MANOVA). PrCA effectively decomposes an ensemble forecast into a sum of components ordered such that the first maximizes predictability, the second maximizes predictability subject to being uncorrelated with the first, and so on. The method of PrCA is not new and its equivalent forms have been used in several previous studies. In an insightful paper, DelSole and Chang (2003) showed that different measures used by Déqué (1988), Renwick and Wallace (1995) and Schneider and Griffies (1999) are equivalent to PrCA.

One limitation of PrCA is that it maximizes predictability at fixed lead times and hence it gives information about predictability dependent on lead time. However it is possible that predictabilities at different lead times may remain in the same space and there is no reason to prefer one lead time over the other for characterizing predictability of a system. Therefore, we would like to derive a measure that compares predictability independent of lead time. The average predictability time (APT) proposed by DelSole and Tippett (2009a,b) is a method that overcomes the limitations of PrCA. The APT characterizes predictability of a system independent of lead time hence can be effectively used to compare lead time-independent-predictability of two systems.

2.5 Average predictability time

The APT is a method of diagnosing overall predictability of a system. It is basically an "integral time scale" that is based upon the integral of a predictability measure over all lead times. The integral time scale is not a new concept and is already used in the field of turbulence to define eddy time scales. The APT is defined as the integral of the predictability measure P_τ, as expressed in the Eq. 2.4,

$$APT = 2\int_{\tau=0}^{\infty} P_\tau d\tau. \tag{2.5}$$

The factor of 2 is introduced to ensure that APT agrees with the e-folding time of a time series. For discrete time, APT is defined as

$$APT = 2\sum_{\tau=\mathbf{1}}^{\infty} P_\tau \Delta_\tau \tag{2.6a}$$

$$= 2\sum_{\tau=\mathbf{1}}^{\infty} \left(1 - \frac{\sigma_\tau^2}{\sigma_\infty^2}\right) \Delta_\tau, \tag{2.6b}$$

where Δ_τ is the difference between two successive lead times.

Instead of considering a scalar $X_{i+\tau}$, we now consider a vector of random variables $\mathbf{x}_{i+\tau}$

of length N. We are interested in finding a linear combination of these random variables that maximizes APT. Let $\mathbf{q}$ be the coefficient vector for the combination of variables, then a component is derived by the inner product $\mathbf{q}^T\mathbf{x}_{i+\tau}$. The ensemble mean of the forecast associated with the component $\mathbf{q}^T\mathbf{x}_{i+\tau}$ can be written as

$$\boldsymbol{\mu}_{\tau,i} = E_{|i}[\mathbf{q}^T\mathbf{x}_{i+\tau}], \tag{2.7}$$

and the ensemble spread as

$$\begin{aligned}
\sigma^2_{\tau,i} &= E_{|i}[(\mathbf{q}^T\left(\mathbf{x}_{i+\tau} - E_{|i}[\mathbf{x}_{i+\tau}]\right)\left(\mathbf{x}_{i+\tau} - E_{|i}[\mathbf{x}_{i+\tau}]\right)^T\mathbf{q}] \\
&= \mathbf{q}^T E_{|i}[(\left(\mathbf{x}_{i+\tau} - E_{|i}[\mathbf{x}_{i+\tau}]\right)\left(\mathbf{x}_{i+\tau} - E_{|i}[\mathbf{x}_{i+\tau}]\right)^T]\mathbf{q} \\
&= \mathbf{q}^T\boldsymbol{\Sigma}_{\tau,i}\mathbf{q},
\end{aligned} \tag{2.8}$$

where, $\boldsymbol{\Sigma}_{\tau,i}$ is the covariance matrix of the forecast ensemble and is the multivariate generalization of the univariate ensemble spread $\sigma^2_{\tau,i}$ expressed in 2.2.

The mean square error can be written as

$$\begin{aligned}
\sigma^2_{\tau} &= E_i[\sigma^2_{\tau,i}] \\
&= E_i[\mathbf{q}^T\boldsymbol{\Sigma}_{\tau,i}\mathbf{q}] \\
&= \mathbf{q}^T E_i[\boldsymbol{\Sigma}_{\tau,i}]\mathbf{q}] \\
&= \mathbf{q}^T\boldsymbol{\Sigma}_{\tau}\mathbf{q}.
\end{aligned} \tag{2.9}$$

Where $\boldsymbol{\Sigma}_{\tau}$ is the covariance matrix of the forecast error. Since the forecast error increases with lead time, $\boldsymbol{\Sigma}_{\tau}$ also increases with lead time and saturates to $\boldsymbol{\Sigma}_{\infty}$ for asymptotically infinite lead time $\tau \to \infty$. As discussed above, in the limit of $\tau \to \infty$, the saturation error variance must be the climatological error variance, which can be written as

$$\sigma_\infty^2 = \mathbf{q}^T \mathbf{\Sigma}_\infty \mathbf{q}. \tag{2.10}$$

Substituting Eqs. 2.9 and 2.10 in Eq. 2.6b gives

$$APT = 2\sum_{\tau=\mathbf{1}}^{\infty} \left(1 - \frac{\mathbf{q}^T \mathbf{\Sigma}_\tau \mathbf{q}}{\mathbf{q}^T \mathbf{\Sigma}_\infty \mathbf{q}}\right) \Delta_\tau \tag{2.11a}$$

$$= \frac{\mathbf{q}^T \mathbf{G} \mathbf{q}}{\mathbf{q}^T \mathbf{\Sigma}_\infty \mathbf{q}}, \tag{2.11b}$$

where,

$$\mathbf{G} = 2\sum_{\tau=\mathbf{1}}^{\infty} \left(\mathbf{\Sigma}_\infty - \mathbf{\Sigma}_\tau\right) \Delta_\tau \tag{2.12}$$

Recall that APT is defined as the integral of a predictability measure. It follows from comparing eqs. 2.6a and 2.11a that the predictability measure is

$$R_\tau^2 = \left(1 - \frac{\mathbf{q}^T \mathbf{\Sigma}_\tau \mathbf{q}}{\mathbf{q}^T \mathbf{\Sigma}_\infty \mathbf{q}}\right). \tag{2.13}$$

R_τ^2 is the multivariate generalization of the Eq. 2.4. We define “the limit of predictability” as when R_τ^2 decays to zero.

The eq. 2.11b is a Rayleigh coefficient. According to a standard theorem in linear algebra (Noble and Daniel, 1988) maximizing Rayleigh coefficient in Eq. 2.11b leads to a generalized eigenvalue problem

$$\mathbf{G}\mathbf{q} = \lambda \mathbf{\Sigma}_\infty \mathbf{q} \tag{2.14}$$

The set of eigenvectors obtained from solving the generalized eigenvalue problem 2.14 are the coefficient vectors $\mathbf{q}_1,\ \mathbf{q}_2,\ \cdots\ \mathbf{q}_S$. The eigenvalues corresponding to $\mathbf{q}_s$ are the APT values (in the units of time) ordered from the largest to the smallest ($\lambda_1,\ \lambda_2,\ \cdots\ \lambda_S$ such that $\lambda_1 >$

$\lambda_2 > \cdots > \lambda_S$). The coefficient vectors can be written in matrix form as

$$\mathbf{Q} = [\mathbf{q}_1 \quad \mathbf{q}_2 \quad \cdots \quad \mathbf{q}_S] \tag{2.15}$$

The matrices $\mathbf{G}$ and Σ_∞ are symmetric and therefore solving Eq. 2.14 produces components that are uncorrelated (derived rigorously in Jia (2011)). It is convenient to assume that the climatological variance of each component is unit, i.e.,

$$\mathbf{q}_k^T \Sigma_\infty \mathbf{q}_k = 1 \qquad \text{or} \qquad \mathbf{Q}^T \Sigma_\infty \mathbf{Q} = \mathbf{I}. \tag{2.16}$$

It can be shown that the first component maximizes APT, the second component maximizes APT subject to being uncorrelated to the first component as so on. The time series associated with a predictable component is called "variate" and is defined as

$$\mathbf{r}_{i+\tau} = \mathbf{Q}^T \mathbf{x}_{i+\tau}, \tag{2.17}$$

where $\mathbf{r}_{i+\tau}$ is a set of variates, i.e.,

$$\mathbf{r} = [r_1 \quad r_2 \quad \cdots \quad r_S] \tag{2.18}$$

The variates, associated with each coefficient vector $\mathbf{q}_1, \mathbf{q}_2 \cdots \mathbf{q}_S$, are uncorrelated with each other as a natural consequence of matrices $\mathbf{G}$ and $\boldsymbol{\Sigma}_\infty$ being symmetric. The variates also have unit variance following the assumption (2.16). Therefore,

$$E[r_i r_j] = 0 \qquad \text{and} \qquad E[r_i r_i] = 1, \tag{2.19}$$

where E denotes average over all ensembles and over all initial conditions. The above relations can be written equivalently as

$$E[\mathbf{r}\mathbf{r}^T] = \mathbf{I}. \tag{2.20}$$

The spatial pattern of the predictable components is called “loading vector”. Because the columns of $\mathbf{Q}$ are linearly independent, $\mathbf{Q}$ is invertible, therefore we can invert Eq. 2.17 to express the random variable $\mathbf{x}$ in terms of a linear combination of variates as

$$\mathbf{x}_{i+\tau} = \mathbf{Q}^{T^{-1}} \mathbf{r}_{i+\tau}. \tag{2.21}$$

We define loading vectors $\mathbf{P}$ as

$$\mathbf{P} = \mathbf{Q}^{T^{-1}}, \tag{2.22}$$

So, the Eq. 2.21 becomes

$$\mathbf{x}_{i+\tau} = \mathbf{P}\, \mathbf{r}_{i+\tau}. \tag{2.23}$$

Now using the identity 2.19, the loading vectors $\mathbf{P}$ can be written as

$$\mathbf{P} = E[\mathbf{x}_{i+\tau}\, \mathbf{r}^{T}_{i+\tau}]. \tag{2.24}$$

Eq 2.24 shows that loading vectors $\mathbf{P}$ can also be defined as projection of variates $\mathbf{r}$ on the data $\mathbf{x}$. Note that $\mathbf{P}$ is a set of component loading vectors, i.e.,

$$\mathbf{P} = [\mathbf{p}_1 \quad \mathbf{p}_2 \quad \cdots \quad \mathbf{p}_N]. \tag{2.25}$$

It is important to note that the loading vectors $\mathbf{p}_s$ are not orthogonal to each other. Eq. 2.24 shows that APT decomposes the data into a set of uncorrelated components, the state $\mathbf{x}$ can be represented as

$$\mathbf{x} = \mathbf{p}_1 \left(\mathbf{q}_1^T \mathbf{x}\right) + \mathbf{p}_2 \left(\mathbf{q}_2^T \mathbf{x}\right) + ... + \mathbf{p}_k \left(\mathbf{q}_k^T \mathbf{x}\right), \tag{2.26}$$

Thus it is apparent that decomposition based on APT is analogous to principal component analysis, except that instead of decomposing variance we decompose predictability.

2.6 Regularization procedure

In most climate science applications the spatial dimension far exceeds the temporal dimension. As a result the covariance matrices are singular (i.e., they have no inverse). This causes difficulty in solving the generalized eigenvalue problem 2.14. Moreover, all multivariate optimization problems suffer from overfitting - that is, using too many parameters for optimization in a sample leads to overfitting of variability that is not verified in a different independent sample. The standard approach to solve these problems is to project the data onto a lower dimensional space such as a space spanned by leading empirical orthogonal functions (EOFs) of the data. Unfortunately, EOFs are data dependent and therefore change as the time period or data source change. This dependence makes comparisons across multiple datasets and time periods difficult. Another issue with eigenvalue decomposition is that EOFs tend to overfit variance. Therefore statistical inferences based on EOFs are not straightforward (DelSole and Tippett, 2015; Giannakis and Majda, 2012; Lawley, 1956).

We have used the eigenfunctions of the Laplacian operator using the method developed by DelSole and Tippett (2015). This method effectively captures large-scale features and filters out small spatial structures. This property of Laplacian eigenfunctions makes it useful as many of the components of natural climate variability such as the PDO, AMO and ENSO are characterized by large coherent spatial patterns. Another important property of the Laplacian eigenfunctions is that they depend only on the geometry of the domain, in contrast to commonly used EOFs. Hence they are independent of data facilitating comparisons across models and data sets. In this study we derived Laplacian eigenfunctions over ocean on $5^\circ \times 5^\circ$ domain bounded by $50^\circ S$ to $60^\circ N$. The first four Laplacian eigenfunctions are shown in 2.2. The first Laplacian corresponds to an area average of the quantity projected on the Laplacian eigenfunctions. The subsequent patterns are arranged in decreasing order of their length scales. The eigenfunctions are orthogonal with respect to an area weighted norm and

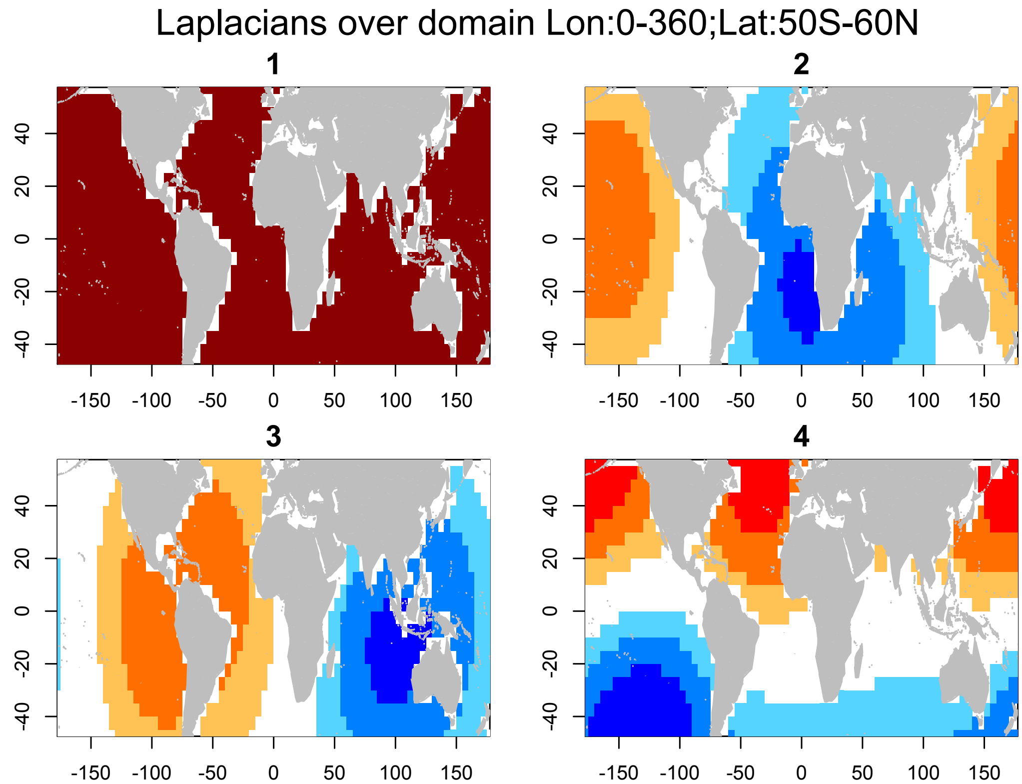

Figure 2.2: The first four Laplacian eigenfunctions derived from the Greens function method over ocean on $5^\circ \times 5^\circ$ domain bounded by $50^\circ S$ to $60^\circ N$. The patterns are orthogonal with respect to an area-weighted inner product and normalized such that the area-averaged square =1.

thus the least squares amplitude of each eigenfunction can be obtained by projection. The appropriate number of basis vectors to use in a problem depends on the problem. Thus, this question is postponed until the next chapter.

Chapter 3: APT Analysis of Coupled and Slab Models: Multimodel Analysis

3.1 Motivation

Most studies have investigated predictability of certain predefined structures such as the AMO, PDO and AMOC. These indices have proven useful for studying decadal predictability, but they were not specifically optimized for studying decadal predictability. For instance, the AMO is merely a spatial average over the Atlantic while the PDO is merely a leading EOF, which maximizes variance, not predictability. In this chapter, we discuss a method for finding components that maximize predictability. In addition, as discussed in the chapter 1, the precise role of ocean dynamics in decadal predictability is under debate. In this chapter we attempt to address these outstanding issues. In particular we attempt to answer following questions. What are the dominant patterns of decadal predictability in systems without ocean dynamics? Are these patterns similar to those of systems that capture ocean dynamics? Do the patterns derived from systems with and without interactive ocean dynamics have similar time scales? How would multiyear predictions by the two systems compare in terms of skill?

3.2 Model and Data

The model data analyzed in this study are monthly 2m-temperature (tas) from simulations of 13 models from the Coupled Model Intercomparison Project 3 (CMIP3). We explicitly chose CMIP3 models for our study as they contain two different simulations; one involving fully interactive ocean dynamics and the other without interactive ocean dynamics. The later generation of CMIP does not have simulations without interactive ocean dynamics.

Table 3.1: List of CMIP3 models used for this study

Model	Length of slab-ocean models (years)	Length of fully coupled models (years)	Resolution
$CCCMA\_CGCM3\_1$	30	500	$3.75° \times 3.75°$
$CCCMA\_CGCM3\_1\_T63$	30	350	$2.8° \times 2.8°$
$CSIRO\_MK3\_0$	60	380	$1.875° \times 1.875°$
$GFDL\_CM2\_0$	50	500	$2.0° \times 2.5°$
$GFDL\_CM2\_1$	100	500	$2.0° \times 2.5°$
$GISS\_MODEL\_E\_R$	120	500	$3.9° \times 5.0°$
$INMCM3$	60	330	$4.0° \times 5.0°$
$MIROC3\_2\_HIRES$	20	500	$1.125° \times 1.125°$
$MIROC3\_2\_MEDRES$	60	100	$2.8125° \times 2.8125°$
MPI_ECHAM5	180	1000	$3.75° \times 3.75°$
$MRI\_CGCM2\_3\_2A$	100	350	$2.8° \times 2.8°$
$NCAR\_CCSM3$	450	500	$0.90° \times 1.25°$
$UKMO\_HADGEM1$	70	240	$1.25° \times 1.75°$

The term "interactive ocean dynamics" represents the dynamical processes of the ocean such as variations in the mixed layer depth, ocean currents, gyre circulation and vertical deep ocean circulation, that vary in response to atmospheric variabilities and in turn provide feedback to the atmosphere. In CMIP3 both the simulations are control runs in which external forcing is held fixed at their preindustrial settings, ensuring that the only mechanism for decadal predictability is internal variability. The first set comes from fully coupled climate models with interacting atmosphere, land, ocean and sea ice components; these models will be called coupled. The other set of simulations uses the same atmospheric model as in the coupled simulations, but the ocean model is a 50-m-deep slab mixed layer model; these models will be called slab. Although the slab model has a periodically varying ocean heat transport (the so-called Qflux), this transport is noninteractive in the sense that it is a prescribed function of time and is independent of the ocean-atmosphere variability. Thus, the slab model contains no interactive ocean dynamics. Further details of the models are given in Table 3.1.

The observed monthly SST is from ERSSTv3b (Smith et al., 2008) for the period 1901-2015. The observed Nino3.4 index is from the HadISST1 (Rayner et al., 2003) It is the area averaged SST from 5S-5N and 170-120W (`https://www.esrl.noaa.gov/psd/gcos_wgsp/Timeseries/Nino34/`). The observed AMO index is the 12-month running mean index using Kaplan SST V2 (`https://www.esrl.noaa.gov/psd/data/timeseries/AMO/`). The PDO index is downloaded from University of Washington/JISAO (`http://research.jisao.washington.edu/pdo/PDO.latest`). All indices have been smoothed using a 12-month running mean. We have used monthly sea surface temperatures because the difference between 2m-air temperature and surface temperature is negligible on monthly or longer timescales.

Since some of the slab models simulations were relatively short (some last only for 20 years), we maximized APT by pooling model data together. This makes the sample size very large.

3.3 Regularization

In order to minimize overfitting we projected the data onto a space spanned by Laplacian eigenfunctions. Laplacian eigenfunctions were derived on a $5° \times 5°$ domain bounded by $50°S - 60°N$. The eigenfunctions are orthogonal with respect to an area weighted norm and thus the least squares amplitude of each eigenfunction can be obtained by projection. The eigenfunctions were truncated to ten (a justification is made in the *Results* section) and projected onto monthly temperature fields of each model and simulation. The resultant time series were centered, detrended and seasonally adjusted, yielding a data matrix $\mathbf{X}_t$ of dimension $10 \times N$, where N is the number of months. The time lagged covariance matrix of a single model is written as

$$\mathbf{C}_\tau^m = \frac{1}{N} \sum_{t=1}^{N-|\tau|} \mathbf{X}_{t+|\tau|} \mathbf{X}_t^T, \tag{3.1}$$

where, $\tau = 0, \pm1, \pm2......$, and the superscript T denotes the matrix transpose. Covariances were computed for each model and simulation separately. A similar procedure was performed on monthly observed SST data, except that instead of removing a trend, a best-fit third order polynomial was subtracted to remove most of the forced signal, yielding Laplacian timeseries $\mathbf{Y}_t$ and time lagged covariance matrix $\mathbf{C}_\tau^{\text{obs}}$.

3.4 APT for linear regression models

Decadal predictions from CMIP3 dynamical models are not available. But, we can compute prediction skill of models using regression methods. Accordingly, following DelSole and Tippett (2009b) we estimate a regression model using data from individual model and then analyze predictability of that regression model. Some caveats regarding this approach are discussed at the end of this chapter. In our approach a linear model is used to predict the future amplitude of ten Laplacian eigenfunctions based on their values of the present value. The regression model is defined as

$$\hat{\mathbf{X}}_{t+\tau} = \mathbf{L}_\tau^m \mathbf{X}_t, \tag{3.2}$$

where τ is lead month and the caret $\hat{}$ denotes a prediction. $\mathbf{L}_\tau^m$ is a matrix, called the prediction operator, that depends on lead time τ and model m. The least squares estimate of the prediction operator $\mathbf{L}_\tau^m$ is

$$\mathbf{L}_\tau^m = \mathbf{C}_\tau^m \mathbf{C}_0^{m^{-1}}. \tag{3.3}$$

The multimodel average covariance matrix is defined as

$$\mathbf{C}_\tau = \frac{1}{M} \sum_{m=1}^{M} \mathbf{C}_\tau^m, \tag{3.4}$$

where M is the total number of models (in this study, 13).

The multimodel prediction operator $\mathbf{L}_\tau$ can be written in the same way as in the Eq. 3.3

$$\mathbf{L}_\tau = \mathbf{C}_\tau \mathbf{C}_0^{-1} \tag{3.5}$$

Computing multimodel mean covariance matrix is effectively equivalent to pooling the model data together. It is worth mentioning here that the prediction operators are estimated from dynamical model simulations without using any observations, and is estimated for each lead month separately.

The covariance matrix of the forecast error in each model is

$$\begin{aligned}
\mathbf{\Sigma}_\tau^m &= \frac{(\hat{\mathbf{X}}_{t+\tau} - \mathbf{X}_{t+\tau})(\hat{\mathbf{X}}_{t+\tau} - \mathbf{X}_{t+\tau})^T}{N} \\
&= \frac{(\hat{\mathbf{X}}_{t+\tau}\hat{\mathbf{X}}_{t+\tau}^T - \hat{\mathbf{X}}_{t+\tau}\mathbf{X}_{t+\tau}^T - \mathbf{X}_{t+\tau}\hat{\mathbf{X}}_{t+\tau}^T + \mathbf{X}_{t+\tau}\mathbf{X}_{t+\tau}^T)}{N} \\
&= \mathbf{L}_\tau^m \mathbf{C}_0^m \mathbf{L}_\tau^{m^T} - \mathbf{L}_\tau^m \mathbf{C}_\tau^{m^T} - \mathbf{C}_\tau^m \mathbf{L}_\tau^{m^T} + \mathbf{C}_0^m \\
&= \mathbf{C}_\tau^m \mathbf{C}_0^{m^{-1}} \mathbf{C}_\tau^{m^T} - \mathbf{C}_\tau^m \mathbf{C}_0^{m^{-1}} \mathbf{C}_\tau^{m^T} - \mathbf{C}_\tau^m \mathbf{C}_0^{m^{-1}} \mathbf{C}_\tau^{m^T} + \mathbf{C}_0^m \\
&= \mathbf{C}_0^m - \mathbf{C}_\tau^m \mathbf{C}_0^{m^{-1}} \mathbf{C}_\tau^{m^T},
\end{aligned} \tag{3.6}$$

where in deriving the Eq. 3.6, we have used the relations 3.2 and 3.3 and the fact that $\mathbf{C}_0^{m^{-1^T}} = \mathbf{C}_0^{m^{-1}}$, because $\mathbf{C}_0^m$ is nonsingular covariance matrix. Using Eqs. 3.4, the multimodel average covariance matrix of the forecast error, analogous to the Eq. 3.6, can be written as

$$\mathbf{\Sigma}_\tau = \mathbf{C}_0 - \mathbf{C}_\tau \mathbf{C}_0^{-1} \mathbf{C}_\tau^T. \tag{3.7}$$

There remains no predictability for asymptotically large lead time $\tau \to \infty$, therefore, initial and final state are independent. Hence, $\mathbf{C}_\infty \to 0$ for $\tau \to \infty$, and the multimodel average climatological error covariance matrix reduces to

$$\mathbf{\Sigma}_\infty = \mathbf{C}_0 \tag{3.8}$$

Substituting $\mathbf{\Sigma}_\infty$ and $\mathbf{\Sigma}_\tau$ into the generalized eigenvalue problem 2.14 leads to

$$\mathbf{G}\mathbf{q} = \lambda \mathbf{C}_0 \mathbf{q}, \quad \text{where} \tag{3.9}$$

$$\mathbf{G} = 2 \sum_{\tau=1}^{60} \mathbf{C}_\tau \mathbf{C}_0^{-1} \mathbf{C}_\tau^T \, \Delta_\tau. \tag{3.10}$$

Here the APT is summed over 60 months although the results are not sensitive to the upper limit of τ. The components that maximize the APT of a linear regression model are obtained by solving the generalized eigenvalue problem 3.9. The eigenvectors of the Eq. 3.9 are the coefficient vectors $\mathbf{q}$ and corresponding eigenvalues are the APT values. The APTs are arranged in decreasing order. The variates and loading vectors associated with each predictable component are obtained using the Eqs. 2.17 and 2.24.

By substituting Eqs. 3.7 and 3.8 in Eq. 2.13, the multimodel predictability measure R_τ^2 can be written as

$$R_\tau^2 = \frac{\mathbf{q}^T \mathbf{C}_\tau \mathbf{C}_0^{-1} \mathbf{C}_\tau^T \mathbf{q}}{\mathbf{q}^T \mathbf{C}_0 \mathbf{q}} \tag{3.11}$$

In linear regression theory, R_τ^2 is also called the coefficient of multiple determination.

Forecast skill in observations is measured in two ways. First, the normalized mean square error (NMSE) is defined as,

$$NMSE = \|\mathbf{q}^T(\mathbf{Y}_{t+\tau} - \mathbf{L}_\tau \mathbf{Y}_t)\|^2 / \|\mathbf{q}^T(\mathbf{Y}_t)\|^2, \tag{3.12}$$

where, $\|\cdot\|$ is the Euclidean distance. The other metric is the ρ_τ^2, where ρ_τ is the forecast

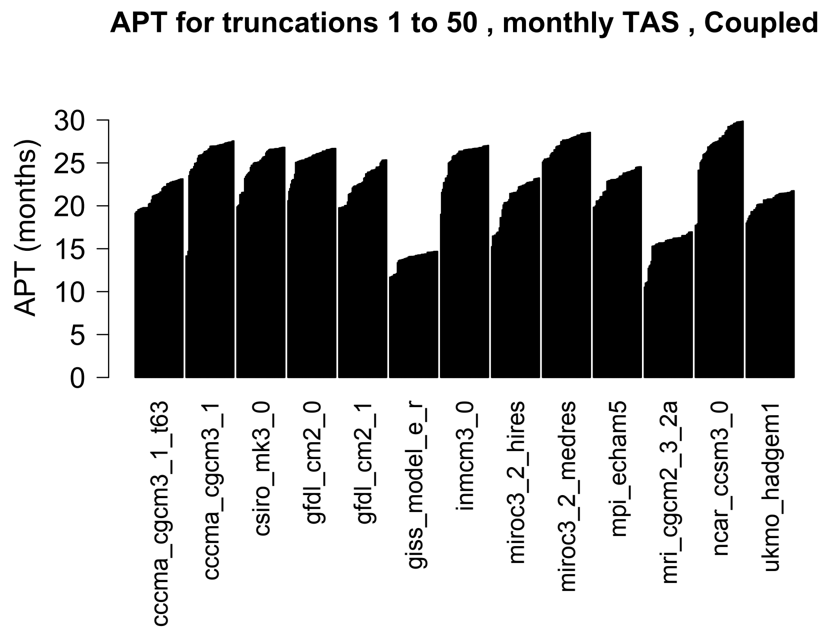

(a)

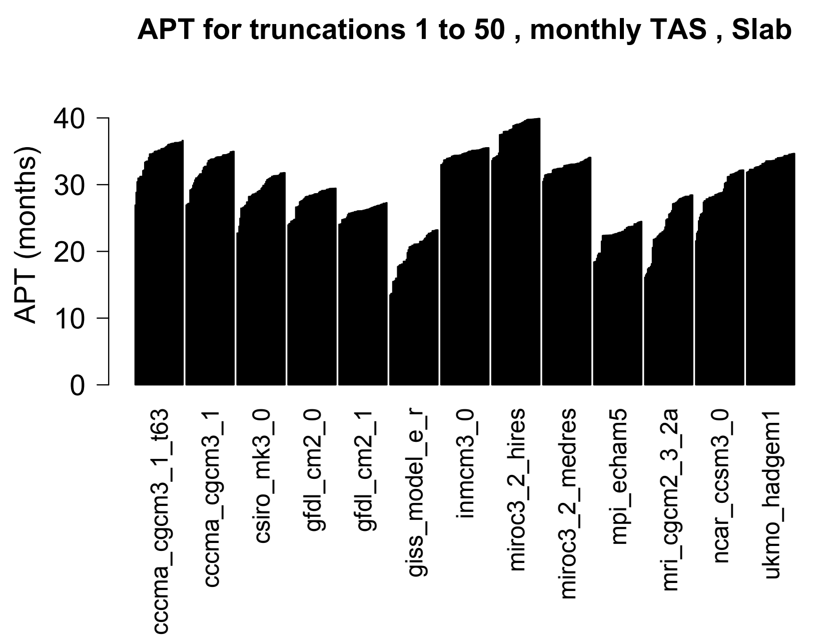

(b)

Figure 3.1: APT (months) computed for accumulated number of Laplacian eigenfunctions in (a) coupled and (b) slab models.

correlation skill measured as,

$$\rho_\tau = \mathrm{cor}\left[\mathbf{q}^T \mathbf{Y}_{t+\tau}, \mathbf{q}^T \mathbf{L}_\tau \mathbf{Y}_t\right]. \tag{3.13}$$

3.5 Significance level of predictability and forecast skill

Computing the significance level of predictability and skill of monthly data is a difficult task. One issue is that there exists serial correlation in monthly timeseries, and in order to compute the significance level, the issue of serial correlation should be taken into account. It is customary to divide the total sample size by some number representing the effective distance between independent samples. This procedure is not rigorous and sensitive to the method used to estimate the effective sample size. Moreover, the effective sample size depends on the degree of serial correlation and therefore depends on the time series being analyzed. For simplicity, we use a constant value of 6 months for the distance between independent samples. This value is chosen simply as a reference for comparison. The significance level (for non-serially correlated data) can be determined by standard procedures based on the F distribution. Since we have pooled all the model data together, the total sample size is very large in both the slab and coupled simulations. For illustration, the 95% significance level of R^2 for a total sample size of 1200 months (therefore effective sample size is $1200/6 = 200$ months) is 0.09. Since the total sample size is much larger than 1200 months in pooled slab and coupled models respectively, the significance level is much smaller for them. However, we can agree that predictability of 0.1 or smaller may be statistically significant but actually is too small to remain useful. Therefore, we chose $R^2 = 0.1$ as a reference point for both slab and coupled models so that predictability in them is measured against this reference point. Following similar arguments, we chose a value 0.1 for the NMSE skill and correlation skill to be reference point to measure significant skill.

3.6 Results

3.6.1 Selection of Laplacian truncation

A critical parameter in regularization is the selection of truncated Laplacians. If the number of Laplacians is too small, then the basis set may fail to capture important structures, but if the number is too large, then overfitting becomes a problem and APT is overestimated. Figs. 3.1a and 3.1b show APT in months computed for accumulated number of Laplacian eigenfunctions from 1 to 50 in the coupled and slab models, respectively. It is apparent that APT in all the models increases monotonically with the number of Laplacians. APT nearly saturates for truncations greater than 10 for most of the models except slab versions of GISS_Model_E_R and MRI-CGCM2_3_2A; and there is no appreciable increase in APT after that. Therefore, it seems reasonable to use ten Laplacians for computation of APT as it captures most of the APT in the models.

3.6.2 Predictability in the slab and coupled models

The multimodel APT of first ten predictable components are shown in the figure 3.2, top panel. It is interesting to note that APT of the most predictable component in the slab model is more than 20 months whereas in the coupled models is around 15 months. Also APTs of other components are comparable in both the simulations. The figure 3.2, bottom panel shows R_τ^2 at one year. It shows that except for the first component, predictability after one year is comparable in the slab and coupled models. Interestingly, for the first predictable component, predictability decays slower in the slab models than in the coupled models in the first year. This leads to twice as large predictability in the slab models as in the coupled models after one year.

3.6.3 Sensitivity of loading vectors

Recall that loading vectors are defined as projection of variates on the data (Eq. 2.24), or in other words, as regression of variates on the data in appropriate space. Now the loading

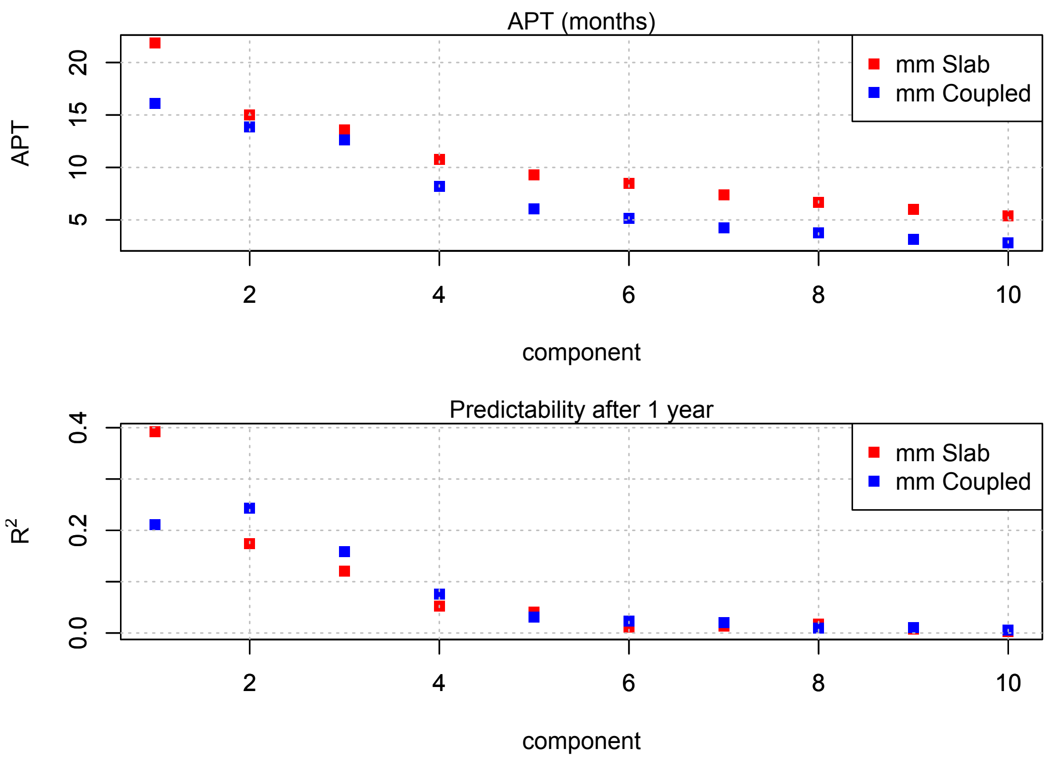

Figure 3.2: Multimodel APT (months) and R^2 of 10 predictable components in the slab and coupled simulations. R^2 shown is the explained variance after a year.

vectors obtained by projecting variates on the data matrix $\mathbf{X}_t$ are in the Laplacian space, i.e. in the truncated space (a function of truncation). We discovered a major limitation of loading vectors that they are sensitive to truncation, i.e., changing the truncation changes the loading vectors. Instead a regression map derived by projecting the variate on the "original data" is robust in the sense that it does not depend on the selection of truncation. To avoid any confusion, we call the projection of variate on the original data as "regression patterns". Fig. 3.3 illustrates these points. In this figure, the left panels show loading vectors (in the Laplacian space) for truncations 10, 20 and 35, whereas the right panel shows the regression patterns (in the data space) for the same truncations. It is clear from the figure that the regression pattern is largely insensitive to truncation whereas the loading

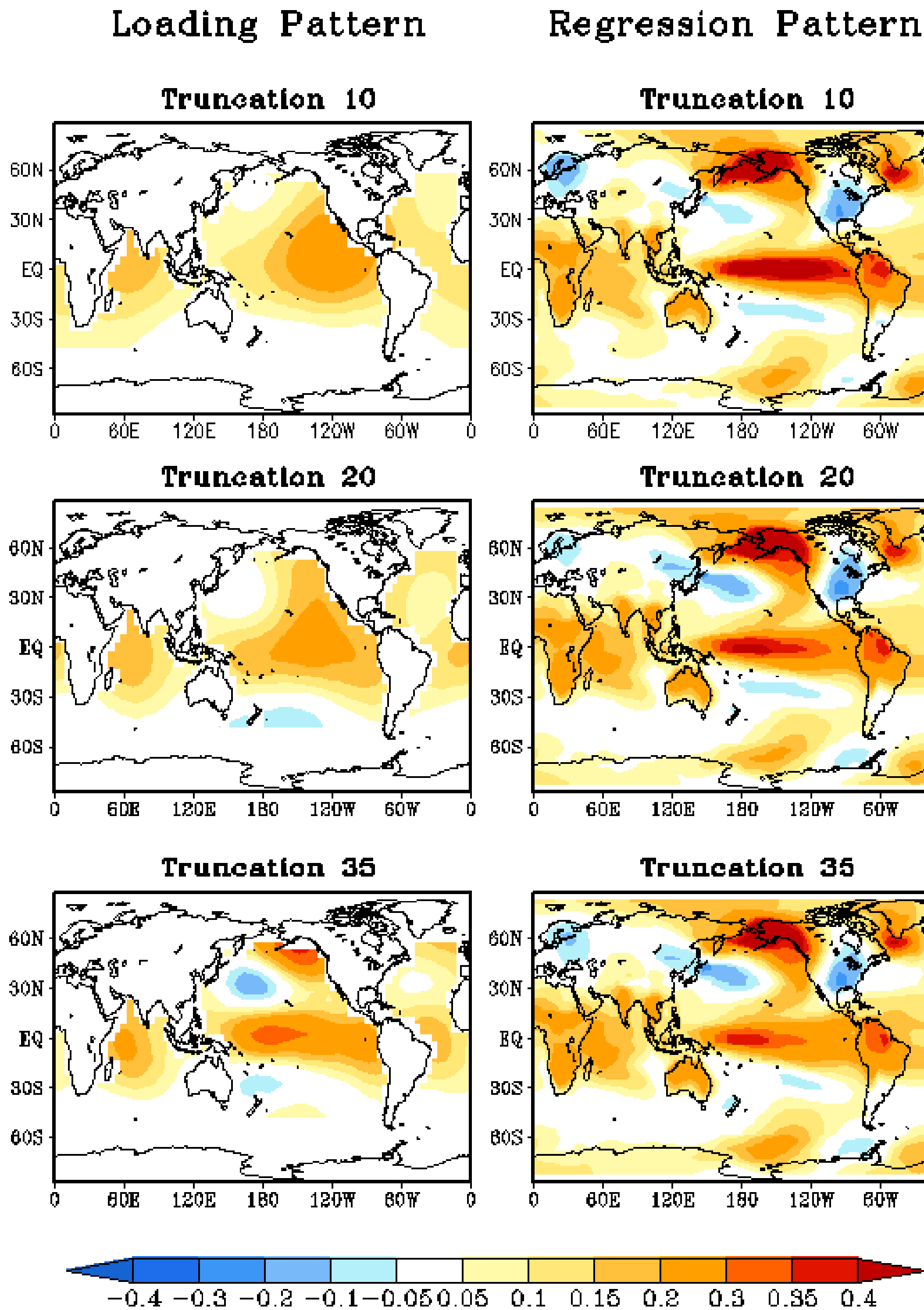

Figure 3.3: Sensitivity of loading patterns

vector is very sensitive and evolving towards the regression pattern with increasing number of truncations. This shows that regression patterns are robust in the sense that they do not depend upon truncation and hence are preferable over the loading vectors. Therefore we use regression patterns as predictable patterns in our study.

3.6.4 Most Predictable components in the slab and coupled models

The most predictable component in coupled and slab models is shown in fig. 3.4. Although some differences can be seen between the two regression patterns, especially in the northern latitudes, the large-scale structures are remarkably similar (panels (A) and (B)). An immediate question arises if the differences in spatial structures are important? One approach to quantifying the importance of these differences is to project the coefficient vectors $\mathbf{q}$ on the observed laplacian timeseries $\mathbf{Y}_t$ and compare the resulting projection coefficients. If the projection coefficients for the two patterns are close, then differences in spatial structure can be said to be minor, in the sense that they have a minor impact on their corresponding time series, which are the central quantities in predictability theory. The time series obtained by projecting these patterns on observations are shown in fig. 3.4(c). As can be seen, the two time series are very similar – their correlation is 0.92 – indicating that differences in spatial structure are relatively minor in terms of their corresponding time series (and thus their predictability). Thus, the differences in spatial structure seen in figs. 3.4a & b should not be interpreted too literally. The spatial patterns resemble the PDO, but the corresponding projected time series are modestly correlated with the observed PDO index (0.56 in slab and 0.35 in coupled models).

The predictability of the most predictable component is shown in fig. 3.4(d). It is clear that predicability, in perfect model sense, in slab model persists for around three years whereas it persists for less than two years in coupled models. The true predictability of real system is unknown, so we do not know which of these estimates is closer to the truth.

Next, we use the prediction operator $\mathbf{L}_\tau$ to predict the observed amplitude of the most predictable component $\mathbf{q}^T\mathbf{Y}_t$. Because observations were not used for model estimation,

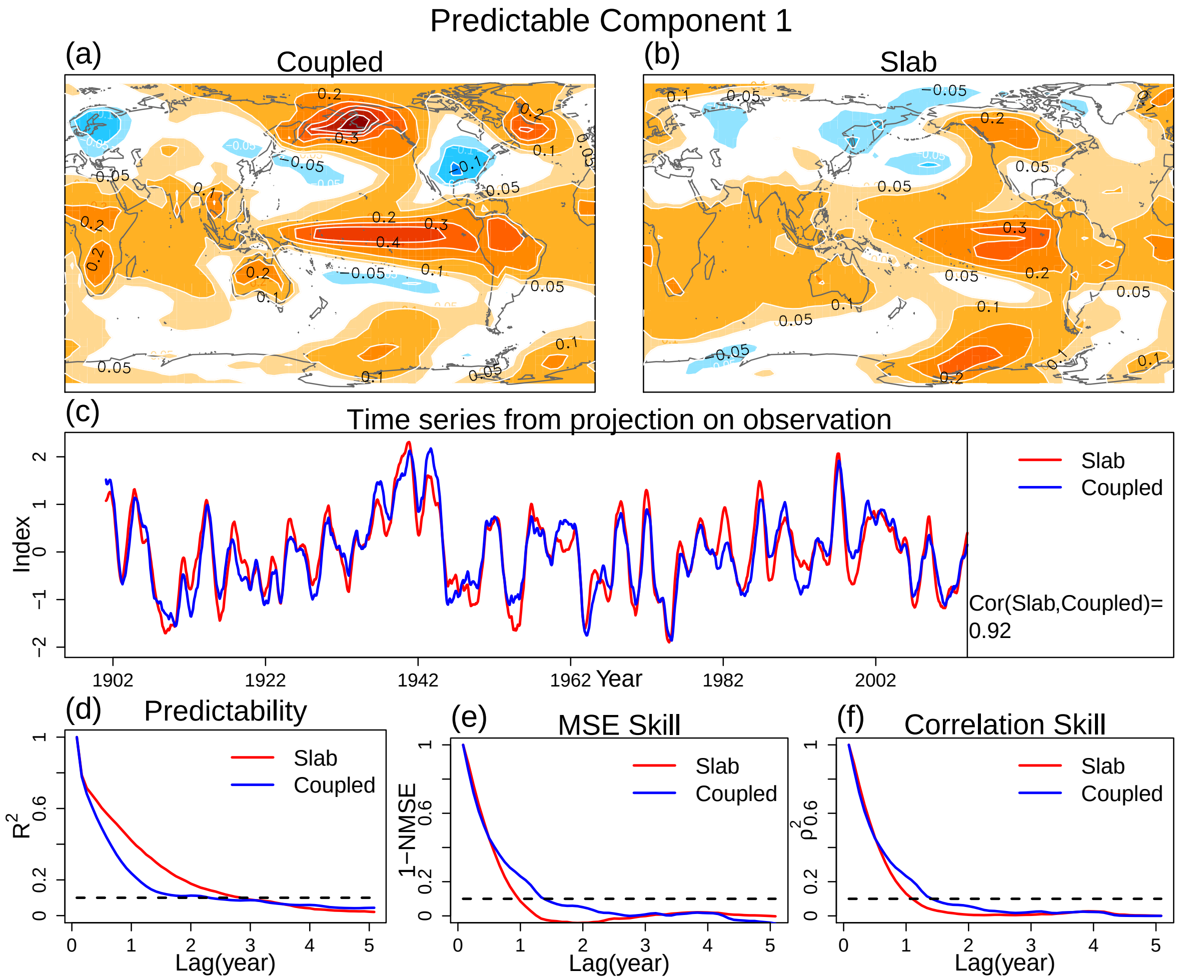

Figure 3.4: **Most predictable component in coupled and slab models.** Most predictable component is derived by maximizing the Average Predictability Time (APT) separately in coupled and slab models. (a & b): Regression pattern of the most predictable component in the coupled and slab models, respectively. Each pattern is normalized such that the time series multiplied by the pattern gives the temperature variations (in degrees Celsius) due to this component. (c): Projection of the most predictable pattern onto monthly observed SST, smoothed with a 1-year running mean (blue and red curves, respectively). The correlation between coupled and slab projected time series is indicated in the bottom right legend. (d): The predictability (3.11) of a linear prediction model that predicts the component in dynamical models. (e & f): The forecast skills (3.12) and (3.13) of a linear prediction model that predicts the component in observations. (d), (e) & (f): The dashed line at 0.1 indicates the reference level above which predictability and skill is assumed to be useful (a discussion about this is given in the section 3.5). The timescale of the predictability and forecast skills is defined by the time (lag) when the red and blue curves intersect the dashed curve.

observational data constitutes genuinely independent verification data for the prediction model. This approach avoids questions related to fitting and validating regression models with the same observational data. The NMSE skill and correlation skill are computed using the Eqs. 3.12 and 3.13. The skill based on NMSE (fig. 3.4e) is around a year in slab model and around 1.5 years in the coupled models. Similar conclusions are obtained using correlation skill (fig. 3.4f). The fact that the skill of the regression model derived from slab models is comparable to that from coupled models is striking considering that the slab model does not contain any interactive ocean dynamics, aside from simple thermodynamic mechanisms associated with heat storage.

Because the most predictable pattern can be predicted skillfully only a couple of years, one might question whether the term "decadal" is appropriate. In fact, many components with multidecadal time scales, such as the AMO and PDO (after the forced response has been removed), appear to be predictable for only a few years, despite having significant power on multidecadal time scales (Newman, 2007, 2013; Suckling and Smith, 2013; Zanna, 2012). The "time scale" of a variable is sometimes identified with the period at which the power spectrum peaks but this period should not be confused with the predictability time scale. The predictability time scale is in fact proportional to the damping timescale which is inversely related to the relative width of the spectral peak. Thus the larger is the damping timescale, the more predictable is the system and hence the narrower the spectral peak will be (Chang et al., 2004; DelSole, 2016; DelSole and Tippett, 2007).

The second most predictable component in coupled and slab models is shown in fig. 3.5. Both components have amplitudes concentrated in high latitudes and opposing signs across hemispheres (figs. 3.5a,b). Such predictable, inter-hemispheric asymmetric patterns often are claimed to be driven by the AMOC, but the fact that the slab model can produce this pattern demonstrates that inter-hemispheric asymmetric patterns can be generated without invoking the AMOC. Projection of these patterns onto observations yields similar time series, as indicated by the correlation value of 0.83 (fig. 3.5c). The projections are modestly correlated with the observed AMO index (~ 0.4 in coupled and slab models). The

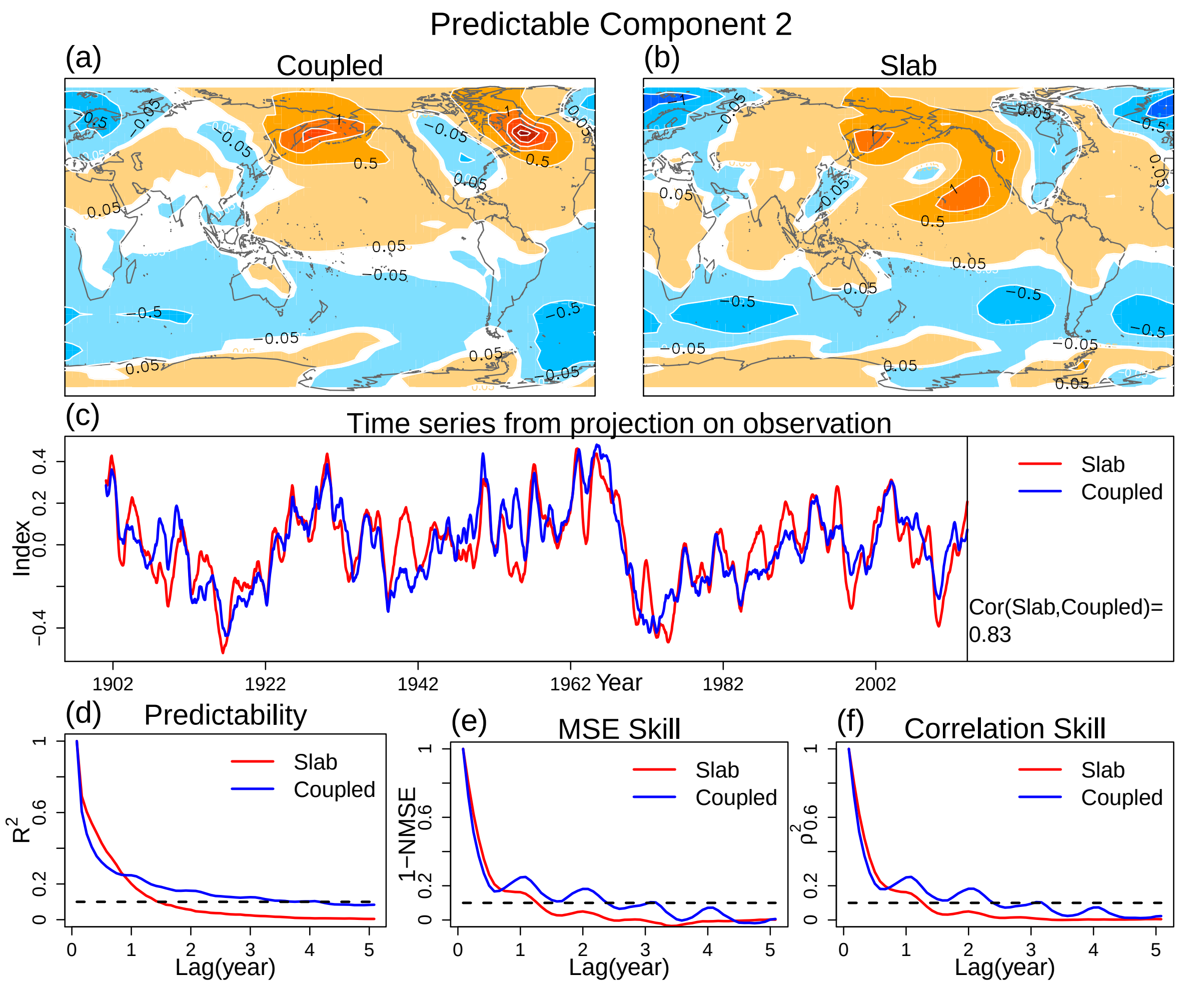

Figure 3.5: **The second predictable component in coupled and slab models.** Same as in figure 3.4, except for the second most predictable component.

predictability in coupled models is around three years whereas in slab model is less than two years. Also, the skill in coupled models is between 2 and 3 years whereas in slab models is between 1 and 2 years. Thus the coupled system has stronger predictability and forecast skill than its slab counterpart (i.e., the blue curves lie above the red in figs. 3.5d-f), suggesting that interactive ocean dynamics play a larger role than in the first component. Nevertheless, the slab models provide predictability and skill for around a year and half. Interestingly, the regression model utilizes only surface information so whatever ocean dynamics may be at play can be inferred from surface variables.

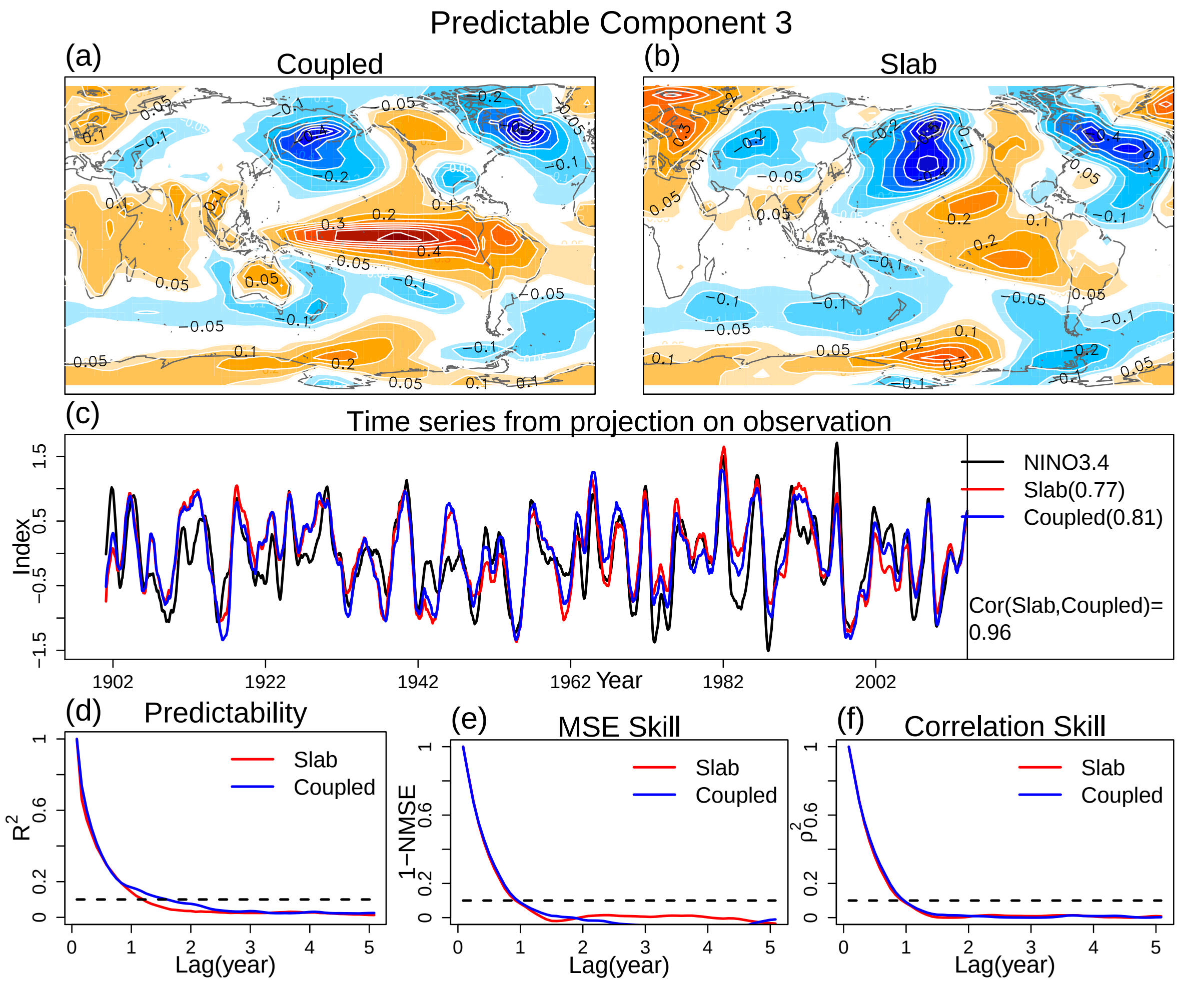

Figure 3.6: **The third predictable component in coupled and slab models.** Same as in figures 3.4 and 3.5, except for the third most predictable component. The black curve in panel (c) shows the observed 1-year-smoothed Nino 3.4 index. The correlation between each projected time series and the observed ENSO index is indicated in the parenthesis after "slab" and "coupled" in the right legend, and the correlation between coupled and slab projected time series is indicated in the bottom right legend.

The third most predictable component in coupled and slab models is shown in fig. 3.6. This component resembles the observed ENSO pattern. Incidentally, components 1 and 3 look similar, but their projection on observations differ and their predictabilities differ (indeed, their time series are orthogonal in the models). Though the pattern in the slab run does not have maximum loading along the equatorial Pacific, it's projection time series is very similar to that of the coupled model pattern (correlation of 0.96). Interestingly, the component in slab models is correlated with the observed 1-year smoothed ENSO index almost as well as the component in coupled models. Slab models provide as much predictability and forecast skill ($\sim$ a year) as coupled models, which is surprising because slab models do not contain the oceanic Rossby and Kelvin waves associated with ENSO mechanisms. Also, the prediction skill of ENSO in current dynamical and statistical models is less than a year (Collins et al., 2002; Li and Ding, 2013; Zheng et al., 2006). Subsequent predictable components (i.e., 4, 5 and 6) in slab and coupled models show similar spatial structure, predictability, and skill, but these are not shown for brevity.

We emphasize that the two curves shown in panels (d), (e) and (f) of figs.1-3 show the skill and predictability of two different patterns. Testing statistical significance of a difference in skill or predictability of two different quantities is not straightforward. Nevertheless, physically, the range of skill and predictability of the two components are "comparable." It is also important to recognize that even if the predictable components were not similar component-by-component, this would not necessarily imply that the predictabilities differ. For instance, the patterns could be identical but have different rankings. Alternatively, the leading pattern of one model could be a linear combination of leading patterns of another model, or the patterns of one model could be rotated in the same space as those of the other model. In any of these cases, a component-by-component comparison would be unsatisfactory and a more comprehensive comparison would be required.

The above comment is pertinent to relating our results to traditional indices like the AMO or PDO. As mentioned earlier, these latter indices have modest correlations with individual model components, but this fact does not imply the two sets of components are

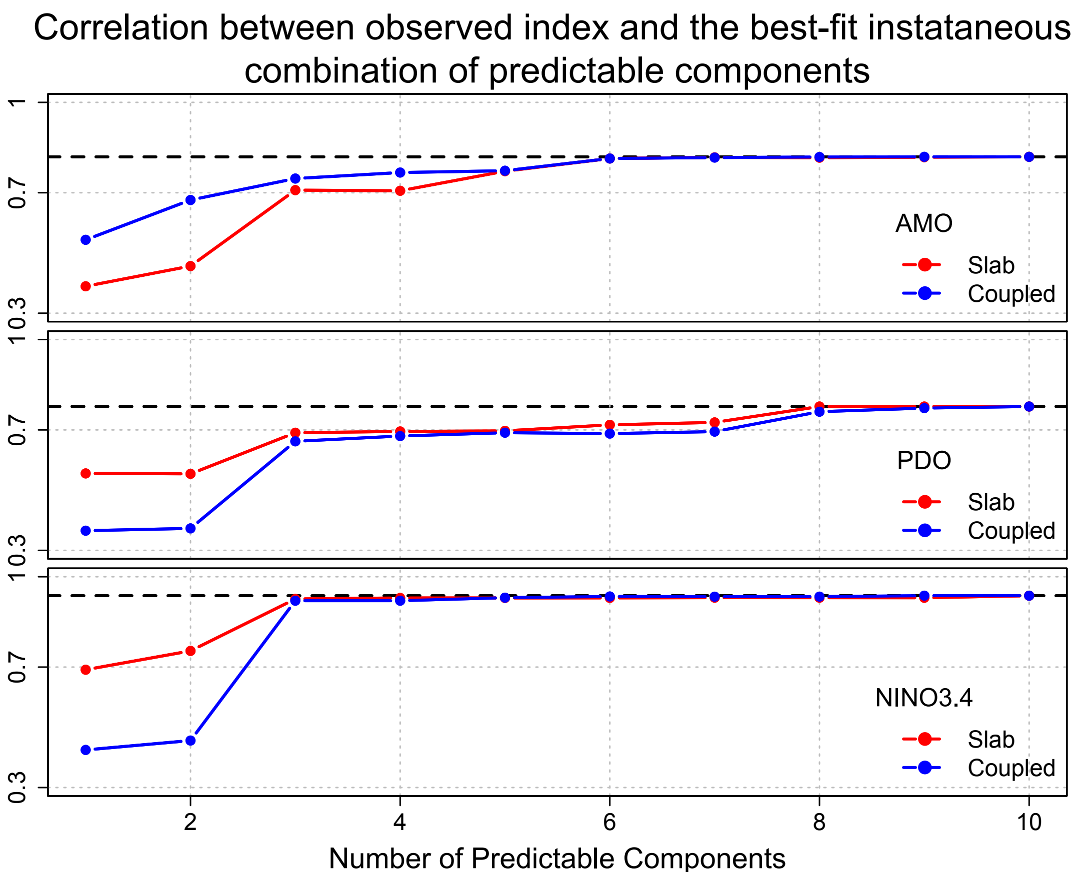

Figure 3.7: **Correlation between observed index and the best-fit instantaneous combination of predictable components.** The correlation is computed using a 12-month running mean for the observed index and for the best fit instantaneous combination of predictable components. The horizontal axis shows the number of predictable components used to fit the observed index. The blue and red curves show results for coupled and slab predictable components, respectively. The black dashed line shows the maximum correlation when all ten predictable components are used.

unrelated. For instance, the traditional indices could be some linear combination of the components derived here. To investigate this question, the observed AMO index was fit to a linear combination of predictable components. The correlation between the observed and best fit AMO index is shown in the top panel of fig. 3.7, where the correlation is computed from a 12-month running mean of the two time series. The correlation based on all ten predictable components is 0.82, indicating that much of the AMO variability can be captured by a linear combination of predictable components. The figure shows that only six predictable components are needed to achieve this correlation. For the PDO (bottom panel of fig. 3.7), the maximum correlation is 0.78, again indicating that much of the PDO variability is captured by the most predictable components. Noticeably, the maximum correlation for the ENSO (Nino3.4) index is 0.94 and only first three components are sufficient to capture this correlation. It is important to note that in contrast to the Nino3.4 index, the traditional AMO and PDO indices are not captured by just the first two or three components, suggesting that the AMO and PDO indices may not be the best indices of decadal predictability as the leading predictable components. This conclusion is not necessarily surprising since traditional indices were not designed to maximize predictability; for instance, the AMO is merely a spatial average over the Atlantic while the PDO is merely a leading EOF, which maximizes variance, not predictability. In contrast, ENSO seems to be better identified with the most predictable components hence is an appropriate target for predictability.

3.7 Global basis vectors versus Local basis vectors

An interesting question in our analysis design is whether the basis vectors for maximizing predictability should be global or restricted to individual ocean basins. If decadal predictability in the Atlantic and Pacific arise from different mechanisms, then global basis vectors may lead to failure to detect localized predictability, or may give a misleading impression of the spatial extent of predictability. To investigate this issue, APT analysis was applied to the union of five Laplacian eigenfunctions from the Pacific plus five Laplacian

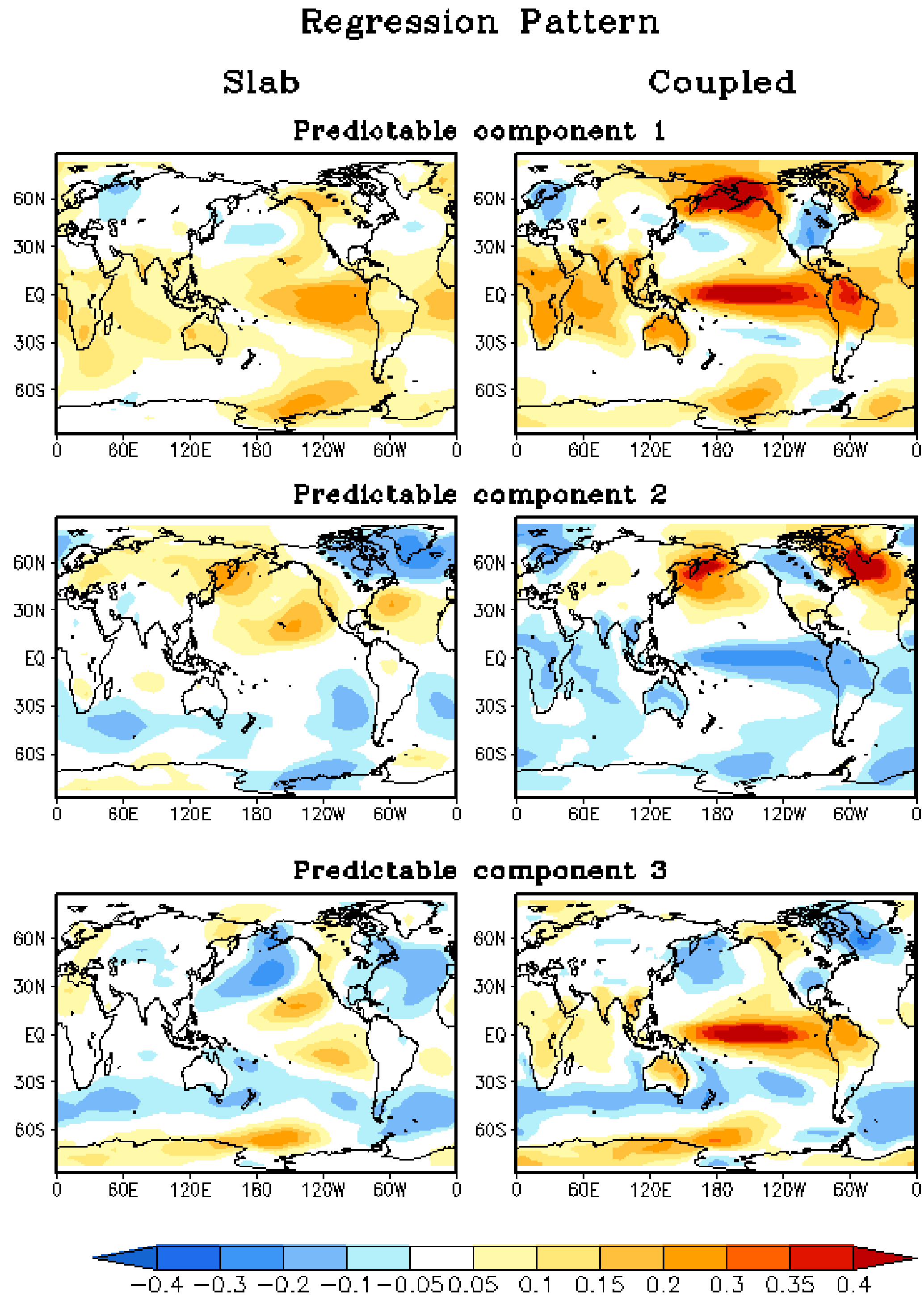

Figure 3.8: Regression patterns of the first three most predictable components: The patterns are obtained when APT analysis was applied to the union of five Laplacian eigenfunctions from the Pacific plus five Laplacian eigenfunctions from the Atlantic.

eigenfunctions from the Atlantic. If predictability were localized in each basin separately, then APT analysis would indicate that fact by producing predictable components with loadings in just the Atlantic or just the Pacific. The fig. 3.8 shows the regression patterns for the first three predictable components obtained by using the union of five Laplacian eigenfunctions from the Pacific plus five Laplacian eigenfunctions from the Atlantic. It is clear that, in both the slab and coupled models, APT analysis always yields global patterns, suggesting that the most predictable components in climate models have global expressions. This result does not necessarily imply that the mechanisms are global. For instance, the mechanism could be local while the response may be global. Indeed, ENSO arises from coupled dynamics localized in the equatorial Pacific, yet it has a global expression through Rossby wave teleconnection mechanisms. Similarly, climate models show that when one basin is forced on multidecadal time scales, the other oceans (which are free to adjust) vary in synchrony (Zhang et al., 2007). If a predictable component has a global expression, then it is beneficial from a statistical point of view to use global basis vectors in order to improve the signal-to-noise ratio, even if the mechanisms giving rise to that predictability are local. Moreover, the mechanisms that dominate decadal predictability could very well be global (Kucharski et al., 2016). In any case, analyzing global basis vectors is not incompatible with the hypothesis of local mechanisms of predictability. For the above reasons, we chose global basis vectors to maximize predictability.

3.8 Some caveats

It is possible that our results are biased by the procedure used to estimate predictability and skill. For instance, we have used a linear regression model to measure APT, so predictability arising from nonlinear dynamics may not be captured by our method. Also, our linear regression model is based on ten Laplacian eigenfunctions, so any predictability in the smaller-scale eigenfunctions will not be captured by our method. Admittedly, removing a third order polynomial from the observed SST data may not perfectly remove the forced signal. Any leftover forced signal may contaminate our results, but the fact that the predictable components have real forecast skill of the order of years lends legitimacy to our conclusions.

Also, climate models suffer from significant biases that may reduce or distort the influence of ocean dynamical processes. For example, many coupled models tend to be too cold and fresh in the North Atlantic, which may impact the forcing of the Atlantic Meridional Overturning Circulation (AMOC) by the North Atlantic Oscillation (NAO), and impact the coupling of the AMOC with the surface ocean. Reducing these biases has been found to change the character of decadal variability in coupled models (Park et al., 2016). Also, the above biases can alter the AMOC from being thermally driven to being salinity driven, which also likely impacts predictability (Menary et al., 2015). Despite these shortcomings, this paper shows that empirical models derived from dynamical models can skillfully predict observations for a few years, suggesting that coupled and slab models still capture realistic aspects of decadal predictability, despite certain biases and inconsistencies with observations.

3.9 Summary

In this chapter we attempted to identify the dominant patterns of decadal predictability in systems without ocean dynamics. Also we investigated if these patterns are similar to those of systems that capture ocean dynamics. In order to address these issues we analyzed coupled (systems with interactive ocean dynamics) and slab (systems without interactive ocean dynamics) in the CMIP3. We found that the most predictable patterns are characterized by large global patterns in both the slab and coupled models and that the spatial structure in the slab and coupled models are remarkably similar. We also investigated if the patterns derived from systems with and without interactive ocean dynamics have similar time scales? How would multiyear predictions by the two systems compare in terms of skill? We found that predictability timescales and forecast skills derived from coupled and slab models are comparable, though predictability and skill of the coupled models are slightly higher than that of the slab models in some of the components identified.

The similarity of predictable patterns, predictability timescales and forecast skills derived from coupled and slab models strongly suggest that interactive ocean dynamics is not essential for the existence of multi-year predictability previously identified in coupled models and observations. Instead, the essential mechanisms of decadal predictability appear to involve atmospheric processes and thermodynamic air-sea coupling. One often cited mechanism is the fact that the ocean mixed layer acts as an integrator of short-period stochastic forcing from the atmosphere, producing red power spectra from white noise forcing (Hasselmann, 1976). Other mechanisms such as cloud-SST feedback (Bellomo et al., 2014) and wind-evaporation-SST feedback (Park et al., 2005) may further redden the spectrum. We emphasize that we do not claim that ocean dynamics play *no* role in decadal predictability. For instance, the skill derived from coupled models tends to be higher than that from slab models (see figs. 3.4e,f and 3.5e,f), though the difference is small in many cases. In the other cases, interactive ocean dynamics appear to simply enhance or modulate decadal predictability without significantly altering the spatial structure. Indeed, components like the AMO and PDO are highly persistent and can be predicted with skill by univariate regression models, but can be predicted with somewhat more skill if predictors associated with ocean dynamics (e.g., ocean meridional circulation or ENSO) are included as predictors (Newman et al., 2003; Trenary and DelSole, 2016). There is no doubt that ocean dynamics can produce variability over a huge range of time scales, from days to millennia, but the degree to which subsurface variability on decadal and multidecadal time scales influences the atmosphere and continental land masses (where humans live) remains to be quantified.

Chapter 4: APT of coupled and slab models: model-by-model

4.1 Motivation

In the previous chapter we examined predictability and forecast skills arising in the slab and coupled systems in a multi-model sense. In this chapter, we examine differences in predictability and forecast skills in coupled and slab models on a model-by-model basis. This chapter presents model-by-model comparison in two different senses. The first sense refers to a comparison of the slab (atmosphere coupled to 50-m deep slab ocean mixed layer) and coupled (atmosphere coupled to full ocean) versions of a model. By comparing the slab and coupled versions of the same model, we can test the sensitivity of predictability to including interactive ocean circulation. The second sense refers to a comparison across slab models or a comparison across coupled models. For example, since two slab models differ in their atmospheric component, by comparing two slab models, we can test the sensitivity of predictability to atmospheric dynamics. The interpretation of differences across coupled models is rather complicated as the differences may occur due to differences in the atmosphere, differences in the ocean circulation, or differences due to dynamics arising from coupled ocean-atmosphere interactions.

In this chapter, we investigate the degree of model agreement in estimates of predictability and skill. Equivalently, we investigate whether some models are outliers, in the sense that their predictability and skill differs a lot from the multimodel mean. We also determine whether some models have especially high skill or especially low skill. In addition, we will examine whether some of the conclusions found in the multi-model analysis, such as the fact that the slab and coupled models have comparable skill, also hold on a model-by-model basis.

4.2 Method

4.2.1 Optimized APT in Each Model

We begin with the linear regression model used in chapter 3. This model predicts the future amplitude of ten Laplacian eigenfunctions based on their present value using (3.2), where the prediction operator $\mathbf{L}_\tau^m$ is given by (3.3). The corresponding forecast error covariance matrix $\mathbf{\Sigma}_\tau^m$ is given by (3.6). In this chapter, we optimize APT in each individual model. To do this, we substitute $\mathbf{\Sigma}_\infty^m$ and $\mathbf{\Sigma}_\tau^m$ into the generalized eigenvalue problem (2.14), which gives

$$\mathbf{G}^m \mathbf{q}^m = \lambda \mathbf{C}_0^m \mathbf{q}^m, \quad \text{where} \tag{4.1}$$

$$\mathbf{G}^m = 2 \sum_{\tau=1}^{60} \mathbf{C}_\tau^m \mathbf{C}_0^{m^{-1}} \mathbf{C}_\tau^{m^T} \Delta_\tau \tag{4.2}$$

Solving this equation gives the components that maximize APT in model m. All other computation details (e.g., computing the variates and regression maps) are exactly the same as before, except using single-model covariance rather than multi-model covariances.

The predictability at fixed lead time τ in each model can be quantified by

$$(R_\tau^m)^2 = \frac{\mathbf{q}^{m^T} \mathbf{L}_\tau^m \mathbf{C}_0^m \mathbf{L}_\tau^{m^T} \mathbf{q}^m}{\mathbf{q}^{m^T} \mathbf{C}_0^m \mathbf{q}^m}. \tag{4.3}$$

4.2.2 Predictability in individual models

Unfortunately, presenting the results of the above calculations is challenging because each model produces its own set of predictable patterns. In fact, each model is characterized by 10 different patterns, so a comparison across 13 models would involve comparing 130 different patterns. However, there is an elegant way of comparing predictability across models. Specifically, we compare the predictability of the multi-model pattern and the single-model pattern in model m, where predictability is measured using the single-model regression operator $\mathbf{L}_\tau^m$. The idea here is that if the multi-model pattern is close to the single-model pattern, then the APTs of those patterns also should be close. To do this comparison, consider the multi-model coefficient vector $\mathbf{q}$. The R-square associated with this pattern is

$$R_\tau^{p^2} = \frac{\mathbf{q}^T \mathbf{L}_\tau^m \mathbf{C}_0^m \mathbf{L}_\tau^{mT} \mathbf{q}}{\mathbf{q}^T \mathbf{C}_0^m \mathbf{q}}. \tag{4.4}$$

Note that there is no superscript m on $\mathbf{q}$, but there are superscripts on all the other quantities. In essence, we are using the single-model regression model $\mathbf{L}_\tau^m$ to predict 10 Laplacian eigenvectors, then projecting the prediction onto the multi-model pattern. The corresponding APT can be written as:

$$APT^p = 2 \sum_{\tau=1}^{60} R_\tau^{p^2}. \tag{4.5}$$

Importantly, the APT values given by (4.5) are not optimized in the individual models. Therefore the APT of the multi-model pattern will always be less than the APT from optimizing (4.1) in a single-model sense. Moreover, APTs derived from Eq. 4.5 may not have the same order for multi-model and single-model patterns. The predictable variates for each model is obtained by projecting the multimodel $\mathbf{q}$ on the Laplacian timeseries (columns of the data matrix $\mathbf{x}$).

4.2.3 Forecast skills in individual models

For completeness, we give here mathematical details of how forecast skill is computed for single models. These equations differ from those in chapter 3 by including superscript m for the regression operator and dropping superscript m on the coefficient vector $\mathbf{q}$.

A linear regression model that predicts the future amplitude of ten Laplacian eigenfunctions of the observed SST based on their present values in each model is defined as

$$\hat{\mathbf{Y}}^m_{t+\tau} = \mathbf{L}^m_\tau \mathbf{Y}_t, \tag{4.6}$$

It is important to note that the prediction operator $\mathbf{L}^m_\tau$ is computed from the dynamical models as in Eq. 3.3. The projection of multimodel coefficient vector $\mathbf{q}$ on the observed Laplacian timeseries can be computed as $\mathbf{q}^T\mathbf{Y}_t$. Similarly, the projection of multimodel coefficient vector $\mathbf{q}$ on the predicted Laplacian timeseries in the observation is $\mathbf{q}^T\hat{\mathbf{Y}}^m_{t+\tau}$. Now the forecast skill in terms of the correlation skill ρ^2_m is defined as

$$\rho_m = \mathrm{cor}\left[\mathbf{q}^T\mathbf{Y}_{t+\tau}, \mathbf{q}^T\hat{\mathbf{Y}}^m_{t+\tau}\right]. \tag{4.7}$$

It is important to note that ρ_m a is model specific because $\hat{\mathbf{Y}}^m$ is model specific.

4.3 Significance level of predictability and forecast skill

As discussed in section 3.5, computing the significance level of predictability and skill of monthly data is a difficult task. One issue is that there exists serial correlation in monthly timeseries, and in order to compute the significance level, the issue of serial correlation should be taken into account. It is customary to divide the total sample size by some number representing the effective distance between independent samples. This procedure is not rigorous and sensitive to the method used to estimate the effective sample size. Moreover, the effective sample size depends on the degree of serial correlation and therefore depends on the time series being analyzed. For simplicity, we use a constant value of 6 months for the distance between independent samples. This value is chosen simply as a reference for comparison. The significance level (for non-serially correlated data) can be determined by standard procedures based on the F distribution. Keeping these caveats in mind, the 95% significance level of R^2 can be computed as

$$R^2_{0.95} = F_{0.95} \frac{p-1}{\frac{N}{6}-1}, \tag{4.8}$$

where $F_{0.95}$ is the critical value of F statistic at 95% level. p is the number of predictors (10 here) and N is the sample size (number of months) in the individual models.

The above refers to predictability in the perfect model sense. We also need to quantify skill in observations. The 95% significance level of correlation skill $\rho^2_{0.95}$ is 0.017 based upon the total sample size of 1380 months (effective sample size of $1380/6 = 230$ months) in the observation. This value of correlation skill may be significant but is not useful in practice. Hence we use a value of 0.1 as a reference point for the significant and useful correlation skill.

4.4 Results

4.4.1 Comparison Between Multi-model and Single-model Predictability

A major question is whether the multi-model predictable components adequately capture the predictability of single models. For instance, one model might have a lot of predictability that differs from that of other models. In this case, a multi-model pattern may not project on a predictable single-model pattern. Are we sure we are not missing some predictability by focusing on multi-model patterns? To investigate this question, we compare the APT of the multi-model and single-model optimized patterns. In general, predictable patterns are derived from different data (multi-model, single model, coupled, slab), but are eventually projected onto single-model time series for estimating its predictability in that model.

We first consider patterns computed from slab models. The maximized APT in individual slab models are shown in fig. 4.1 as yellow solid squares. For the most part, the maximized APTs (a measure of overall predictability/predictability timescale of a system)

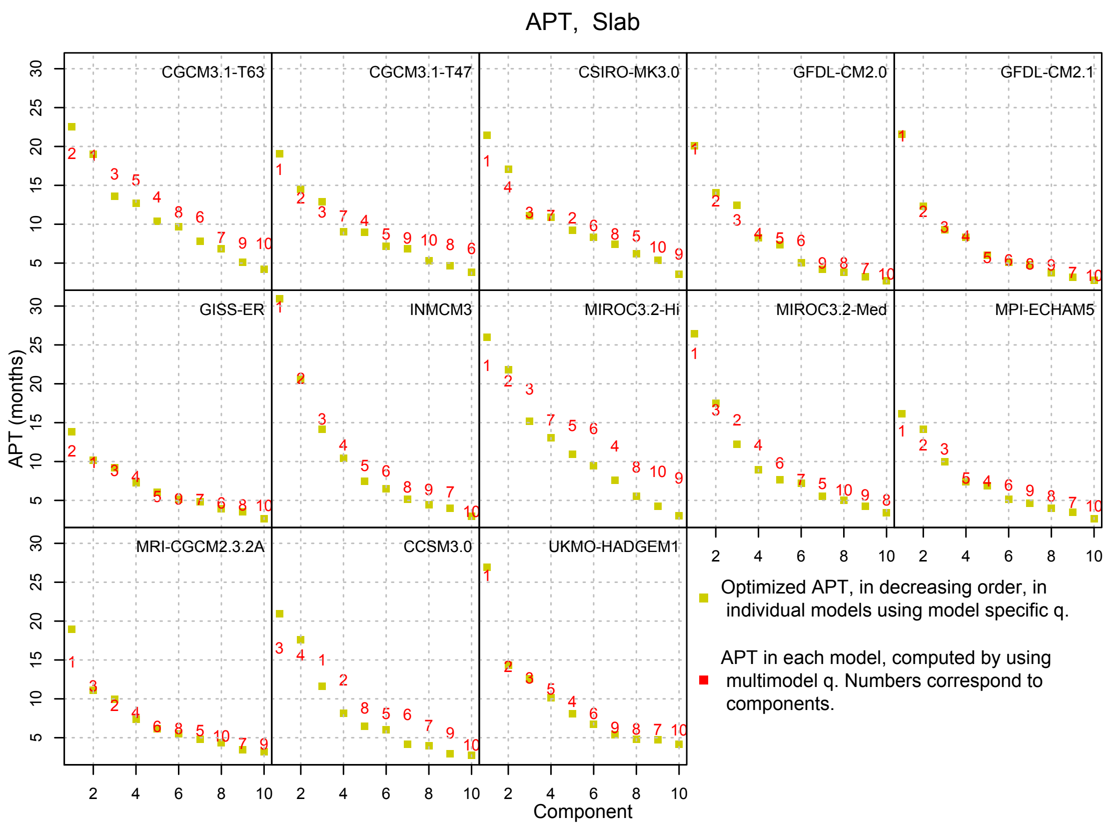

Figure 4.1: APT of predictions from a linear regression model. The regression model is based on $\mathbf{L}_\tau^m$, which is estimated from each model slab run. The resulting predictions are projected onto the most predictable pattern of each respective slab model (yellow squares), and onto the pattern that optimizes multi-model APT over all slab runs (red numbers). In the latter case, the number labels give the ranking in the multi-model ensemble, but the values have been re-ordered (from largest to smallest) for each model separately to simplify comparison to the single-model optimized values.

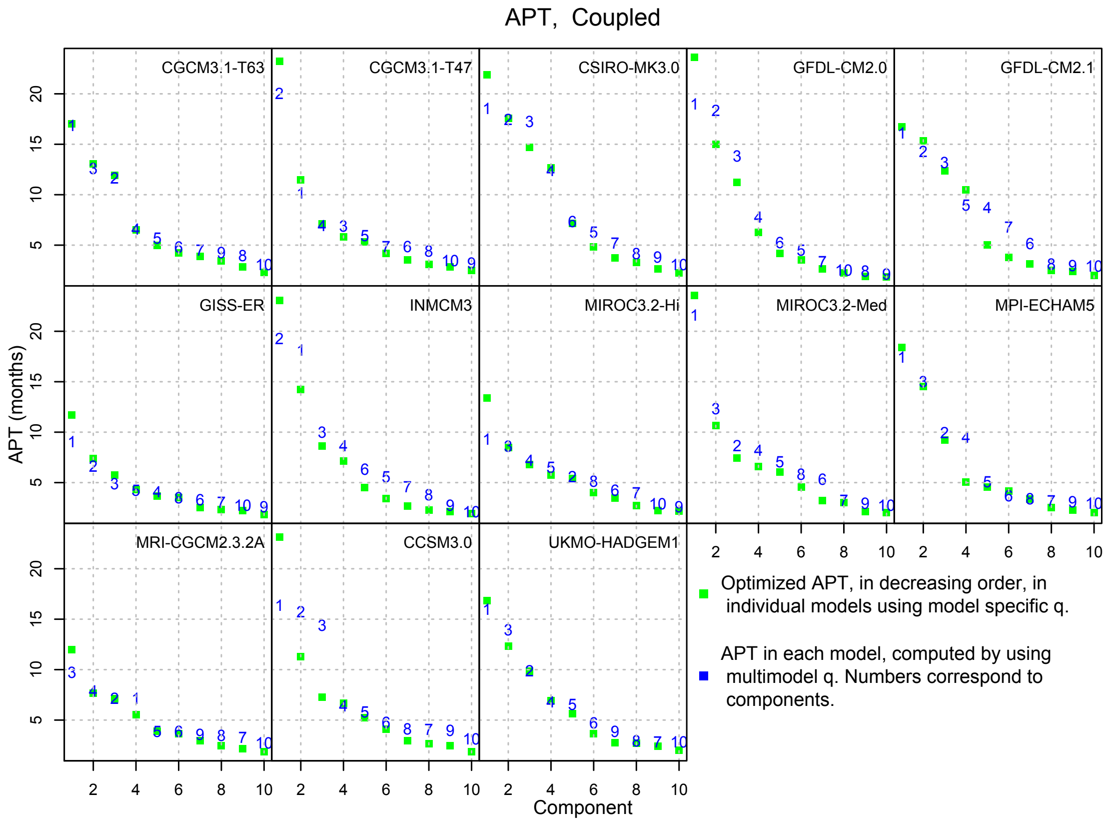

Figure 4.2: Same as fig. 4.1, but for coupled model runs.

are similar across most of the slab models (compare yellow squares across models). However, there are important differences across models. For instance, the leading APT ranges between 15-30 months across models, which is a factor of two. Thus, a large range of predictability can arise simply from differences in atmospheric dynamics (because the slab ocean is the same in these models).

The APT of the multi-model pattern projected on individual models is shown in fig. 4.1 as the red numbers. The number indicates the rank in the multi-model ensemble, but the APT values have been re-ordered with respect to each model so that they can be compared to the single-model optimized predictable components. As can be seen, the red numbers are close to the yellow squares, indicating that the multi-model patterns are similar to the single-model optimized patterns (except possibly in a different order). Thus, the multimodel pattern does not "miss" important predictability in individual slab models. Strikingly, the same conclusion holds for the coupled models, as can be seen in fig. 4.2, which shows the analogous results for coupled models.

Together figs. 4.1 and 4.2 convey two important points. First, most of the slab models have similar APT values despite of the differences in the atmospheric-slab ocean dynamics. However, a small number of models differ a lot from other models, indicating sensitivity to atmospheric dynamics. Also, coupled models tend to have largely similar APT values despite of differences in the atmosphere-ocean dynamics, although there are some exceptions. Second, the multimodel pattern can be reasonably used to measure predictability in individual models without loss of any appreciable predictable signal.

4.4.2 APT in individual models

Hereafter we consider only the multi-model patterns, since the previous section showed that there is no loss in generality in doing this. Nevertheless, there are two types of multi-model patterns: slab and coupled. In addition, for each dynamical model, there exist two types of oceans: slab and coupled. Thus, there are a total of four possible APTs that can be computed per model. These cases are denoted s2s, s2c, c2s, c2c. To explain this notation, consider the case s2c: the first letter ("s") indicates that slab multi-model $\mathbf{q}$ is used for projection, and the second letter ("c") indicates that the prediction operator $\mathbf{L}_\tau^m$ is derived from the coupled model. Thus, s2c means that the *s*lab pattern is projected onto the *c*oupled-model regression predictions. A similar interpretation follows for other cases s2s, c2c and c2s.

The APTs of the first predictable component in individual models for the various cases are shown in fig. 4.3. First note that, in general, the APT values for s2s and c2s (red squares and yellow stars) are close to each other, and those for s2c and c2c (green circle and blue diamond) are close to each other. This similarity in APT values reinforces the conclusion in chapter 3 that the predictable patterns are very similar between coupled and

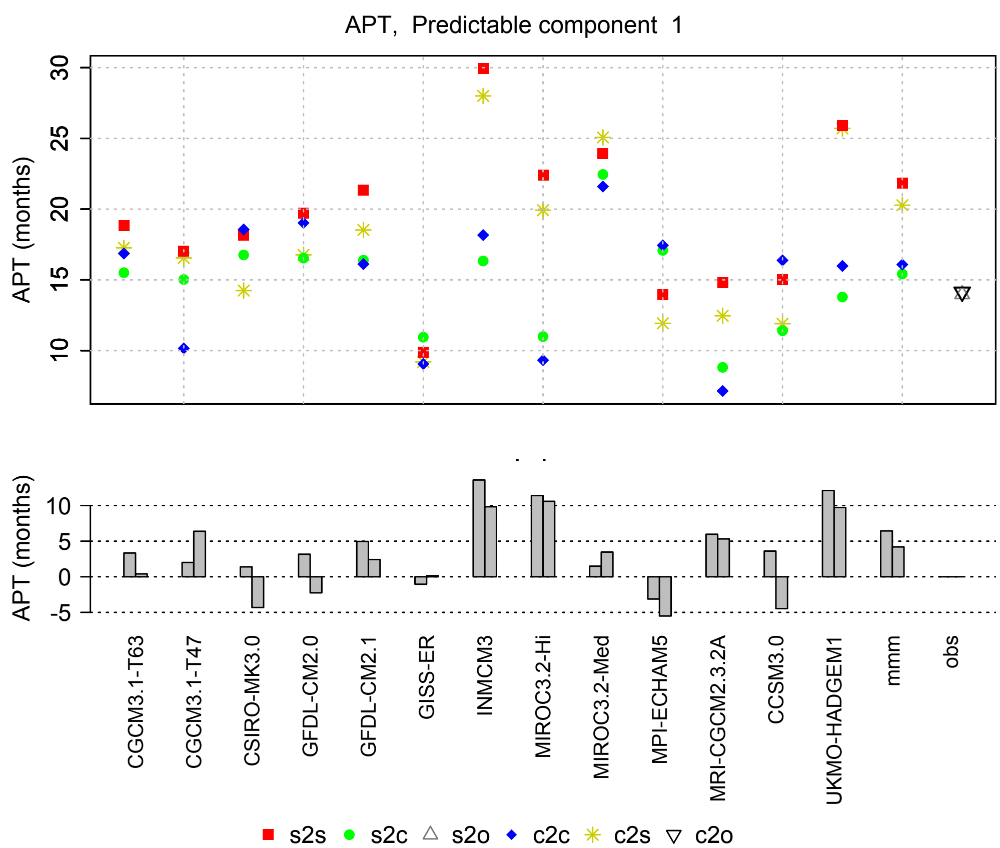

Figure 4.3: Upper panel: APT of the first predictable component, where the component is derived from either the coupled or slab in a multi-model sense, and then projected onto either the coupled or slab model in a single-model sense (i.e., four distinct cases). The various cases are denoted s2s, s2c, c2s, c2c, where the first letter refers to the model-type from which the pattern is derived, and the second letter refers to the model-type on which the pattern is projected. For instance, s2c means that the most predictable pattern from the slab model is projected onto a coupled model simulation. Lower panel: differences in APT, where the first vertical bar indicates the difference between s2s and s2c, and the second vertical bar indicates the difference between c2s and c2c.

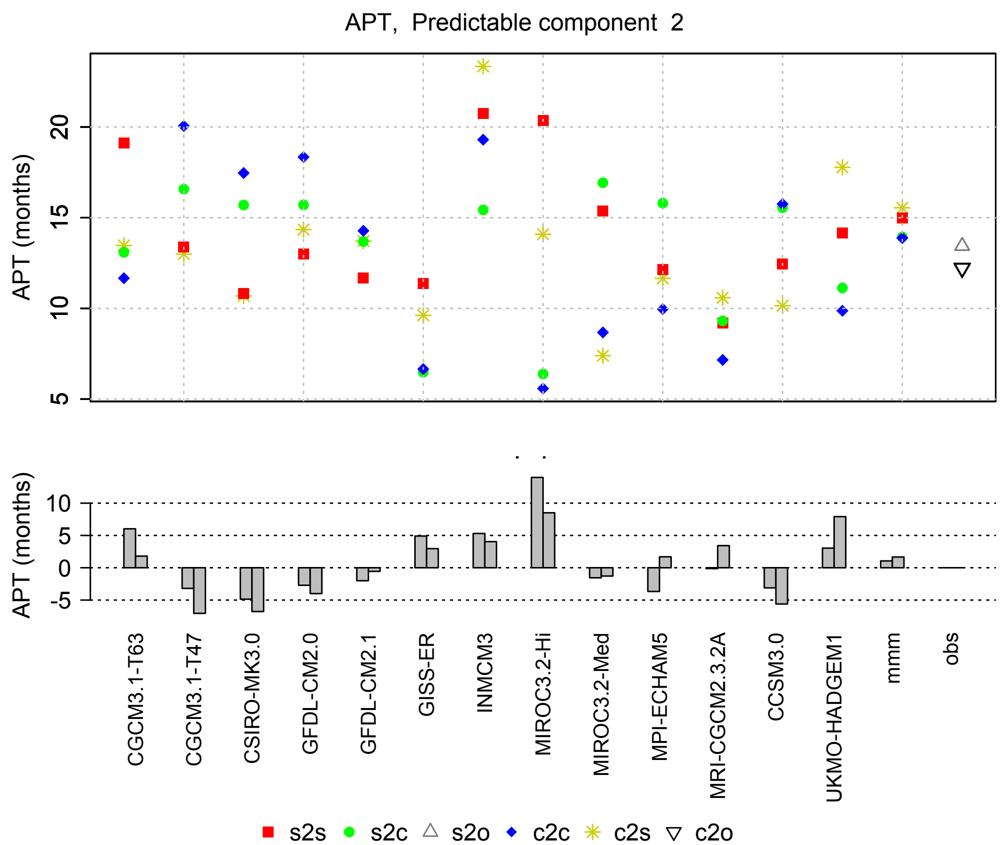

Figure 4.4: Same as figure 4.3, but for the second predictable component.

slab models. A minor exception to this general pattern is CGCM3.1-T47 and CCSM3.0, whose values for s2c and c2c differ by about 5 months, indicating a sensitivity to whether pattern is optimized in the coupled or slab model. Moreover, the direction of the difference is not robust.

Second, aside from a few exceptions, all four APT values are close together. The main exceptions are INMCM3, MIROC3.2-Hi, HadGEM1, which have a much larger APT for s2s/c2s than for s2c/c2c. This difference implies that, for these models, the predictability in the slab model is much larger than the predictability in the coupled model. This result is counter to the expectation that "coupled ocean enhances predictability." We visually

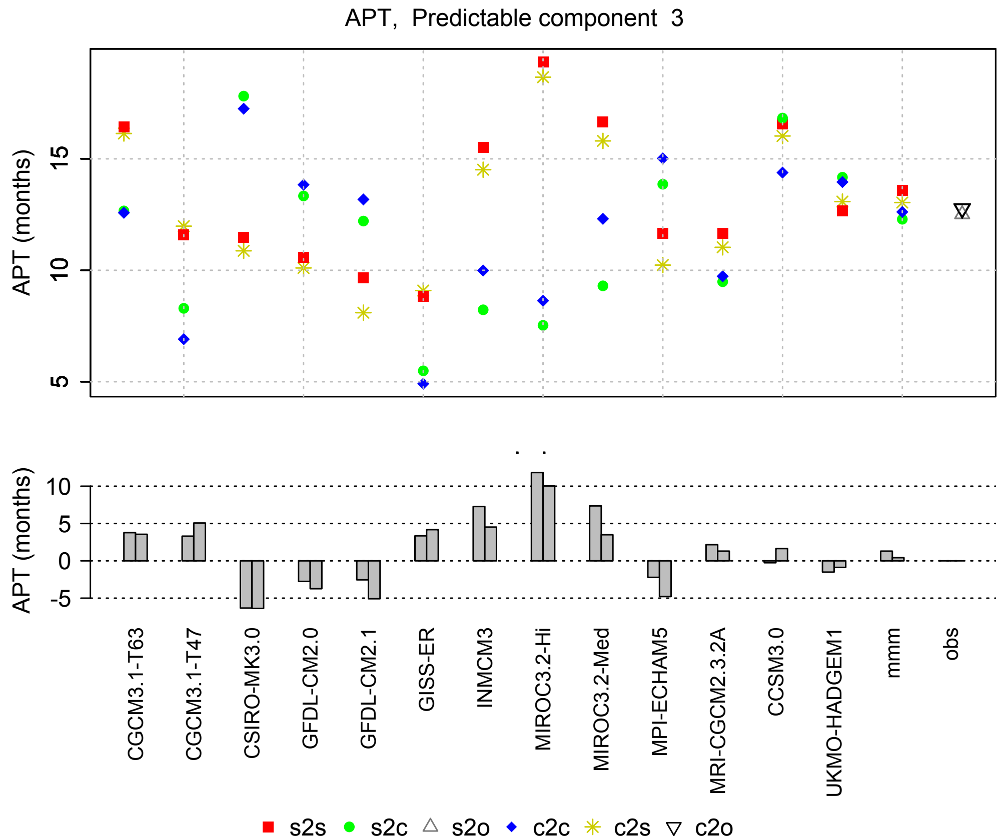

Figure 4.5: Same as figure 4.3, but for the third predictable component.

inspected individual predictable variates in these models to confirm that this difference is not the result of a spurious signal such as a trend. In a sense, then, these results suggest that ocean dynamics “suppresses” predictability in these models!

We also projected the predictable patterns on the regression operator derived from observations. The resulting APT values are shown on the far right hand side as the open triangles in fig. 4.3. First, both values ($\sim$ 13 months) are close to each other, which is not surprising considering the similarity of the first predictable patterns in slab and coupled models as shown in fig. 3.4. Also, the observational estimate lies in the lower tail of the slab model estimates, but in the middle of the coupled model estimates. Thus, although slab and coupled models have similar predictable patterns, coupled models tend to give more accurate magnitudes of the predictability, whereas slab models tend to overestimate the magnitude of predictability.

The various APT values for the second predictable component are shown in fig. 4.4. In contrast to the first component, the impact of ocean dynamics has no clear pattern in terms of APT– APT is larger for the coupled dynamics (s2s vs c2s) in nearly half the cases. Interestingly, observational estimates of APT for coupled and slab patterns are close to each other and close to that of the first pattern (~ 13 months). Similar conclusions hold for the third predictable component, shown in fig. 4.5.

4.4.3 Rate of Decay in Predictability

In this section we take a closer look at the decay of predictability in individual models. The R^2_τ for the most predictable component for the various cases are shown in fig. 4.6. We define the limit of predictability as the time at which R^2_τ curve hits the corresponding 95% significance level. The upper dashed curve in each panel shows the 95% significance level of R^2_τ in the slab version of a model and the lower dashed curve shows the corresponding level in the coupled version of that model. It is apparent that the significance level for slab models is much higher than their coupled counterparts due to the much smaller sample size of the slab models. Noticeably there is considerable model dependence of predictability as noted in other previous studies (for e.g., Jia and DelSole (2012)). Based upon the strict application of significance level, it appears that the predictability in the slab models (s2s) persists between 1 and 3 years whereas it persists for 5 years or longer in most of the coupled models (c2c). However, this conclusion should be taken carefully because it could most likely be an artifact of much smaller sample size in the slab models than in the coupled models. Remember that in chapter 3 where all the slab and coupled models were pooled together separately, the difference in their predictability was very small.

One of the major conclusion is that in most models, whether slab or coupled, predictability decreases rapidly in the first year. Typically, more than 50% of predictability is lost in

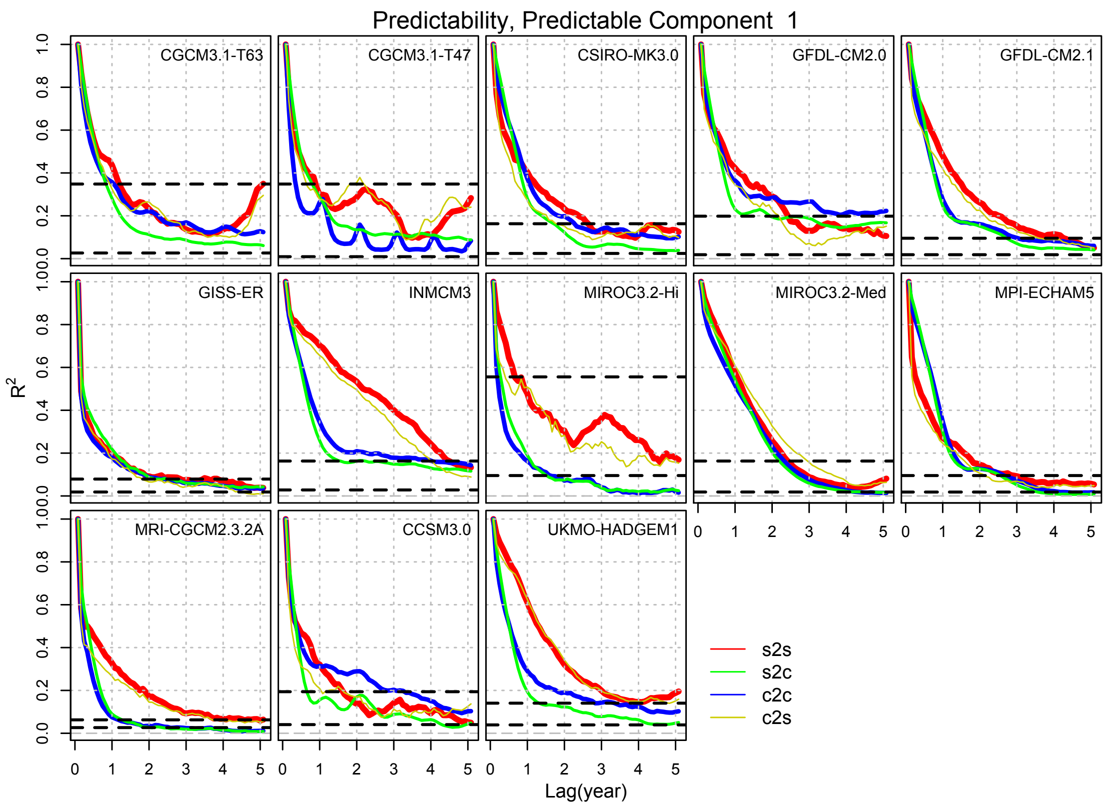

Figure 4.6: Predictability R_τ^2 for the first predictable component for the four cases s2s, s2c, c2s, c2c , where the first letter indicates the model-type from which the pattern is derived and the second letter indicates the model-type from which the regression operator is derived. In the context of (4.4), s2c means that $\mathbf{q}$ is derived from the slab models, and the covariance matrix $\mathbf{C}_0'$ and prediction operator $\mathbf{L'}_\tau$ are derived from the coupled models. The upper dashed curve in each panel shows the 95% significance level of R_τ^2 in the slab version of a model and the lower dashed curve shows the corresponding level in the coupled version of that model.

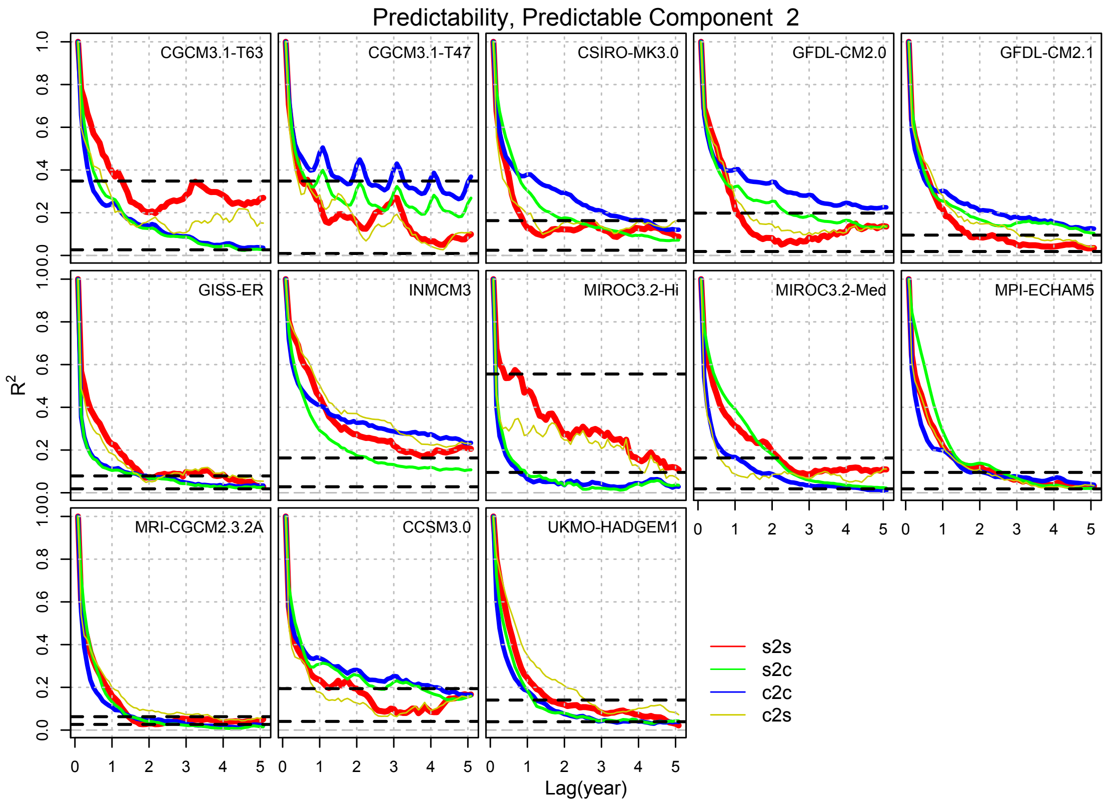

Figure 4.7: Same as figure 4.6, but for the second predictable component.

the first year. Most importantly, for the same dynamical system, both the slab and coupled patterns give similar predictability (compare s2s with c2s and c2c with s2c). This is a remarkable conclusion and supports the conclusion obtained in chapter three that the slab and coupled predictable patterns are similar. An interesting feature is that some of the R_τ^2 curves oscillate with an annual cycle (e.g. CGCM3.1-T47). We emphasize that the annual cycle has been removed from all time series, so the annual oscillations is not an artifact of climatology (consistent with the fact that other models do not show this behavior). Such annual oscillations also occur at local grid points and commonly interpreted in terms of the *re-emergence phenomenon*. It is possible that these oscillations may represent re-emergence.

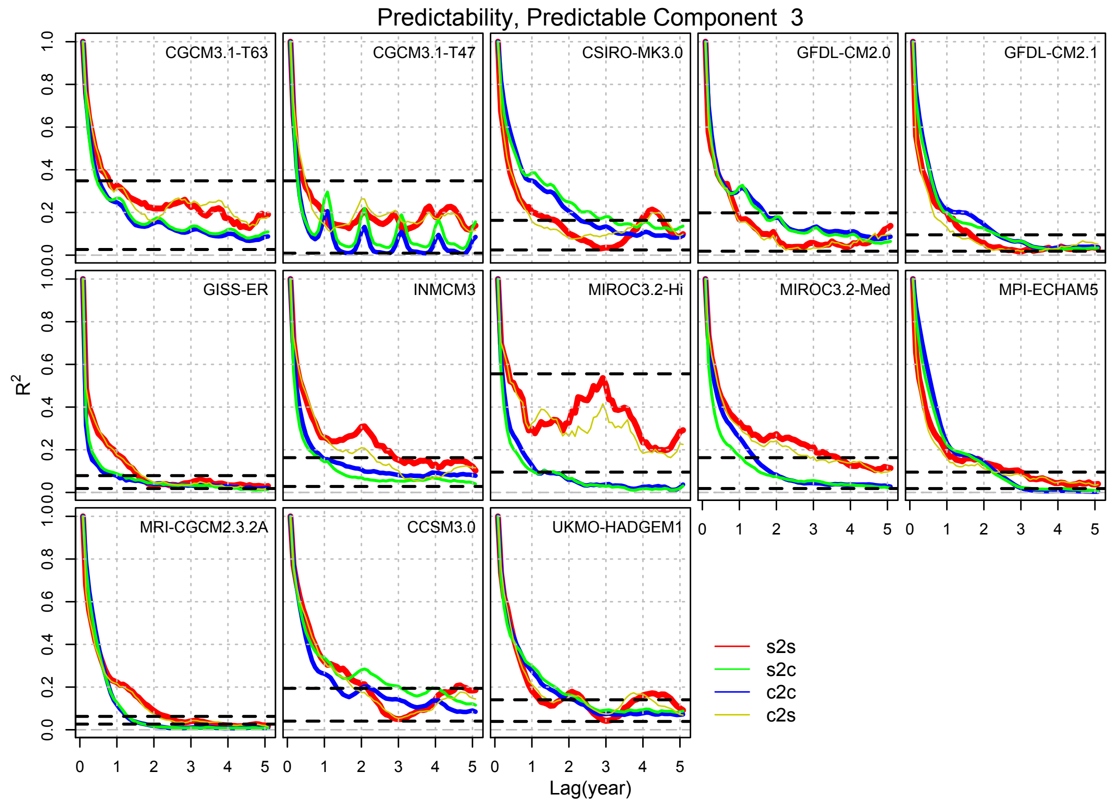

Figure 4.8: Same as figure 4.6, but for the third predictable component.

Predictability for the second and third predictable components are shown in figs. 4.7 and 4.8. A Similar conclusion as in the first component can be drawn for these components.

4.4.4 Forecast skill in individual models

The previous results are mostly model results– observations have not played a big role in the above analysis. In this section, we compare the forecast skills of various regression operators and various patterns. Thus, this section goes beyond pure model results and assesses the reality of model-derived predictable components.

The correlation skill of the most predictable (model) pattern is shown in fig. 4.9. It is apparent that forecast skill of all the models decreases rapidly and reduces to nearly 20%

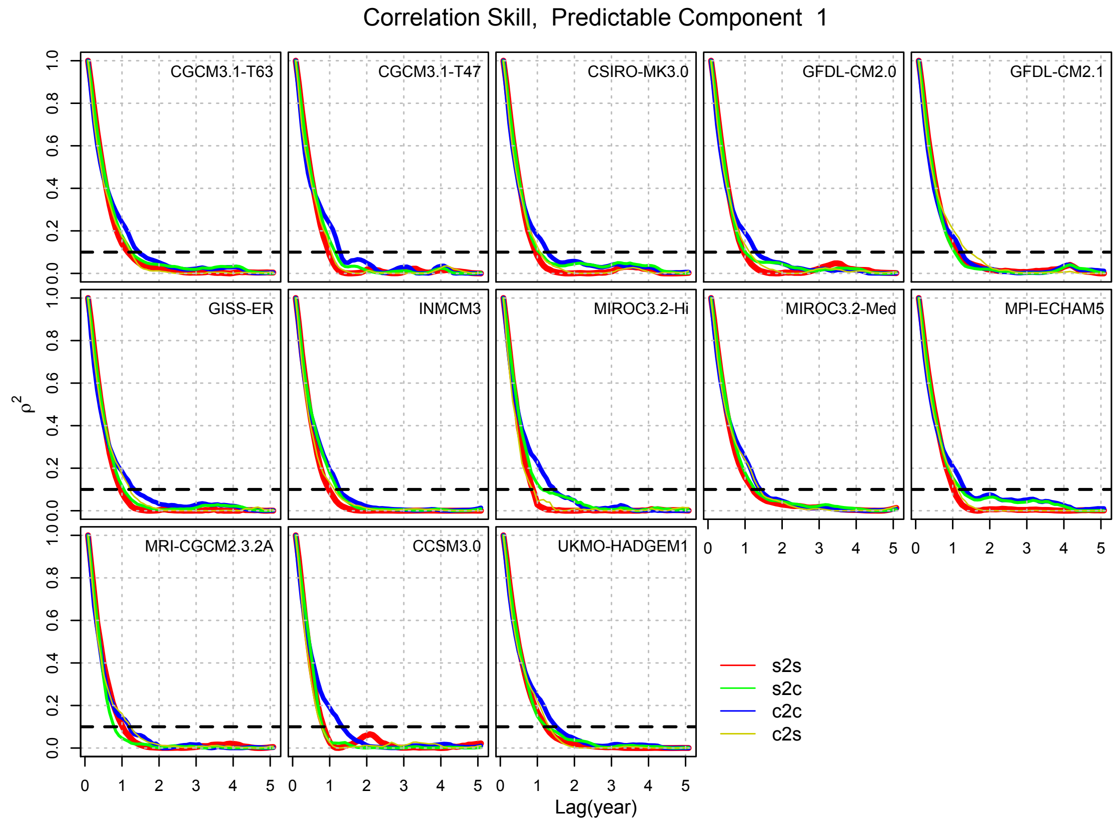

Figure 4.9: Correlattion skill for the first predictable component for the four cases s2s, s2c, c2s, c2c , where the first letter indicates the model-type from which the pattern is derived and the second letter indicates the model-type from which the regression operator is derived. In the context of (4.7) , s2c means that $\mathbf{q}$ is derived from the slab models, and the prediction operator $\mathbf{L}'^{m}_{\tau}$ is derived from the coupled model. The horizontal dashed line at 0.1 indicates the reference level above which the skill is assumed to be useful (a discussion about this is given in the section 4.3.

at the end of the first year. The skills of the various cases are nearly the same (1-1.5 years). An interesting feature is that despite of apparently higher predictability of coupled models as seen in figure 4.6, this higher predictability does not translate into higher predictive skill of coupled models relative to observations. Thus all the models, whether slab or coupled, exhibit similar prediction skill of around a year.

Correlation skill for the second predictable components is shown in the fig. 4.10. Similar to the first component, the skill of all models, both slab and coupled, decreases very rapidly in the first year. In almost all the slab models (s2s and c2s), skill exists only for around

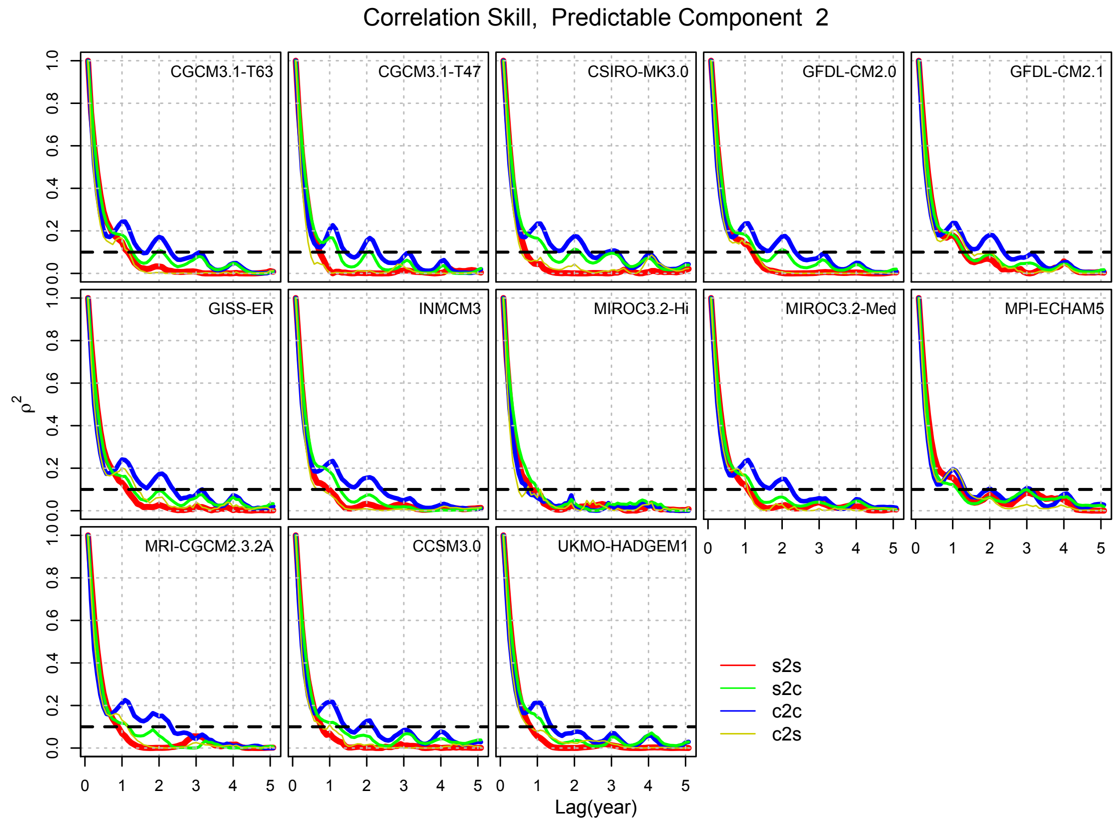

Figure 4.10: Correlation skill for the second predictable component: Similar to figure 4.9 but for the second predictable component.

a year only. An interesting feature is the annually oscillating correlation skill of the the coupled models (s2c and c2c). Since such oscillations are absent in the predictability of the models discussed above, it is possible that these oscillations might be related to the observations. Moreover, skill of most of the coupled models ($\sim$ 2 years) is slightly higher than that of the slab models ($\sim$ a year) and this enhancement seems to be related to the inclusion of ocean dynamics as well as the annual oscillation in the correlation skill (s2s vs s2c and c2c vs c2s). The correlation skills for the third component is shown in 4.11. The correlation skill decreases even more rapidly than in the first two components in the first year and skill remains only for around a year in both the slab and coupled models and for all the cases.

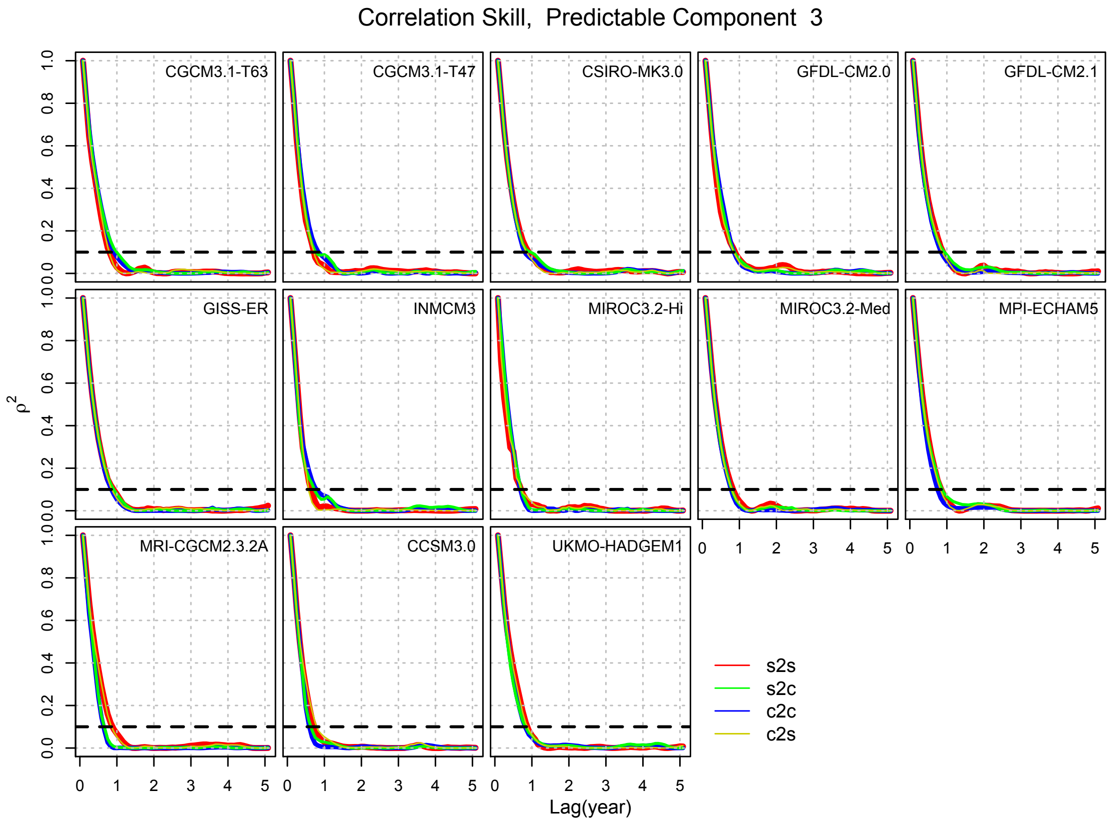

Figure 4.11: Correlation skill for the third predictable component: Similar to figure 4.9 but for the third predictable component.

4.5 Summary

In this chapter, we diagnosed predictability timescale (APT), predictability limit and forecast skill of models on model-by-model basis. The objective was to investigate if some models are outliers, in the sense that their predictability and skill differ a lot from the multimodel mean. A comparison of maximized APT across individual slab models reveals that the largest APT differs by a factor of two, indicating that a large range of predictability can arise simply from differences in atmospheric dynamics. Importantly, APT values obtained by using multimodel slab pattern is largely similar to that obtained by using model specific slab pattern. This shows that multimodel slab pattern does not miss important predictability in individual slab model, thus strengthening the results obtained in chapter

3. Strikingly, the same conclusion holds for coupled models. For the first component, APT values in the slab models are larger than their coupled counterparts- a result that counters the argument that inclusion of ocean dynamics enhances predictability. However, the impact of ocean dynamics has no clear pattern in the other components diagnosed.

Based upon strict application of significance levels to R^2_τ, it appears that, for all the components diagnosed, predictability in most of the coupled models is higher than that in their slab counterparts. For instance, for the first component, the predictability in the coupled models persists for 5 years or longer, whereas in the slab models it persists between 1 and 3 years. However, this conclusion should be taken with caution as the much smaller sample size artificially raises the significance threshold for the slab models. A fair comparison of the predictability in the slab and coupled models should be done when the sample size is large enough and comparable in both the models. This point is also important as the predictability of the slab and coupled models were comparable as in chapter 3 when model data were pooled together in the slab and coupled simulations respectively.

The most striking result in this chapter is confirmation of our conclusion from chapter 3: the most predictable patterns in slab and coupled models have similar predictabilities. Although the magnitude of predictability is sensitive to model, the spatial structures of the most predictable components are not.

An analysis of correlation skill reveals that for all the components diagnosed the skill of both the coupled and slab models decreases rapidly in the first year with around 80% skill lost in the first year. The skill of the coupled and slab models are comparable and persists for around a year in all the components diagnosed except for component 2 in which coupled models have higher skill ($\sim$ 2 years) than their slab counterparts. These results are consistent with the results shown in chapter 3 and in Srivastava and DelSole (2017) where multimodel skills of coupled and slab models were comparable except for the component 2.

Chapter 5: Stochastic model

5.1 Motivation

The previous results suggest that interactive ocean dynamics are not essential for decadal predictability. Nevertheless, the mechanisms of this predictability are far from clear: although slab models have a relatively simple ocean, the atmosphere is based on a comprehensive primitive equation model with moist processes. As a result, isolating the precise mechanisms responsible for decadal predictability in slab models is difficult because these models are nonlinear, chaotic, and simulate many complex physical processes. On the other hand, Hasselmann-type models use simplistic atmospheric models that do not have spatially coherent responses to ocean temperature anomalies. To gain insight into the physical mechanisms, we built a model that is intermediate between the one-dimensional Hasselmann model and the nonlinear AGCM-mixed layer models.

The model we have built is a stochastically forced, linearized primitive equation model coupled to a slab mixed layer ocean model. The stochastic forcing in this model serves a fundamentally different role than in the Hasselman model. In the Hasselmann model, the stochastic forcing represents atmospheric heat fluxes in a non-interactive fashion; that is, the stochastic forcing is simply imposed and does not change in response to ocean temperatures. In contrast, in our model, the stochastic forcing excites atmospheric eddies, and then these eddies interact with slab ocean model. As a result, the atmospheric heat fluxes in this model depend on the slab temperatures and therefore may change their behavior and interact with the ocean temperature. Thus, the atmospheric forcing seen by the ocean model is *dynamically constrained* by primitive equations. To be clear, our stochastic forcing parameterizes not the atmospheric fluctuations themselves, but the eddy-eddy nonlinear interactions of large-scale atmospheric eddies. Thus, the spatial structure of the atmospheric forcing is *derived* from the primitive equation, rather than imposed by the forcing. The stochastic atmospheric model used here has been used successfully in the past to investigate weather scale phenomena. For example, Whitaker and Sardeshmukh (1998) successfully predicted a wide variety of storm-track behavior, including certain lag-covariances. Zhang and Held (1999) presented a stochastic model, based on the primitive equations for zonally varying background flows, that could capture the variances and fluxes, the midwinter suppression, and storm track responses to El Nino. Our goal is to determine whether models of this type can generate realistic decadal predictability when coupled to an ocean mixed layer. Our premise is that since the atmospheric stochastic model generates more realistic eddy structures, it is plausible that it also will generate more realistic low-frequency variability when coupled to a mixed-layer ocean model.

5.2 Description of the Model

The dynamical core of our model is based on the primitive equation model linearized about a zonally symmetric basic state. In previous atmospheric stochastic models, Newtonian relaxation was used to parameterize radiative effects. Unfortunately, Newtonian cooling does not provide the information necessary to specify fluxes at the surface of the mixed layer model. Accordingly, we use a gray radiative transfer model that predicts upward and downward fluxes, following Frierson et al. (2006). We also use standard bulk formulas for sensible heat fluxes. We add linear dissipation and stochastic forcing to parameterize the eddy-eddy nonlinear interactions. In the following subsections we present a more complete description of our model.

5.2.1 Radiation Scheme

Since our atmospheric model is coupled to the ocean mixed layer through the surface fluxes, thermal forcing needs to be prescribed in such a way that the upward and downward fluxes at the surface are known. This requirement is not met by traditional Newtonian relaxation. We chose a gray radiative transfer scheme with specified long wave absorber distribution as a

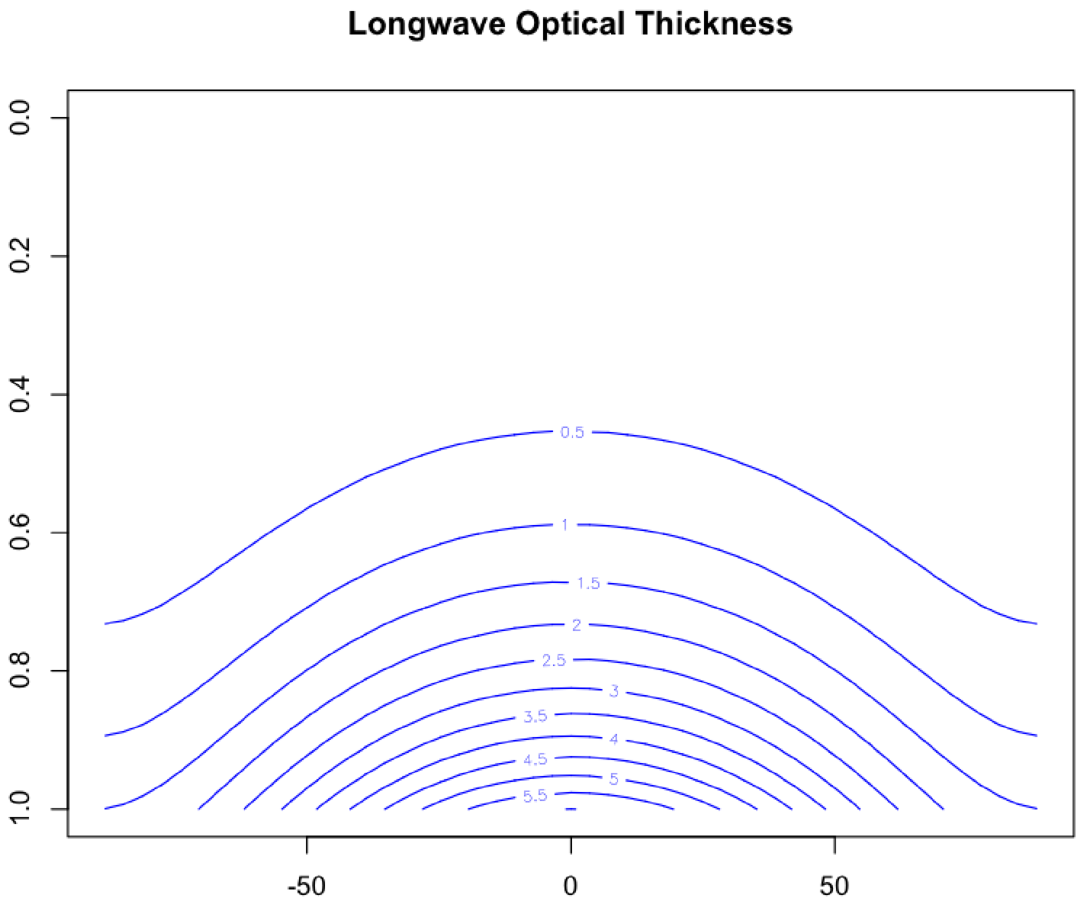

Figure 5.1: The assumed optical depth for longwave radiation.

function of pressure, as in Frierson et al. (2006). This approach ignores changes in absorber distribution that may occur as the system evolves, like those associated with clouds. We also assume that solar radiation is not absorbed by the atmosphere and has no seasonal or diurnal cycle. The solar flux is specified as

$$Q = R_{sol0}\left(1 + \Delta_s p_2(\theta)\right) \tag{5.1}$$

where

$$p_2(\theta) = \frac{1}{4}\left(1 - 3\sin^2\theta\right) \tag{5.2}$$

is the second Legendre polynomial. R_{sol0} is the global mean net solar flux, and Δ_s controls the meridional temperature gradients. The optical depth is specified as

$$\tau = \left(\tau_{0e} + (\tau_{0p} - \tau_{0e})\sin^2\theta\right)\left(f\frac{p}{\pi} + (1-f)\left(\frac{p}{\pi}\right)^4\right) \tag{5.3}$$

where τ_{0e} and τ_{0p} give surface values of longwave optical depths at the equator and poles respectively, and π is the surface pressure. The longwave optical depth profile of (5.3) is shown in figure 5.1. If both scattering and atmospheric motions are ignored, then the Schwarzschild equations for radiative transfer and the first law of thermodynamics give

$$\frac{\partial U}{\partial \tau} = U - \xi T^4 \tag{5.4a}$$

$$\frac{\partial D}{\partial \tau} = \xi T^4 - D \tag{5.4b}$$

$$\frac{\partial T}{\partial t} = \frac{g}{\pi c_{air}}\frac{\partial (U-D)}{\partial \sigma} \tag{5.4c}$$

where U and D are the upward and downward infrared fluxes, respectively, T is Temperature, and τ is the optical depth measured from the top of the atmosphere downward. In a gray atmosphere, optical depth is related to vertical distance as

$$d\tau = -k\rho dz \tag{5.5}$$

where k is a constant. At the top of the atmosphere we have

$$\tau = 0 \;\; and \;\; D = 0 \tag{5.6}$$

and the bottom of the atmosphere is connected to the ocean mixed layer through the upward and downward fluxes at the surface. The parameters for the radiation scheme is listed in Table 5.1.

Table 5.1: Parameters for the Radiation Scheme

Parameter	Interpretation	Value
ξ	Stefan-Boltzman Constant	$5.6734 \times 10^{-8}\, Wm^{-2}K^{-4}$
α	albedo	0.31
R_{sol0}	Solar Constant	$1360\, Wm^{-2}$
Δ_s	latitudinal variation of SW radiation	1.4
τ_{0e}	longwave optical depth at the equator	6
τ_{0p}	longwave optical depth at the pole	1.5
f	linear optimal depth parameter (for stratosphere)	0.1
V_0	Nominal velocity	1 m/sec

5.2.2 Surface Fluxes

The surface exchange of heat and momentum fluxes between the atmosphere and ocean is parameterized using bulk aerodynamic formula. Surface stress is parameterized as

$$\Gamma_s = \rho_a C_D \mathbf{V_a}, \tag{5.7}$$

and sensible heat flux is parameterized as

$$\mathbf{H} = \rho_a C_{air} C_Q \left(|\mathbf{V}_a| + V_0\right) \left(T_s - T_a\right), \tag{5.8}$$

where C_{air} is the heat capacity of the air at constant pressure; T_s is the temperature of the ocean mixed layer; ρ_a and T_a are density and temperature of air at the lowest atmospheric model interface; C_D and C_Q are bulk transfer coefficients for momentum and sensible heat flux; $\mathbf{V}_a$ is the horizontal wind at the lowest model interface, parameterized as 0.49 times the wind at the lowest model level. The parameter V_0 is a "nominal" velocity that ensures sensible heat fluxes exist even with no surface wind (as observed), and prevents singularities that would otherwise occur when linearizing about $\mathbf{V}_a = 0$. We have chosen the same values for C_D and C_Q, namely 0.002.

5.2.3 Vertical Diffusion

We have also parameterized turbulent momentum fluxes as a diffusive process, where stress in a layer can be written as

$$\Gamma = -\frac{\rho_a^2 g}{\pi} K_M \frac{\partial \mathbf{V}}{\partial \sigma} \tag{5.9}$$

while the boundary condition at the top is no stress, i.e., $\Gamma = 0$ at top. K_M is the exchange coefficient (4×10^{-6}).

5.2.4 Ocean Mixed Layer

The lower boundary condition in our model is an aquaplanet with no topography. The ocean is parameterized as slab mixed layer with depth h . The thermodynamic equation for the ocean mixed layer is

$$h \rho_{water} c_{water} \frac{\partial T_s}{\partial t} = Q(1 - \alpha) + D_s - U_s \tag{5.10}$$

where Q is the net solar incident radiation, α is the albedo, U_s and D_s are the upward and downward infrared fluxes evaluated at the surface, and T_s is the temperature of the mixed layer. We assume that the mixed layer is a black body, which implies that the bottom of the atmosphere has the boundary condition

$$U_s = \xi T_s^4 \tag{5.11}$$

5.2.5 Dynamical Core

The dynamical core of our model consists of six equally spaced sigma levels, with the lowest level at 1000 mb and top level at 0 mb, and 51 grid points in latitudinal direction. The dynamical core is represented by zonally averaged primitive equations linearized about the basic state flow. The nonlinear primitive equations are

$$\frac{D\mathbf{v}}{Dt} = -\nabla\Phi - \sigma\alpha\nabla\pi - f\mathbf{k}\times\mathbf{v} + \mathbf{F} + \text{curvature terms} \tag{5.12}$$

$$\frac{\partial\Phi}{\partial\sigma} = -\pi\alpha \tag{5.13}$$

$$\frac{\partial\pi}{\partial t} = -\nabla\cdot(\pi\mathbf{v}) - \pi\frac{\partial\dot{\sigma}}{\partial\sigma} \tag{5.14}$$

$$c_{air}\frac{DT}{Dt} = \alpha\omega + Q \tag{5.15}$$

where

$$\alpha = RT/P \tag{5.16}$$

$$\omega = \pi\dot{\sigma} + \sigma\left(\frac{\partial\pi}{\partial t} + \mathbf{v}\cdot\nabla\pi\right) \tag{5.17}$$

$$\sigma = (p - p_{top})/\pi, \tag{5.18}$$

and where ω is vertical velocity in sigma coordinates, α is specific volume of the air, and π is the surface pressure. p_{top} is the pressure at the top of the atmosphere. Other symbols are standard. This set of equations are linearized about the mean flow such that all second order perturbation terms are neglected.

5.2.6 Linearized form of Equations

In the previous sections we presented the nonlinear form of equations that were linearized about the zonally averaged flow. The linearized equations are mentioned in this section. To linearize the equations, each variable A is written as $A = \overline{A} + A'$, where $\overline{A}$ is the zonal average of the variable A and the term A' denotes the longitudinal variation about zonal mean $\overline{A}$. We further use the fact that $\partial\overline{(\;)}/\partial x = 0$ and $\overline{A'} = 0$.

The Schwarzschild equations for radiative transfer 5.4a, 5.4b and the associated first law of thermodynamics 5.4c are expressed in the linearized form as

$$\frac{\partial U'}{\partial \tau} = U' - 4\xi \overline{T}^3 T' \tag{5.19a}$$

$$\frac{\partial D'}{\partial \tau} = 4\xi \overline{T}^3 T' - D' \tag{5.19b}$$

$$\frac{\partial T'}{\partial t} = \frac{g}{\overline{\pi} c_{air}} \frac{\partial (U' - D')}{\partial \sigma} - \frac{\partial \overline{T}}{\partial t} \frac{\pi'}{\overline{\pi}}. \tag{5.19c}$$

The linearized form of sensible heat flux equation 5.8 is

$$\mathbf{H}' = C_{air} C_Q ((u_a^2 + v_a^2)^{1/2} + V_0) \Bigg[\rho_a \left(T_s' - T_a' \right)$$

$$+ (T_s - T_a) \rho_a \frac{(u_a' \overline{u_a} + v_a' \overline{v_a})}{\left((u_a^2 + v_a^2)^{1/2} + V_0 \right)^2} + (T_s - T_a) \rho_a' \Bigg]. \tag{5.20}$$

The linearized form of stress terms 5.9 are

$$\Gamma_x = -\frac{\overline{\rho^2} g K_M}{\overline{\pi}} \left[(\frac{2\rho'}{\overline{\rho}} - \frac{\pi'}{\overline{\pi}})(\frac{\partial \overline{u}}{\partial \sigma}) + \frac{\partial u'}{\partial \sigma} \right] \tag{5.21a}$$

$$\Gamma_y = -\frac{\overline{\rho^2} g K_M}{\overline{\pi}} \left[(\frac{2\rho'}{\overline{\rho}} - \frac{\pi'}{\overline{\pi}})(\frac{\partial \overline{v}}{\partial \sigma}) + \frac{\partial v'}{\partial \sigma} \right]. \tag{5.21b}$$

The linearized version of ocean mixed layer equation 5.10 is

$$h \rho_{water} c_{water} \frac{\partial T_s'}{\partial t} = D_s' - U_s'. \tag{5.22}$$

The linearized from of momentum equations 5.12 are

$$\frac{\partial u'}{\partial t} = -\frac{v'}{a}\frac{\partial \overline{u}}{\partial \phi} - \frac{\overline{v}}{a}\frac{\partial u'}{\partial \phi} - \dot{\sigma}'\frac{\partial \overline{u}}{\partial \sigma} - \bar{\dot{\sigma}}\frac{\partial u'}{\partial \sigma}$$

$$+ \frac{\overline{u}v'tan\phi}{a} + \frac{u'\overline{v}tan\phi}{a} + fv' \tag{5.23a}$$

$$\frac{\partial v'}{\partial t} = -\frac{v'}{a}\frac{\partial \overline{v}}{\partial \phi} - \frac{\overline{v}}{a}\frac{\partial v'}{\partial \phi} - \dot{\sigma}'\frac{\partial \overline{v}}{\partial \sigma} - \bar{\dot{\sigma}}\frac{\partial v'}{\partial \sigma}$$

$$+ \frac{2\overline{u}u'tan\phi}{a} - fu' - \frac{1}{a}\frac{\partial \Phi'}{\partial \phi} - \frac{\sigma\alpha'}{a}\frac{\partial \overline{\pi}}{\partial \phi} - \frac{\sigma\overline{\alpha}}{a}\frac{\partial \pi'}{\partial \phi}. \tag{5.23b}$$

The linearized version of hydrostatic equation 5.13 is

$$\frac{\partial \Phi'}{\partial \sigma} = -\pi'\overline{\alpha} - \overline{\pi}\alpha'. \tag{5.24}$$

The linearized form of continuity equation 5.14 can be written as

$$\frac{\partial \pi'}{\partial t} = -\frac{1}{acos\phi}\frac{\partial}{\partial \phi}(\overline{\pi}v'cos\phi) - \frac{1}{acos\phi}\frac{\partial}{\partial \phi}(\pi'\overline{v}cos\phi) - \pi'\frac{\partial \bar{\dot{\sigma}}}{\partial \sigma} - \overline{\pi}\frac{\partial \dot{\sigma}'}{\partial \sigma}. \tag{5.25}$$

The linearized form of thermodynamic equation 5.15 is

$$c_{air}\frac{\partial T'}{\partial t} = -c_{air}\left[\frac{\overline{v}}{a}\frac{\partial T'}{\partial \phi} + \frac{v'}{a}\frac{\partial \overline{T}}{\partial \phi} + \bar{\dot{\sigma}}\frac{\partial T'}{\partial \phi} + \dot{\sigma}'\frac{\partial \overline{T}}{\partial \phi}\right] + \overline{\alpha}\omega' + \alpha'\overline{\varpi} + Q'. \tag{5.26}$$

5.2.7 Discretization and Conservation Laws

Unlike the continuous equations, the discretized equations can not satisfy all conservation laws. Hence, the discretization is constructed in a way that satisfies the physical laws of conservation. These considerations require that the advection terms be represented in flux form; and the conservations of kinetic energy and angular momentum require that certain terms, such as Coriolis terms and curvature terms, be represented in a special form. For example, the Coriolis term in the meridional momentum equation is written as

$$\left(\widehat{fu}\right)_j = \frac{\Omega}{2\cos\phi_j \Delta\phi_j}\left[\cos\phi_{j+\frac{1}{2}}\left(\widehat{\cos^2\phi}\right)_{j+\frac{1}{2}}\left(\frac{u_j}{\cos\phi_j} - \frac{u_{j+1}}{\cos\phi_{j+1}}\right) + \right.$$

$$\cos\phi_{j-\frac{1}{2}}\left(\widehat{\cos^2\phi}\right)_{j-\frac{1}{2}}\left(\frac{u_{j-1}}{\cos\phi_{j-1}} - \frac{u_j}{\cos\phi_j}\right) +$$

$$\left.\cos\phi_{j+\frac{1}{2}}\left(u_{j+1}\cos\phi_{j+1} - u_j\cos\phi_j\right) + \cos\phi_{j-\frac{1}{2}}\left(u_j\cos\phi_j - u_{j-1}\cos\phi_{j-1}\right)\right]. \quad (5.27)$$

The derivation of this and other differencing schemes is tedious and therefore omitted from this report. The conservation properties of the differencing scheme have been verified by separate off-line analysis.

5.2.8 Stochastic Model

We now present our method for solving the statistics of the stochastic model; further details can be found in DelSole (2004). The state of the system is specified by the values of U, V, T, T_s, π at all latitudes and appropriate levels and can be represented by the N-dimensional vector $\mathbf{g}(\mathbf{t})$. The governing equations for this system can be expressed as a stochastic differential set of equations of the form

$$\dot{\mathbf{g}} = \mathbf{A}\mathbf{g} + \mathbf{w}, \quad (5.28)$$

where $\mathbf{A}$ is an $N \times N$ matrix, independent in time, called the dynamical operator, and $\mathbf{w}(\mathbf{t})$ is an N-dimensional stochastic process, often called noise. The matrix $\mathbf{A}$ is assumed to be stable - that is, all its eigenvalues have negative real parts. The operator $\mathbf{A}$, being independent of time, can be diagonalized by a normal mode transformation

$$\mathbf{A} = \mathbf{Z}\boldsymbol{\Lambda}\mathbf{Z}^{-\mathbf{1}}, \quad (5.29)$$

where the columns of $\mathbf{Z}$ give the eigenmodes, and $\mathbf{\Lambda}$ is a diagonal matrix whose diagonal elements give the eigenvalues of the dynamical operator. If we assume that $\mathbf{w}$ is independent and identically distributed Gaussian white noise with zero mean, then covariance matrix of the noise can be written as

$$\langle \mathbf{w}(t+\tau)\mathbf{w}^{\mathbf{H}}(t)\rangle = \mathbf{Q}\delta(\tau) \tag{5.30}$$

where δ is the dirac delta function and τ is the time lag. The angular bracket denotes an average over an ensemble of realizations of the forcing. The superscript $\mathbf{H}$ denotes the conjugate transpose. We are interested primarily in the eddy fluxes and variances, and in the time-lagged covariances, produced by the stochastic model. These statistical quantities, as well as many others, are contained in the time-lagged covariance matrix

$$\mathbf{C}_\tau(t) = \langle \mathbf{g}(t+\tau)\mathbf{g}^{\mathbf{H}}(t)\rangle. \tag{5.31}$$

It can be shown (DelSole, 2004) that the covariance matrix produced by the stochastic model is

$$\mathbf{C_0}(t) = e^{\mathbf{A}t}\mathbf{C_0}(0)e^{\mathbf{A^H}t} + \mathbf{Z}(\mathbf{Z^{-1}QZ^{-1H}} \circ \mathbf{E_t})\mathbf{Z^H}, \tag{5.32}$$

where $\circ$ denotes the Schur product and

$$(E_t)_{ij} = \frac{e^{(\Lambda_i+\Lambda_j)t} - 1}{\Lambda_i + \Lambda_j^*}. \tag{5.33}$$

Further, the lag covariance matrices $\mathbf{C}_\tau$ are related to $\mathbf{C_0}$ as

$$\mathbf{C}_\tau(t) = \begin{cases} \exp(\mathbf{A}\tau)\mathbf{C_0}(t) & \tau > 0 \text{ and } t > 0 \\ \mathbf{C_0}(t)\exp(-\mathbf{A^H}\tau) & \tau < 0 \text{ and } t+\tau > 0 \end{cases} \tag{5.34}$$

In the limit of very long time, equations (5.32) and (5.33) become

$$\mathbf{C_0}(\infty) = \mathbf{Z}(\mathbf{Z^{-1}QZ^{-1H}} \circ \mathbf{E}_\infty)\mathbf{Z^H} \tag{5.35}$$

and

$$(E_\infty)_{ij} = \frac{-1}{\Lambda_i + \Lambda_j^*} \tag{5.36}$$

respectively. We will use equation (5.35) to compute the *stationary* covariance matrix of the response of the stochastic model. The power spectrum of (5.34) is defined by the Wiener-Khinchin theorem

$$\mathbf{P}(\omega) = \frac{1}{2\pi}\int_{-\infty}^{\infty} \mathbf{C}_\tau e^{i\omega\tau} d\tau. \tag{5.37}$$

Using (5.34), (5.37) reduces to

$$\mathbf{P}(\omega) = \frac{1}{2\pi}\mathbf{Z}(\mathbf{Z^{-1}QZ^{-1H}} \circ \hat{\mathbf{E}}_\omega)\mathbf{Z^H} \tag{5.38}$$

where

$$\mathbf{E}_\omega = \frac{1}{(i\omega + \Lambda_i)(-i\omega + \Lambda_j^*)} \tag{5.39}$$

We shall use (5.39) to compute the power spectrum of the stochastically forced eddies.

5.3 Data and Model Parameters

For our first set of experiments, we linearize the stochastic model about the zonally averaged JFM mean U, V and T averaged over the period 1979-2012 from ERA -Interim data. These fields are shown in figs. 5.2a and 5.2b. The surface pressure is specified to be constant (10^5 mb). The mean SST is approximated by adding a constant temperature ($0.8\,^\circ C$) to the atmospheric temperature at the lowest interface. By approximating the mean SST this way, we ensure that climatological surface sensible heat heat flux is directed from the ocean to the atmosphere, as seen in the observed zonal mean system. We specially adjust the parameters of our model to generate second moment statistics similar to observations. Specifically, we stochastically force temperature at all levels except the top, with variance that maximizes at $45°$ and decays away as a Gaussian with a standard deviation of 12.5 degrees. In order to have stable solutions, we have introduced a constant 'artificial damping' of 1 day^{-1} everywhere in the model. The damping is introduced as part of the nonlinear eddy-eddy parameterization. The value of 1 day^{-1} was chosen to stabilize the system and to avoid resonance. This value is comparable to that used in other stochastic models based on the primitive equations (Zhang and Held, 1999). Also, this value does not dominate the dynamics, as indicated by the fact that the covariance matrix derived from this damping has non-zero off-diagonal elements. All calculations have been done for zonal wave number 6.

5.4 Model Simulations

5.4.1 Gray Radiation Simulation

We first perform a stability analysis of the model with just the pure gray radiation model. In the absence of dynamics, each vertical column is decoupled from all other columns and the stability can be computed for each column separately. An example of the eigenmodes in a particular column is shown in fig. 5.3. All eigenvalues are real and negative, corresponding to pure damping, and range from nearly 5 days in the lowest levels to 100 days in the uppermost layers. These calculations imply that the grey radiation scheme effectively damps temperature.

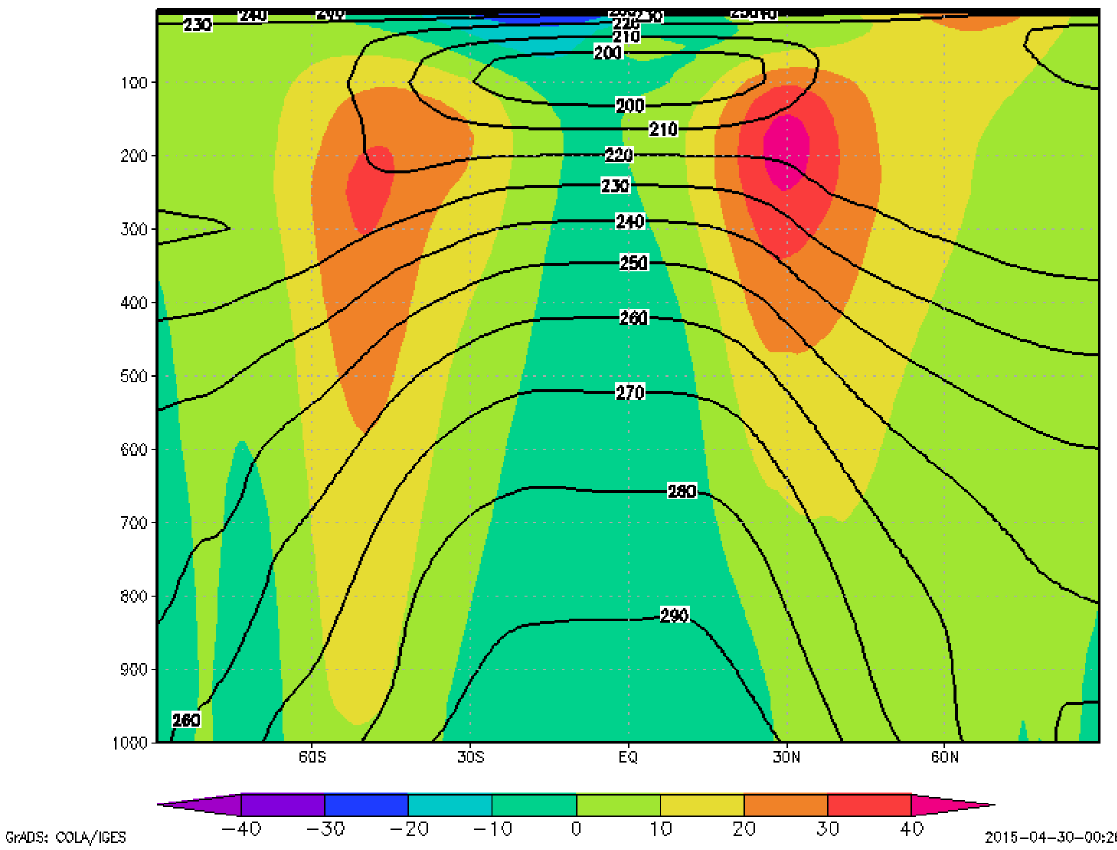

Figure 5.2a: Zonally averaged zonal velocity (shaded; unit:m/sec) and temperature (contour; unit:K) averaged over January, February, March for the period 1979-2012 derived from ERA-INTERIM data.

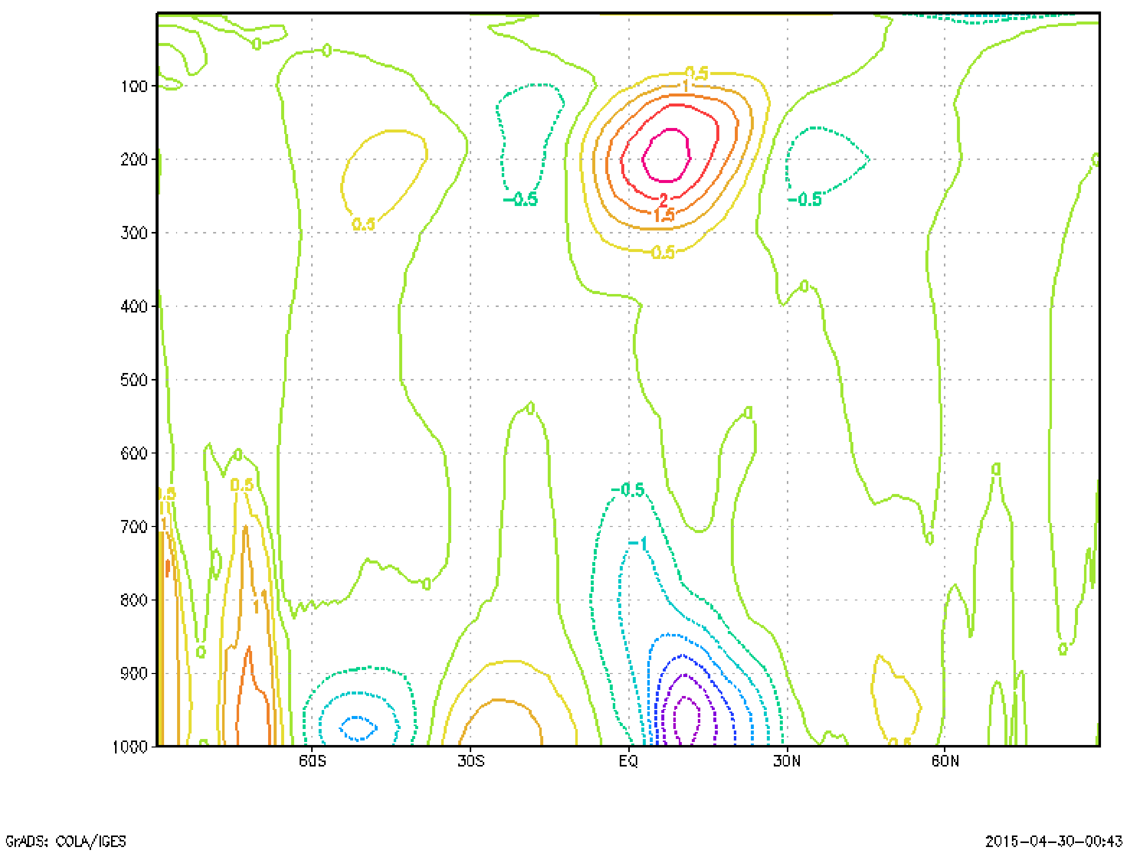

Figure 5.2b: Zonally averaged meridional velocity (unit:m/sec) averaged over January, February, March for the period 1979-2012 derived from ERA-INTERIM data.

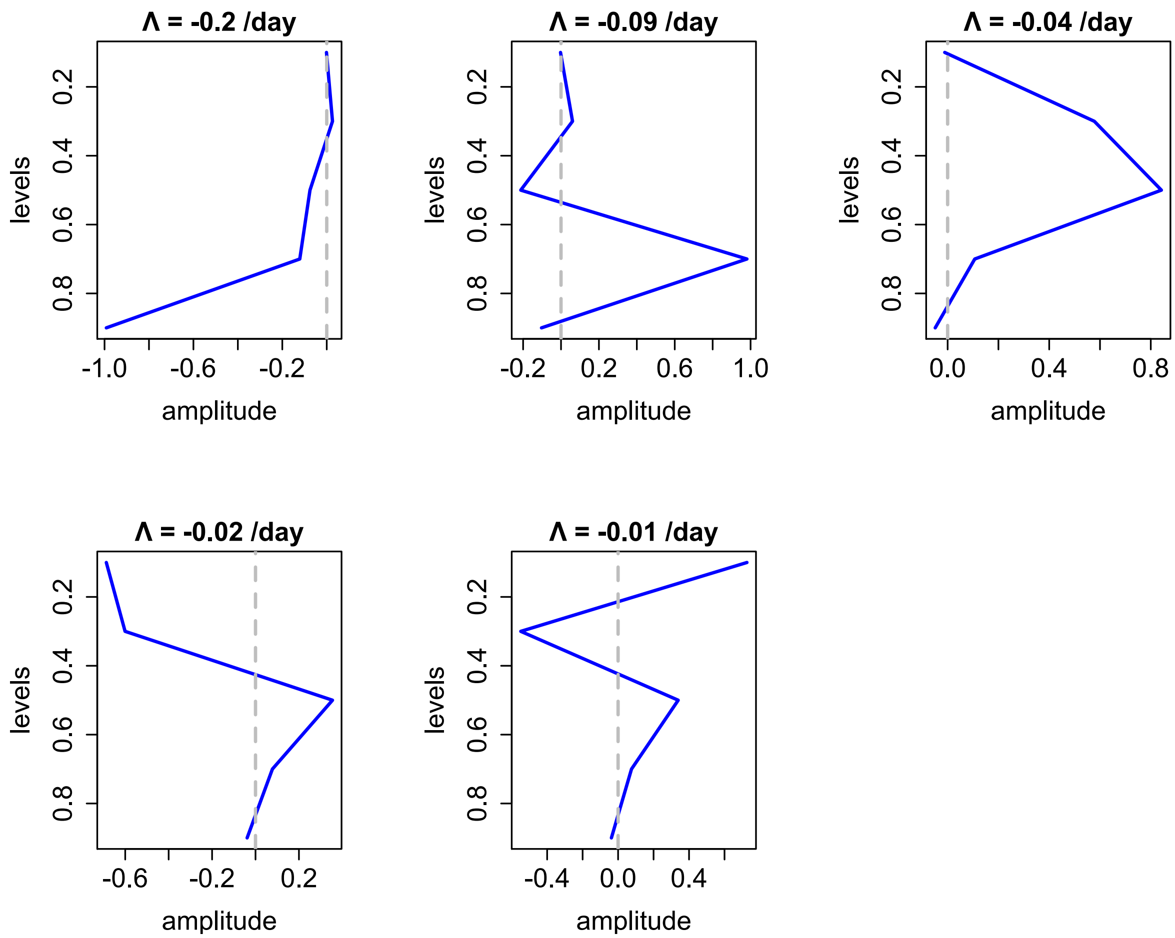

Figure 5.3: Eigenvectors of the pure radiation model as a function of vertical sigma level. The corresponding eigenvalues are indicated in the title. The dashed line indicates zero, for reference.

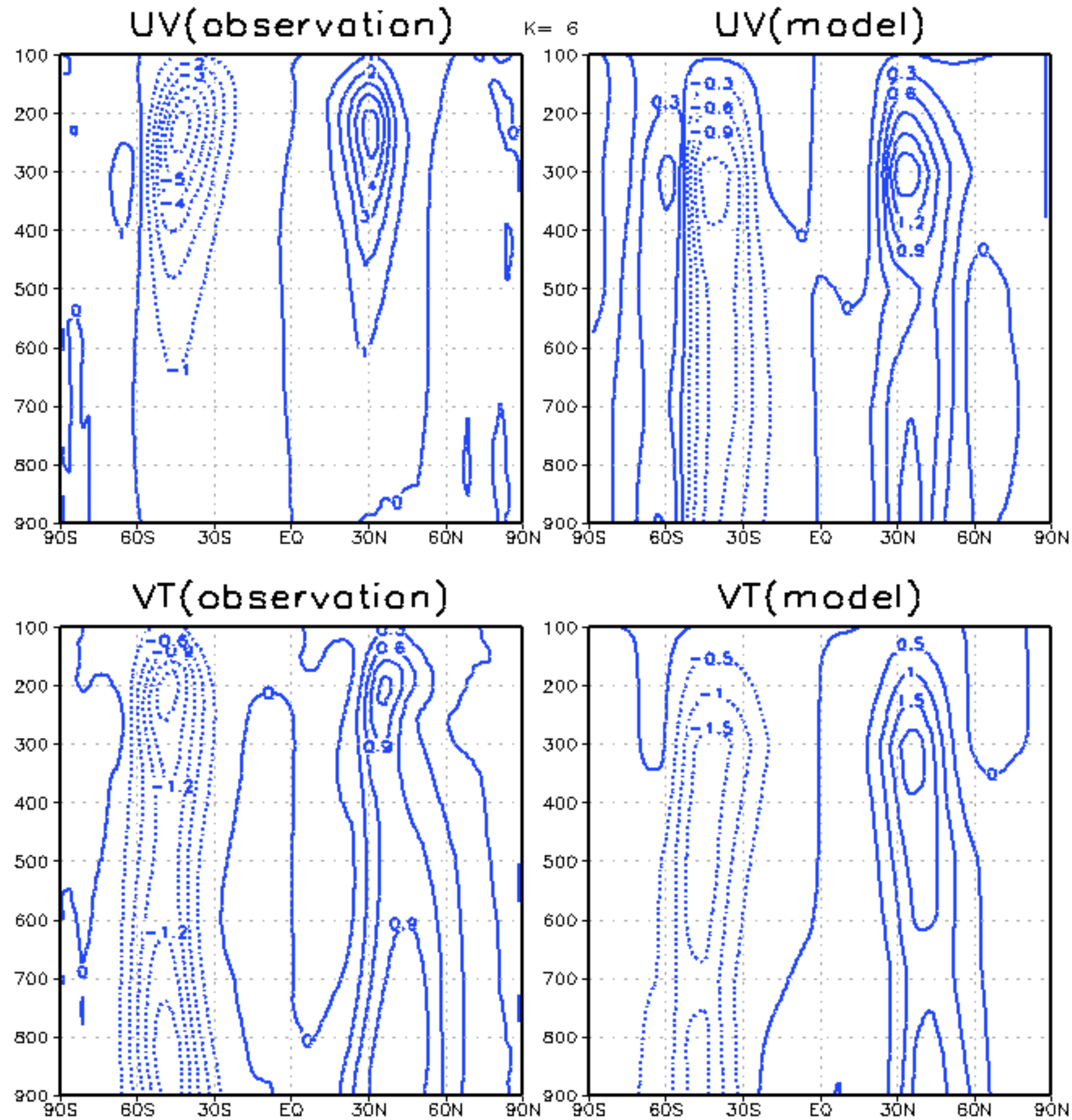

Figure 5.4a: Eddy fluxes for zonal wavenumber six during JFM from observations (left column) and as generated by a 5-layer atmospheric stochastic model (right column). The stochastic model is based only on the atmosphere with no ocean mixed layer or radiation, and has temperature forcing that is uncorrelated in space and reaches maximum variance at 45° and decays away latitudinally as a Gaussian.

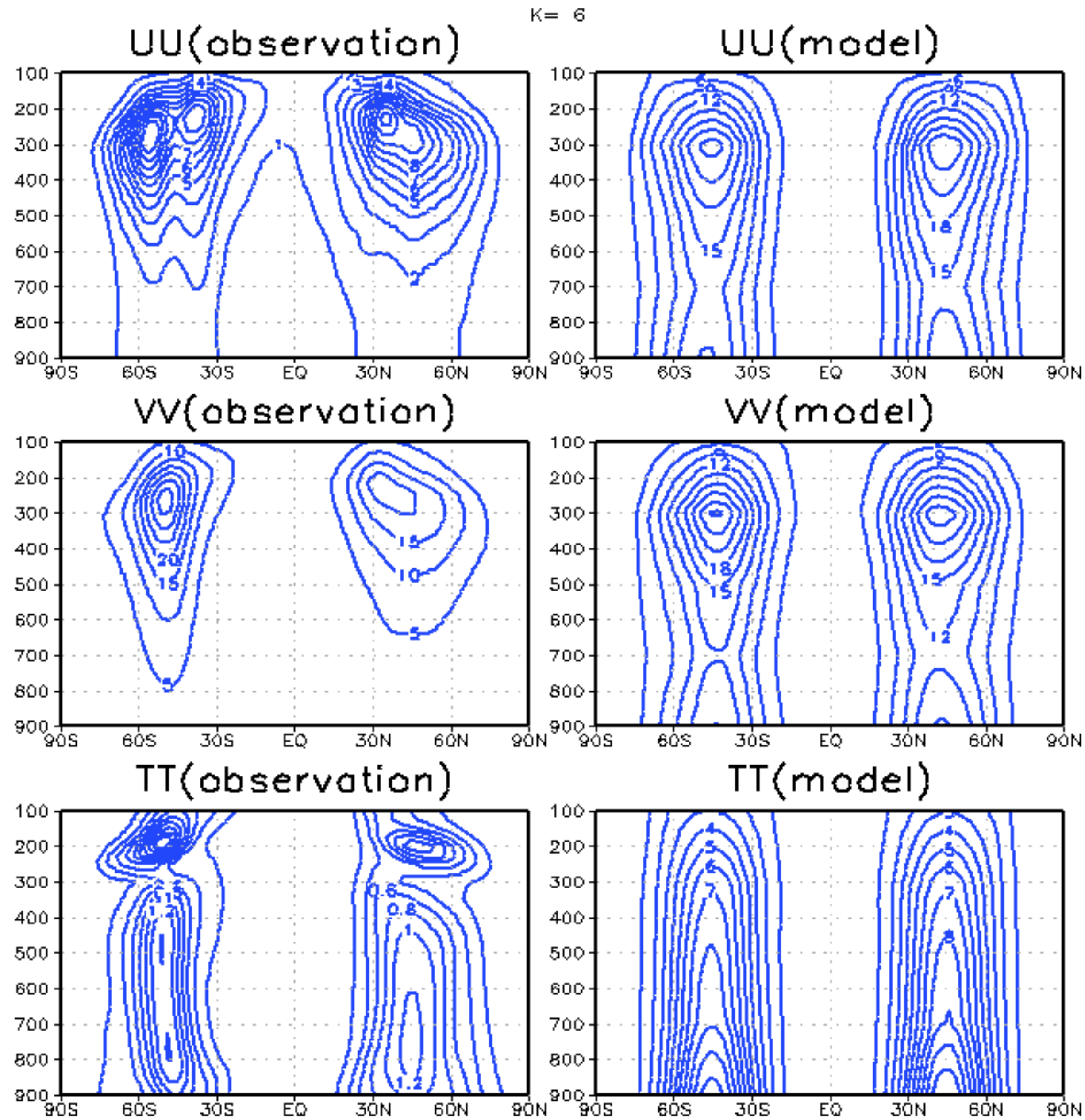

Figure 5.4b: Same as fig. 5.4a, but for eddy variances

5.4.2 Linear Stochastic Atmospheric Model

Eddy heat and momentum fluxes play an important role in determining the mean and variability of the climate, and reasonable simulation of these fluxes is a crucial benchmark for the model's performance (Zhang and Held, 1999). Thus, we first show the response of the stochastic atmospheric model with no radiation and no ocean coupling, in order to establish that the model produces realistic synoptic scale eddy statistics. The response of the 5 level linear stochastic atmospheric model is compared to observations in figs. 5.4a and 5.4b. It is encouraging to note that eddy heat and momentum fluxes are simulated very well in our simple model (figure 5.4a). The eddy variances, in figure 5.4b, are simulated reasonably well except that the variances are little stronger at the surface. The eddy variance of temperature could not capture the observed maxima in the upper levels. This failure could be due to the incorrect representation of stratospheric static stability in our model. However, it is notable that our simple model does fairly well without any complicated tuning. The only tunable parameters involved in our model are the location and breadth of the forcing (which is Gaussian) and the 'artificial damping' of 1 day^{-1} used to stabilize the model. The model used to produce figures 5.4a and 5.4b does not have ocean mixed layer, boundary layer dynamics and any radiation scheme. Moreover, moisture, cloud parameterization, moist convection, realistic radiation and zonal variation in the background state are not part of our modeling scheme. The success of our simple model with very few parameters infuses a confidence that the addition of boundary layer scheme, surface fluxes and ocean mixed layer would improve the simulation of eddy fluxes and variances and could possibly generate low frequency variability in our model.

5.4.3 Coupling with Radiation and Ocean mixed layer

To gain insight into the role of the various physical processes, we computed the eigenvalues of various dynamical models built from different combinations of physics. The resulting eigenvalues are shown in fig. 5.5 for the following configurations: atmosphere-only model with artificial damping (blue stars)- lower boundary condition is no-flux boundary condition at the surface; the radiation-only model (green stars)- lower boundary condition is energy balance at the bottom surface; the ocean-only model (magenta dots)- instantaneous energy balance at the top surface of the ocean mixed layer; the atmosphere coupled to the radiation (red squares)- lower boundary condition is energy balance at the bottom surface; and the atmosphere coupled to the radiation and ocean models and with parameterizations for surface friction and sensible heat flux (black circles). The eigenvalues of the dynamical core are negative due to the constant artificial damping. The figure shows that radiation (green stars) acts just as a pure damping and does not generate oscillatory modes (as indicated by the fact that the associated eigenvalues have zero imaginary parts). In general, coupling radiation to the atmospheric model effectively damps the atmosphere-only modes.

It is apparent that the ocean has much longer (i.e., lower frequency) time scales than the atmosphere-radiation model. However, the ocean mixed layer also introduces very large damping on purely damped modes (see black circles). It is interesting to note that the mixed layer is also introducing a new mode of oscillation that is probably decoupled from the atmosphere and has long damping timescale (black circles in figure 5.5(b)). This new mode might be related to the generation of low frequency variability in the model (I will discuss it in more detail in the next section).

5.4.4 Power Spectrum of the Coupled Stochastic Model

Figure 5.6 shows the leading EOF of the surface pressure as a response of the stochastic model of atmosphere coupled with shallow ocean mixed layer (depth $10^{-11}m$). It shows large variance in the northern hemisphere midlatitudes. The power spectrum of the leading EOF of surface pressure shown in figure 5.6 is exhibited in fig. 5.7 which peaks at 1.5 days. Since the total covariance matrix is the sum of the area under the curve in figure 5.7(a), the eddy fluxes and variances in figures 5.4a and 5.4b seem to be dominated by high frequency variability. It is interesting to observe that the power spectrum of the finite mixed layer case (mixed layer depth = $100m$) produces additional peak at much longer times scale (33 months) in addition to the power at weather timescale. Thus, it is clear that our stochastic

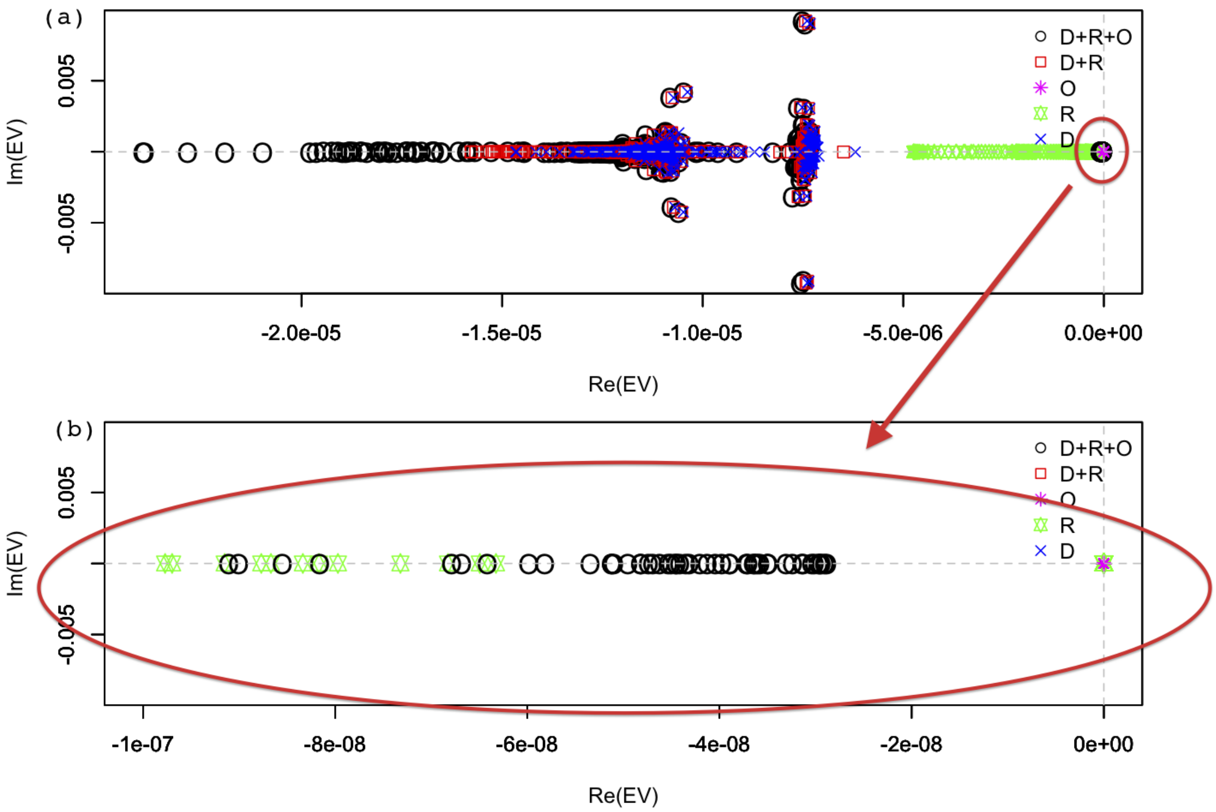

Figure 5.5: Eigenvalues of the dynamical operator associated with different configurations of the stochastic model. The blue, green, and magenta dots represent eigenvalues associated with pure dynamical model, radiation model and ocean mixed layer, respectively. The eigenvalues in red and black color are associated with dynamical model coupled with radiation module and dynamical model coupled with radiation and ocean mixed layer, respectively.

coupled atmosphere-ocean mixed layer model produces low frequency variability. Now, it is desirable to understand the mechanism of this low frequency variability. Mathematical analysis suggests that the power at this lower frequency is supposed to occur when the frequency is equal to the imaginary part of the eigenvalue of the dynamical operator while the real part of the eigenvalue is very small. A preliminary examination of the results in figure 5.5(b) suggests that more than one coupled mode (black circles), whose real part of the eigenvalues are close to zero, might be responsible for the generation of power at low frequency. To verify this, we identified and removed these modes from the calculation of

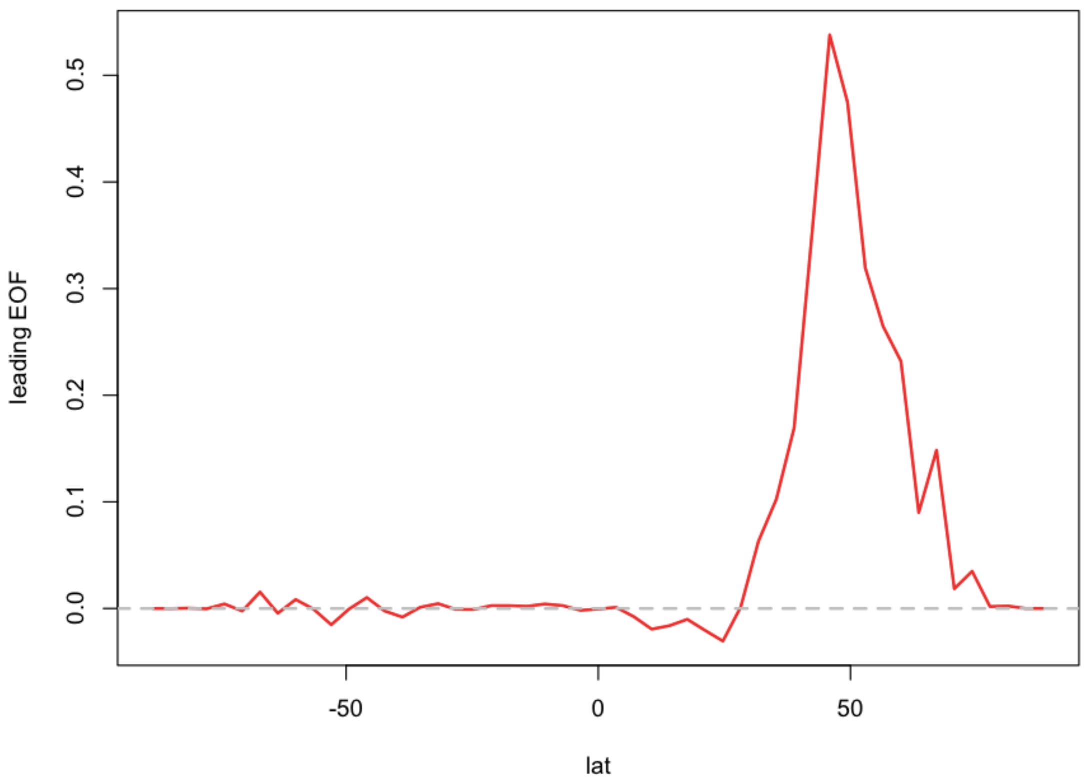

Figure 5.6: The leading EOF of surface pressure from the stochastic model of the atmosphere coupled to a shallow ocean mixed layer of $10^{-11}m$ depth.

the power spectrum, which resulted in suppressed power at low frequencies. An interesting feature in figure 5.7 is that the variance is reduced at all timescales shorter than 30 months in finite mixed layer case as compared to that in shallow mixed layer case. This is an intriguing feature that needs further examination. Our future research involves understanding these new results.

We investigated various methods for physically interpreting the above results, including Green's function methods and time-scale separation techniques. However, we did not obtain meaningful results, so we omit them here.

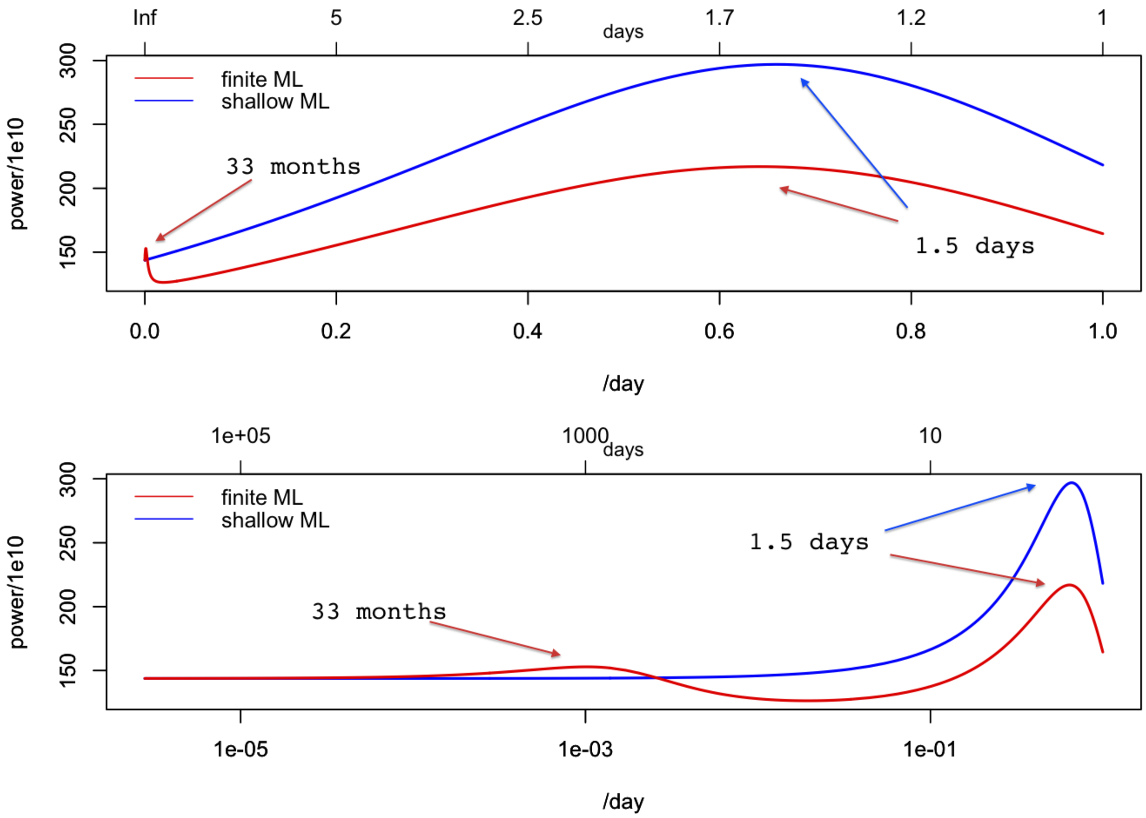

Figure 5.7: Power spectrum of the leading eigenmode of surface pressure in the finite mixed layer case (red; h = $100m$) and shallow mixed layer case (blue; h = $10^{-11}m$). The specific eigenmode is derived from the shallow mixed layer case.

5.5 Summary

Our studies on CMIP3 models suggested that decadal predictability can be derived without a role of interactive ocean dynamics. However, these models are nonlinear and hence chaotic, therefore understanding mechanisms in such models is challenging. Therefore, in order to better isolate the mechanisms of decadal predictability that do not involve interactive ocean dynamics, we built a linear stochastic model of atmosphere coupled to a slab ocean mixed layer.

The atmospheric component of the model involves full primitive equations and the lower boundary of the atmosphere is represented by a slab ocean mixed layer thermodynamically coupled to the atmosphere by grey radiation scheme and a combination of sensible and latent heat fluxes. Although this model is very simple and it does not include moisture, topography and realistic radiation etc., it includes all the necessary physics that may give rise to decadal variability. Thus this model is intermediate between Hasselmann type simple models and complex GCMs. It is important to recognize how this model differs fundamentally from Hasselmann type models: the stochastic forcing in this model does not represent atmospheric forcing of the ocean mixed layer, rather it represents the non-linear eddy-eddy interaction in the atmosphere. The response of the atmosphere to the stochastically forced eddy-eddy interaction results in the spatially coherent atmospheric variability that interacts with the slab ocean mixed layer. We stochastically forced temperature at all levels except the top, with variance that maximizes at 45° and decays away as a Gaussian with a standard deviation of 12.5 degrees. In order to have stable solutions, we have introduced a constant artificial damping of 1 /day everywhere in the model.

An eigenstability analysis of the grey radiation shows that the grey radiation acts as pure damping just like Newtonian relaxation and it does not produce any oscillatory mode. The atmospheric-only version of the the stochastic model reasonably simulates observed eddy variances and fluxes. There are some limitations such as the eddy variance of temperature could not capture the observed maxima in the upper levels. However, considering the fact that our model is extremely simple it is remarkable that it does fairly well without any complicated tuning. It is difficult to establish whether the modes produced in our model correspond to the large-scale spatial structures of internal atmospheric noise, such as those found by Colfescu and Schneider (2016), because realistic noise patterns have preferred relations with the underlying topography and stationary waves whereas our patterns have no such preference due to zonal symmetry of the basic state.

Adding ocean mixed layer to the atmosphere introduces much longer timescale than the atmosphere-radiation model. The ocean mixed layer not only adds a large damping but it also introduces new modes of oscillations. In the infinitesimally small mixed layer case (depth $10^{-11}m$), the power spectrum of the leading EOF of surface pressure variance produces a peak at weather timescale ($\sim$ 1.5 days). It is interesting to observe that the power spectrum of the finite mixed layer case (mixed layer depth = $100m$) produces additional peak at much longer times scale ($\sim$ 33 months) in addition to the power at weather timescale.

The results based upon this simple linear model suggest that atmospheric processes thermodynamically coupled to a slab ocean mixed layer can produce multiyear predictability. Interactive ocean dynamics does not seem to be necessary for generating multiyear predictability.

Chapter 6: Summary

Accurate predictions of climate variations on decadal time scales would be useful from societal, economic and scientific perspectives. Unfortunately, the physical mechanisms giving rise to decadal predictability are unsettled. For instance, it is commonly assumed that predictions on ten-year time scales require climate models with interactive ocean dynamics. This view has been challenged recently by the demonstration that certain forms of decadal variability can arise in climate models even in the absence of interactive ocean dynamics. More precisely, certain forms of decadal variability can arise in an atmospheric model coupled to a 50m-deep slab ocean mixed layer with no interactive currents. We call such climate models "slab" models, whereas fully coupled atmosphere-ocean models will be called "coupled" models.

The purpose of this thesis project was to improve our understanding of decadal predictability. To clarify the mechanisms of decadal predictability, we diagnosed the most predictable patterns of monthly 2m air temperature in coupled and slab models. This diagnosis was based on Average Predictability Time (APT) analysis, which objectively identifies the linear combination of variables that maximizes the integral time scale of predictability. The particular models used in our analysis come from the phase 3 of the Coupled Model Intercomparison Project (CMIP3), which was chosen because it contains slab model runs (the most recent data set, CMIP5, does not have slab runs). However, CMIP3 does not have decadal predictions. Accordingly, decadal predictability was estimated using a multivariate linear regression model trained on long control simulations, which have no year-to-year changes in external forcing (e.g., solar insolation, volcanic aerosols).

Our major result is that the most predictable patterns of internal variability in coupled and slab models are remarkably similar. In addition, the predictability time scales, in perfect model sense, are comparable for coupled and slab models for most of the components diagnosed. For instance, for the first predictable component, predictability limit in the slab models is around three years whereas it is around two years in the coupled models. For the second component, the predictability limit is around three years and is less than two years in the slab models. For the third predictable component, the predictability limit is around one and half years for both the slab and coupled models. We also demonstrate that these components are relevant to observations by showing that the regression models derived from climate simulations can give skillful predictions of these components. The skill of these predictions are comparable for coupled and slab models, although there are a few exceptions in which regressions based on coupled simulations give higher skill, suggesting an important role for ocean circulations. However, the difference in skill is relatively small (a few months). The similarity of predictability and forecast skills derived from the slab and coupled models strongly suggests that interactive ocean dynamics are not essential for multiyear predictability. Instead the essential physics appears to involve atmospheric processes coupled to slab ocean mixed layer.

The above results based on a multimodel analysis were investigated in more detail on a model-by-model basis. A major limitation in the model-by-model analysis was that the sample sizes of slab models are much smaller than their coupled counterparts. This short sample size raises the significance level of predictability in slab models. Based upon the strict application of significance level, it appears that predictability in most of the coupled models (5 years or longer) is much higher than their slab counterparts (around 2 years). However, this result must be taken with caution as the predictability of slab and coupled models were found to be similar in the multimodel analysis. Remember that in the multimodel approach the effective sample size of slab models was very large due to pooling of the slab model data together. Moreover, excluding the component 2, for other components diagnosed, the higher predictability of coupled models than their slab versions does not translate into their higher predictive skill. It was found that the prediction skill of the coupled models were similar to their slab counterparts (between 1 and 2 years) for all the components diagnosed except for component 2 where coupled models ($\sim$ 2 years) have higher skill than their slab counterparts ($\sim$ 1 year). The most striking result of the model-by-model analysis was that the most predictable patterns in slab and coupled models had similar predictabilities. Although the magnitude of predictability is sensitive to model, the spatial structures of the most predictable components are not.

Our analysis also highlights that the conventional indices like the AMO and PDO are not the most predictable patterns in the models on the decadal timescale. It should be recognized that these indices were not designed to be most predicable on decadal/multidecadal timescale. In contrast, ENSO seems to be better identified with the most predictable components, and hence is an appropriate target for predictability.

We admit that there are important caveats with identifying predictable components from models. Specifically, the models may have unrealistic predictability or be compromised by significant biases. In addition, comparison between model and observations is complicated by the fact that observations contain both internal and forced variability.

In order to identify and understand important mechanisms of decadal predictability, we also constructed a linear stochastic model of primitive equation atmosphere coupled to the slab ocean mixed layer through grey radiation scheme and surface latent and sensible heat fluxes. The model is extremely simple as it does not include topography, moisture, clouds, realistic radiation etc.. Despite being simple, it produces realistic eddy variances and fluxes on weather timescale. Coupling of the ocean mixed layer produces two peaks: one at weather timescale ($\sim$ 1.5 days) and the other at multiyear timescale ($\sim$ 33 months). The peak at multiyear timescale is absent in the atmosphere only model. The coupled atmosphere-mixed layer ocean produces new modes of variability, characterized by complex, low-frequency eigenvalues, which in turn generate spectral peaks at low frequencies that do not occur in the atmosphere alone or in the slab-ocean model alone.This shows that atmospheric dynamics coupled to slab ocean mixed layer can produce multiyear predictability and the interactive ocean dynamics does not seem to be necessary for the generation of multiyear predictability.

Bibliography

Ba, J., and Coauthors, 2014: A multi-model comparison of atlantic multidecadal variability. *Climate dynamics*, **43 (9-10)**, 2333–2348.

Bellomo, K., A. Clement, T. Mauritsen, G. Rädel, and B. Stevens, 2014: Simulating the role of subtropical stratocumulus clouds in driving pacific climate variability. *Journal of Climate*, **27 (13)**, 5119–5131.

Bellucci, A., and Coauthors, 2012: Decadal climate predictions with a coupled OAGCM initialized with oceanic reanalysis. *Clim. Dyn.*, DOI10.1007/s00 382–012–1468–z.

Boer, G. J., 2004: Long time-scale potential predictability in an ensemble of coupled climate models. *Climate dynamics*, **23 (1)**, 29–44.

Boer, G. J., 2011: Decadal potential predictability of twenty-first century climate. *Climate dynamics*, **36 (5-6)**, 1119–1133.

Boer, G. J., and S. J. Lambert, 2008: Multi-model decadal potential predictability of precipitation and temperature. *Geophys. Res. Lett.*, **35**, DOI:10.1029/2008GL033 234.

Booth, B. B. B., N. J. Dunstone, P. R. Halloran, R. Andrews, and N. Bellouin, 2012: Aerosols implicated as a prime driver of twentieth-century North Atlantic climate variability. *Nature*, **484**, 228–232.

Bouma, M., and H. Van der Kaay, 1994: Epidemic malaria in india and the el nino southern oscillation. *The Lancet*, **344 (8937)**, 1638–1639.

Buckley, M. W., and J. Marshall, 2016: Observations, inferences, and mechanisms of the atlantic meridional overturning circulation: A review. *Reviews of Geophysics*.

Chang, P., R. Saravanan, T. DelSole, and F. Wang, 2004: Predictability of linear coupled systems. Part I: Theoretical analyses. *J. Climate*, **17**, 1474–1486.

Chen, H., E. K. Schneider, and Z. Wu, 2016: Mechanisms of internally generated decadal-to-multidecadal variability of sst in the atlantic ocean in a coupled gcm. *Climate Dynamics*, **46 (5-6)**, 1517–1546.

Clement, A., K. Bellomo, L. N. Murphy, M. A. Cane, T. Mauritsen, G. Rädel, and B. Stevens, 2015: The atlantic multidecadal oscillation without a role for ocean circulation. *Science*, **350 (6258)**, 320–324.

Clement, A., M. A. Cane, L. N. Murphy, K. Bellomo, T. Mauritsen, and B. Stevens, 2016: Response to comment on "the atlantic multidecadal oscillation without a role for ocean circulation". *Science*, **352 (6293)**, 1527–1527, doi:10.1126/science.aaf2575, URL http://science.sciencemag.org/content/352/6293/1527.2, http://science.sciencemag.org/content/352/6293/1527.2.full.pdf.

Clement, A., P. DiNezio, and C. Deser, 2011: Rethinking the ocean's role in the southern oscillation. *Journal of climate*, **24 (15)**, 4056–4072.

Colfescu, I., and E. K. Schneider, 2016: Internal atmospheric noise characteristics in twentieth century coupled atmosphere–ocean model simulations. *Climate Dynamics*, 1–13.

Collins, M., 2002: Climate predictability on interannual to decadal time scales: the initial value problem. *Climate Dynamics*, **19 (8)**, 671–692.

Collins, M., D. Frame, B. Sinha, and C. Wilson, 2002: How far ahead could we predict el nino? *Geophysical Research Letters*, **29 (10)**.

Collins, M., and Coauthors, 2006: Interannual to decadal climate predictability in the north atlantic: a multimodel-ensemble study. *Journal of climate*, **19 (7)**, 1195–1203.

DelSole, T., 2004: Stochastic models of quasigeostrophic turbulence. *Surveys in Geophysics*, **25 (2)**, 107–149.

DelSole, T., 2016: Decadal prediction: Achievements and future prospects. *Current Climate Change Reports.*, **In press**.

DelSole, T., and P. Chang, 2003: Predictable component analysis, canonical correlation analysis, and autoregressive models. *J. Atmos. Sci.*, **60**, 409–416.

DelSole, T., and M. K. Tippett, 2007: Predictability: Recent insights from information theory. *Rev. Geophys.*, **45**, RG4002, doi:10.1029/2006RG000202.

DelSole, T., and M. K. Tippett, 2009a: Average predictability time: Part I. Theory. *J. Atmos. Sci*, **66**, 1172–1187.

DelSole, T., and M. K. Tippett, 2009b: Average predictability time. part ii: Seamless diagnoses of predictability on multiple time scales. *Journal of the Atmospheric Sciences*, **66 (5)**, 1188–1204.

DelSole, T., and M. K. Tippett, 2015: Laplacian eigenfunctions for climate analysis. *J. Climate*, **28**, 7420–7436.

Delworth, T. L., and M. E. Mann, 2000: Observed and simulated multidecadal variability in the northern hemisphere. *Climate Dynamics*, **16 (9)**, 661–676.

Delworth, T. L., R. Zhang, and M. E. Mann, 2007: Decadal to centennial variability of the atlantic from observations and models. *Ocean Circulation: Mechanisms and Impacts-Past and Future Changes of Meridional Overturning*, 131–148.

Déqué, M., 1988: 10-day predictability of the northern hemisphere winter 500-mb height by the ECMWF operational model. *Tellus*, **40A**, 26–36.

Deser, C., M. A. Alexander, and M. S. Timlin, 1999: Evidence for a wind-driven intensification of the kuroshio current extension from the 1970s to the 1980s. *Journal of Climate*, **12 (6)**, 1697–1706.

Deser, C., M. A. Alexander, and M. S. Timlin, 2003: Understanding the persistence of sea surface temperature anomalies in midlatitudes. *Journal of Climate*, **16 (1)**, 57–72.

Deser, C., A. S. Phillips, and J. W. Hurrell, 2004: Pacific interdecadal climate variability: Linkages between the tropics and the north pacific during boreal winter since 1900. *Journal of Climate*, **17 (16)**, 3109–3124.

Ding, R., J. Li, F. Zheng, J. Feng, and D. Liu, 2016: Estimating the limit of decadal-scale climate predictability using observational data. *Climate Dynamics*, **46 (5-6)**, 1563–1580.

Dommenget, D., 2010: The slab ocean el niño. *Geophysical Research Letters*, **37 (20)**.

Dommenget, D., S. Haase, T. Bayr, and C. Frauen, 2014: Analysis of the slab ocean el nino atmospheric feedbacks in observed and simulated enso dynamics. *Climate dynamics*, **42 (11-12)**, 3187–3205.

Dommenget, D., and M. Latif, 2008: Generation of hyper climate modes. *Geophysical Research Letters*, **35 (2)**.

Easterling, W. E., and Coauthors, 2007: Food, fibre and forest products. *Climate change*, 273–313.

Fan, M., and E. K. Schneider, 2012: Observed decadal north atlantic tripole sst variability. part i: weather noise forcing and coupled response. *Journal of the Atmospheric Sciences*, **69 (1)**, 35–50.

Farneti, R., and G. K. Vallis, 2011: Mechanisms of interdecadal climate variability and the role of ocean–atmosphere coupling. *Climate dynamics*, **36 (1-2)**, 289–308.

Frankignoul, C., A. Czaja, and B. L'Heveder, 1998: Air–sea feedback in the north atlantic and surface boundary conditions for ocean models. *Journal of climate*, **11 (9)**, 2310–2324.

Frankignoul, C., and K. Hasselmann, 1977: Stochastic climate models, part ii application to sea-surface temperature anomalies and thermocline variability. *Tellus*, **29 (4)**, 289–305.

Frankignoul, C., P. Müller, and E. Zorita, 1997: A simple model of the decadal response of the ocean to stochastic wind forcing. *Journal of Physical Oceanography*, **27 (8)**, 1533–1546.

Frankignoul, C., and R. W. Reynolds, 1983: Testing a dynamical model for mid-latitude sea surface temperature anomalies. *Journal of physical oceanography*, **13 (7)**, 1131–1145.

Frierson, D. M., I. M. Held, and P. Zurita-Gotor, 2006: A gray-radiation aquaplanet moist gcm. part i: Static stability and eddy scale. *Journal of the atmospheric sciences*, **63 (10)**, 2548–2566.

Frumkin, H., J. Hess, G. Luber, J. Malilay, and M. McGeehin, 2008: Climate change: the public health response. *American Journal of Public Health*, **98 (3)**, 435–445.

Gastineau, G., and C. Frankignoul, 2012: Cold-season atmospheric response to the natural variability of the atlantic meridional overturning circulation. *Climate dynamics*, **39 (1-2)**, 37–57.

Giannakis, D., and A. J. Majda, 2012: Nonlinear Laplacian spectral analysis for time series with intermittency and low-frequency variability. *Proceedings of the National Academy of Sciences*, **109 (7)**, 2222–2227, URL http://www.pnas.org/content/109/7/2222.abstractN2.

Goldenberg, S. B., C. W. Landsea, A. M. Mestas-Nuñez, and W. M. Gray, 2001: The recent increase in Atlantic hurricane activity: Causes and implications. *Science*, **293 (5529)**, 474–479.

Griffies, S. M., and K. Bryan, 1997: Predictability of north atlantic multidecadal climate variability. *Science*, **275 (5297)**, 181–184.

Gu, D., and S. G. Philander, 1997: Interdecadal climate fluctuations that depend on exchanges between the tropics and extratropics. *Science*, **275 (5301)**, 805–807.

Gulev, S. K., M. Latif, N. Keenlyside, W. Park, and K. P. Koltermann, 2013: North atlantic ocean control on surface heat flux on multidecadal timescales. *Nature*, **499 (7459)**, 464–467.

Hall, A., and S. Manabe, 1997: Can local linear stochastic theory explain sea surface temperature and salinity variability? *Climate Dynamics*, **13 (3)**, 167–180.

Hasselmann, K., 1976: Stochastic climate models I. Theory. *Tellus*, **28**, 473–485.

Hawkins, E., and R. Sutton, 2009: Decadal predictability of the atlantic ocean in a coupled gcm: Forecast skill and optimal perturbations using linear inverse modeling. *Journal of Climate*, **22 (14)**, 3960–3978.

Hegerl, G. C., and Coauthors, 2007: Understanding and attributing climate change. *Climate Change 2007: The Physical Science Basis. Contribution of Working Group I to the Fourth Assessment Report of the Intergovernmental Panel on Climate Change*, S. Solomon, D. Qin, M. Manning, Z. Chen, M. Marquis, K. Averyt, M. Tignor, and H. Miller, Eds., Cambridge University Press, 663–745.

Hurrell, J., and Coauthors, 2010: Decadal climate prediction: Opportunities and challenges. *OceanObsÕ 09: Sustained Ocean Observations and Information for Society*, 521–533.

Jia, L., 2011: Robust multi-year predictability on continental scales. URL https://search-proquest-com.mutex.gmu.edu/docview/868708088?accountid=14541, copyright - Database copyright ProQuest LLC; ProQuest does not claim copyright in the individual underlying works; Last updated - 2016-03-10, 114 pp.

Jia, L., and T. DelSole, 2012: Multi-year predictability of temperature and precipitation identified in climate models. *Geophys. Res. Lett.*, **39**, doi:10.1029/2012GL052 778.

Kirtman, B., D. Anderson, G. Brunet, I.-S. Kang, A. A. Scaife, and D. Smith, 2013a: Prediction from weeks to decades. *Climate science for serving society*, Springer, 205–235.

Kirtman, B., and Coauthors, 2013b: Near-term climate change: Projections and predictability. *Climate Change 2013: The Physical Science Basis. Contribution of Working Group I to the Fifth Assessment Report of the Intergovernmental Panel on Climate Change*,

T. Stocker, D. Qin, G.-K. Plattner, M. Tignor, S. Allen, J. Boschung, A. Nauels, Y. Xia, V. Bex, and P. Midgley, Eds., Cambridge University Press, chap. 11, 953–1028.

Kirtman, B. P., and J. Shukla, 2002: Interactive coupled ensemble: A new coupling strategy for cgcms. *Geophysical research letters*, **29 (10)**.

Knight, J. R., R. J. Allan, C. K. Folland, and M. Vellinga, 2005: A signature of persistent natural thermohaline circulation cycles in observed climate. *Geophys. Res. Lett.*, **32 (L20708)**, doi:10.1029/2005GL024 233.

Knight, J. R., C. K. Folland, and A. A. Scaife, 2006: Climate impacts of the atlantic multidecadal oscillation. *Geophysical Research Letters*, **33 (17)**, n/a–n/a, doi:10.1029/2006GL026242.

Krishnamurthy, L., and V. Krishnamurthy, 2014: Influence of pdo on south asian summer monsoon and monsoon–enso relation. *Climate Dynamics*, **42 (9)**, 2397–2410, doi:10.1007/s00382-013-1856-z, URL http://dx.doi.org/10.1007/s00382-013-1856-z.

Krishnan, R., and M. Sugi, 2003: Pacific decadal oscillation and variability of the indian summer monsoon rainfall. *Climate Dynamics*, **21 (3-4)**, 233–242.

Kucharski, F., and Coauthors, 2016: Atlantic forcing of pacific decadal variability. *Climate Dynamics*, **46 (7-8)**, 2337–2351.

Latif, M., and T. P. Barnett, 1994: Causes of decadal climate variability over the north pacific and north america. *Science*, **266 (5185)**, 634–637.

Latif, M., and N. S. Keenlyside, 2011: A perspective on decadal climate variability and predictability. *Deep Sea Research Part II: Topical Studies in Oceanography*, **58 (17)**, 1880–1894.

Latif, M., and Coauthors, 2004: Reconstructing, monitoring, and predicting multidecadal-scale changes in the north atlantic thermohaline circulation with sea surface temperature. *Journal of Climate*, **17 (7)**, 1605–1614.

Lawley, D. N., 1956: Tests of significance for the latent roots of covariance and correlation matrices. *Biometrika*, **43**, 128–136.

Li, J., and R. Ding, 2013: Temporal–spatial distribution of the predictability limit of monthly sea surface temperature in the global oceans. *International Journal of Climatology*, **33 (8)**, 1936–1947.

Mantua, N. J., and S. R. Hare, 2002: The pacific decadal oscillation. *Journal of Oceanography*, **58 (1)**, 35–44.

Mantua, N. J., S. R. Hare, Y. Zhang, J. M. Wallace, and R. C. Francis, 1997: A Pacific interdecal climate oscillation with impacts on salmon production. *Bull. Amer. Mereor. Soc.*, **78**, 1069–1079.

Marshall, J., and Coauthors, 2001: North Atlantic climate variability: Phenomena, impacts, and mechanisms. *Int. J. Climatology*, **21**, 1863–1898.

McCabe, G. J., M. A. Palecki, and J. L. Betancourt, 2004: Pacific and atlantic ocean influences on multidecadal drought frequency in the united states. *Proceedings of the National Academy of Sciences*, **101 (12)**, 4136–4141, URL http://www.pnas.org/content/101/12/4136.

Meehl, G. A., and Coauthors, 2007: Global climate projections. *Climate Change 2007: The Physical Science Basis. Contribution of Working Group I to the Fourth Assessment Report of the Intergovernmental Panel on Climate Change*, S. Solomon, D. Qin, M. Manning, Z. Chen, M. Marquis, K. B. Averyt, M. Tignor, and H. L. Miller, Eds., Cambridge University Press, chap. 10, 747–845.

Meehl, G. A., and Coauthors, 2014: Decadal climate prediction: an update from the trenches. *Bulletin of the American Meteorological Society*, **95 (2)**, 243–267.

Menary, M. B., D. L. Hodson, J. I. Robson, R. T. Sutton, R. A. Wood, and J. A. Hunt, 2015: Exploring the impact of cmip5 model biases on the simulation of north atlantic decadal variability. *Geophysical Research Letters*, **42 (14)**, 5926–5934.

Newman, M., 2007: Interannual to decadal predictability of tropical and north Pacific sea surface temperatures. *J. Climate*, **20**, 2333–2356.

Newman, M., 2013: An empirical benchmark for decadal forecasts of global surface temperature anomalies. *J. Climate*, **26**, 5260–5269.

Newman, M., G. P. Compo, and M. A. Alexander, 2003: Enso-forced variability of the pacific decadal oscillation. *Journal of Climate*, **16 (23)**, 3853–3857, doi: 10.1175/1520-0442(2003)016⟨3853:EVOTPD⟩2.0.CO;2, URL http://dx.doi.org/10.1175/1520-0442(2003)016⟨3853:EVOTPD⟩2.0.CO;2.

Newman, M., and Coauthors, 2016: The pacific decadal oscillation, revisited. *Journal of Climate*, **29 (12)**, 4399–4427.

Noble, B., and J. W. Daniel, 1988: *Applied Linear Algebra*. 3rd ed., Prentice-Hall, 521 pp.

O'Reilly, C. H., M. Huber, T. Woollings, and L. Zanna, 2016: The signature of low frequency oceanic forcing in the atlantic multidecadal oscillation. *Geophysical Research Letters*.

Park, S., C. Deser, and M. A. Alexander, 2005: Estimation of the surface heat flux response to sea surface temperature anomalies over the global oceans. *Journal of climate*, **18 (21)**, 4582–4599.

Park, T., W. Park, and M. Latif, 2016: Correcting north atlantic sea surface salinity biases in the kiel climate model: influences on ocean circulation and atlantic multidecadal variability. *Climate Dynamics*, 1–18.

Park, W., and M. Latif, 2005: Ocean dynamics and the nature of air–sea interactions over the north atlantic at decadal time scales. *Journal of climate*, **18 (7)**, 982–995.

Pohlmann, H., M. Botzet, M. Latif, A. Roesch, M. Wild, and P. Tschuck, 2004: Estimating the long-term predictability potential of a coupled AOGCM. *J. Climate*, **17**, 4463–4472.

Rayner, N., D. E. Parker, E. Horton, C. Folland, L. Alexander, D. Rowell, E. Kent, and A. Kaplan, 2003: Global analyses of sea surface temperature, sea ice, and night marine air temperature since the late nineteenth century. *Journal of Geophysical Research: Atmospheres*, **108 (D14)**.

Renwick, J. A., and J. M. Wallace, 1995: Predictable anomaly patterns and the forecast skill of northern hemisphere wintertime 500-mb height fields. *Mon. Wea. Rev.*, **123**, 2114–2131.

Robock, A., 2000: Volcanic eruptions and climate. *Reviews of Geophysics*, **38 (2)**, 191–219.

Saravanan, R., and J. C. McWilliams, 1997: Stochasticity and spatial resonance in interdecadal climate fluctuations. *Journal of Climate*, **10 (9)**, 2299–2320.

Saravanan, R., and J. C. McWilliams, 1998: Advective ocean-atmosphere interaction: An analytical stochastic model with implications for decadal variability. *Journal of Climate*, **11 (2)**, 165–188.

Schlesinger, M. E., and N. Ramankutty, 1994: An oscillation in the global climate system of period 65-70 years. *Nature*, **367**, 723–726.

Schneider, E. K., and M. Fan, 2012: Observed decadal north atlantic tripole sst variability. part ii: diagnosis of mechanisms. *Journal of the Atmospheric Sciences*, **69 (1)**, 51–64.

Schneider, N., and B. D. Cornuelle, 2005: The forcing of the pacific decadal oscillation*. *Journal of Climate*, **18 (21)**, 4355–4373.

Schneider, N., A. J. Miller, and D. W. Pierce, 2002: Anatomy of north pacific decadal variability. *Journal of climate*, **15 (6)**, 586–605.

Schneider, T., and S. Griffies, 1999: A conceptual framework for predictability studies. *J. Climate*, **12**, 3133–3155.

Seager, R., Y. Kushnir, N. H. Naik, M. A. Cane, and J. Miller, 2001: Wind-driven shifts in the latitude of the kuroshio–oyashio extension and generation of sst anomalies on decadal timescales. *Journal of Climate*, **14 (22)**, 4249–4265.

Seager, R., Y. Kushnir, M. Visbeck, N. Naik, J. Miller, G. Krahmann, and H. Cullen, 2000: Causes of atlantic ocean climate variability between 1958 and 1998. *Journal of Climate*, **13 (16)**, 2845–2862.

Simmons, A. J., and A. Hollingsworth, 2002: Some aspects of the improvement in skill of numerical weather prediction. *Q. J. R. Meteorol. Soc.*, **128**, 647–677.

Siqueira, L., and B. P. Kirtman, 2016: Atlantic near-term climate variability and the role of a resolved gulf stream. *Geophysical Research Letters*, **43 (8)**, 3964–3972.

Smith, D. M., A. A. Scaife, and B. P. Kirtman, 2012: What is the current state of scientific knowledge with regard to seasonal and decadal forecasting? *Environmental Research Letters*, **7 (1)**, 015 602.

Smith, T. M., R. W. Reynolds, T. C. Peterson, and J. Lawrimore, 2008: Improvements to NOAA's historical merged land–ocean surface temperature analysis (1880–2006). *J. Climate*, **21**, 2283–2296.

Srivastava, A., and T. DelSole, 2017: Decadal predictability without ocean dynamics. *Proceedings of the National Academy of Sciences*, **114 (9)**, 2177–2182, doi:10.1073/pnas.1614085114, URL http://www.pnas.org/content/114/9/2177.abstract, http://www.pnas.org/content/114/9/2177.full.pdf.

Suckling, E. B., and L. A. Smith, 2013: An evaluation of decadal probability forecasts from state-of-the-art climate models. *Journal of Climate*, **26 (23)**, 9334–9347, doi:10.1175/JCLI-D-12-00485.1, URL http://dx.doi.org/10.1175/JCLI-D-12-00485.1.

Timmermann, A., M. Latif, R. Voss, and A. Grötzner, 1998: Northern hemispheric interdecadal variability: A coupled air–sea mode. *Journal of Climate*, **11 (8)**, 1906–1931.

Trenary, L., and T. DelSole, 2016: Does the atlantic multidecadal oscillation get its predictability from the atlantic meridional overturning circulation? *Journal of Climate*, **29 (14)**, 5267–5280, doi:10.1175/JCLI-D-16-0030.1, URL http://dx.doi.org/10.1175/JCLI-D-16-0030.1.

Vera, C., and Coauthors, 2010: Needs assessment for climate information on decadal timescales and longer. *Procedia Environmental Sciences*, **1**, 275–286.

Weng, W., and J. D. Neelin, 1998: On the role of ocean-atmosphere interaction in midlatitude interdecadal variability. *Geophysical research letters*, **25 (2)**, 167–170.

Whitaker, J. S., and P. D. Sardeshmukh, 1998: A linear theory of extratropical synoptic eddy statistics. *J. Atmos. Sci.*, **55**, 237–258.

Zanna, L., 2012: Forecast skill and predictability of observed North Atlantic sea surface temperatures. *J. Climate*, **25**, 5047–5056.

Zhang, R., T. L. Delworth, and I. M. Held, 2007: Can the Atlantic Ocean drive the observed multidecadal variability in the Northern Hemisphere mean temperature? *Geophys. Res. Lett.*, **34**, DOI:10.1029/2006GL028 683.

Zhang, R., R. Sutton, G. Danabasoglu, T. L. Delworth, W. M. Kim, J. Robson, and S. G. Yeager, 2016: Comment on òthe atlantic multidecadal oscillation without a role for ocean circulationó. *Science*, **352 (6293)**, 1527–1527.

Zhang, R., and Coauthors, 2013: Have aerosols caused the observed Atlantic multidecadal variability? *J. Atmos. Sci.*, **70 (4)**, 1135–1144.

Zhang, Y., and I. M. Held, 1999: A linear stochastic model of a gcm's midlatitude storm tracks. *Journal of the atmospheric sciences*, **56 (19)**, 3416–3435.

Zheng, F., J. Zhu, R.-H. Zhang, and G.-Q. Zhou, 2006: Ensemble hindcasts of sst anomalies in the tropical pacific using an intermediate coupled model. *Geophysical research letters*, **33 (19)**.

Curriculum Vitae

Abhishekh Srivastava was born in Varanasi city of state Uttar Pradesh in India. He graduated from University of Allahabad in 1997 with a Bachelor of Science (B.Sc.). He received his Master of Science (M.Sc.) from University of Allahabad in 2000. He joined Ph.D. in Climate Dynamics program of George Mason University in 2010.